



저작자표시-비영리-변경금지 2.0 대한민국

이용자는 아래의 조건을 따르는 경우에 한하여 자유롭게

- 이 저작물을 복제, 배포, 전송, 전시, 공연 및 방송할 수 있습니다.

다음과 같은 조건을 따라야 합니다:



저작자표시. 귀하는 원 저작자를 표시하여야 합니다.



비영리. 귀하는 이 저작물을 영리 목적으로 이용할 수 없습니다.



변경금지. 귀하는 이 저작물을 개작, 변형 또는 가공할 수 없습니다.

- 귀하는, 이 저작물의 재이용이나 배포의 경우, 이 저작물에 적용된 이용허락조건을 명확하게 나타내어야 합니다.
- 저작권자로부터 별도의 허가를 받으면 이러한 조건들은 적용되지 않습니다.

저작권법에 따른 이용자의 권리와 책임은 위의 내용에 의하여 영향을 받지 않습니다.

이것은 [이용허락규약\(Legal Code\)](#)을 이해하기 쉽게 요약한 것입니다.

[Disclaimer](#)



공학박사학위논문

탄성체의 점탄성 및 이력 마찰 특성에 대한
멀티스케일 해석

Multiscale Study on Viscoelastic and
Hysteresis Friction Behavior of Elastomer

2019년 2월

서울대학교 대학원

기계항공공학부

김 병 조

탄성체의 점탄성 및 이력 마찰 특성에 대한
멀티스케일 해석

Multiscale Study on Viscoelastic and
Hysteresis Friction Behavior of Elastomer

지도교수 조 맹효

이 논문을 공학박사 학위논문으로 제출함

2018년 11월

서울대학교 대학원

기계항공공학부

김 병 조

김병조의 공학박사 학위논문을 인준함

2018년 12월

위원장 : 김 윤 예

부위원장 : 조 맹효

위원 : 윤 경 종

위원 : 김 도 희

위원 : 이 승 화



Abstract

In this dissertation, a systematic multiscale simulation framework is proposed to capture the viscoelastic and frictional behavior of natural rubber materials. To overcome the limitation of time and length scale in a convention atomistic molecular dynamics simulation, a coarse-grained mapping scheme is employed. With an extended applicable scale in the coarse-grained domain, the relaxation characteristics of natural rubber system can be accessed and quantified. For the unvulcanized natural rubbers, the effect of molecular weight on the time-dependent relaxation behavior is examined. Moreover, micro-structural changes in the bulk natural rubber are considered; vulcanization and silica nanofillers, those are relevant design parameters when producing rubber compounds as engineering applications. The coarse-grained molecular dynamics simulation results demonstrate that the relaxation characteristics of rubber are substantially influenced by the chain length. With increasing molecular weight of system, the relaxation time is also increased, which is manifested by a slowed relaxation spectrum. This feature becomes more obvious with the formation of vulcanized networks between the rubber chains. However, the effect of silica particles is relatively marginal due to a weak interfacial interaction with rubber matrix. From the relaxation spectra, the frequency-dependent dynamic modulus is calculated using the Fourier transformation. Thus, the storage and loss modulus in frequency domain are computed and compared with experimental results.

The frictional behavior of rubber exhibits a complex nature since various factors substantially alter the frictional feature, such as contact surface condition, roughness, velocity, material property, and temperature. Herein, the hysteresis friction characteristics attributed to the internal viscoelastic energy dissipation is examined when a rubber block slides on a hard rough substrate. Based on the viscoelastic properties obtained from the coarse-grained simulations, the hysteresis friction coefficients are predicted using an analytical approach depending on velocity, material property, normal pressure, and surface roughness. Moreover, the numerical simulation with a finite element model is conducted for the O-ring seal system to investigate the frictional response.

With the present multiscale framework, the viscoelastic behavior of natural rubber system can be assessed considering various design parameters. Plus, the hysteresis frictional feature of rubber is predicted with the consideration of a range of velocity and roughness length scale. Furthermore, the frictional response of rubber in contact with moving part can be examined via the numerical simulation approach.

Keywords: Elastomer, Viscoelastic Behavior, Hysteresis Friction, Multiscale Analysis, Coarse-grained Molecular Dynamics.

Student Number: 2012-23937

Table of Contents

Table of Contents	iii
List of Figures	vi
List of Tables	xii
1. Introduction	1
1.1. Rubber friction	1
1.2. Viscoelastic nature of polymer	3
1.3. Viscoelastic property with molecular dynamics simulation	4
1.4. Outline of the thesis.....	5
2. Coarse-grained modeling methodology.....	7
2.1. Overview of coarse-grained molecular dynamics	7
2.2. Iterative Boltzmann inversion	8
2.3. Coarse-grained modeling of rubber system.....	16
2.3.1. Coarse-grained potential for bulk natural rubber	16
2.3.2. Coarse-grained modeling of rubber vulcanization	27
2.4. Introduction of nanoparticle into rubber.....	37

3. Viscoelastic behavior of natural rubber	47
3.1. Coarse-grained molecular dynamics simulation setup	47
3.2. Characterization of viscoelastic property	50
3.3. Dynamic scaling between coarse-grained system and all-atomistic system	51
3.4. Viscoelastic property of natural rubber system	60
4. Hysteresis friction behavior of natural rubber	71
4.1. Characterization of surface roughness.....	71
4.2. Analytical model for hysteresis friction	77
4.3. Frictional behavior of natural rubber system.....	79
4.4. Numerical application: dynamic seal system	90
5. Conclusions and recommendations.....	94
Appendix A. Multiscale modeling of interphase in crosslinked epoxy nanocomposites	96
A.1. Overview	96
A.2. Interfacial nature of crosslinked epoxy with nanofiller	98
A.3. Characterization of interphase property with multiscale modeling	103
A.4. Summary of appendix A	107

Appendix B. Multiscale analysis of load transfer in crosslinked epoxy nanocomposites.....	109
B.1. Overview	109
B.2. Internal stress transfer in interfacial region	111
B.3. Multiscale modeling of load transfer characteristics	115
B.4. Summary of appendix B	119
References	120
Abstract.....	134

List of Figures

Figure 2.1 Illustration of coarse-grained mapping from the all-atomistic model to the coarse-grained model	14
Figure 2.2 Overall schematic of iterative Boltzmann inversion method to derive coarse-grained potential	15
Figure 2.3 (a) Chemical composition of natural rubber (cis-1, 4 Polyisoprene) and (b) full-atomic model of NR	20
Figure 2.4 Coarse-grained mapping of natural rubber: (a) bead connector representation of single natural rubber chain and (b) coarse-grained bulk natural rubber system.	21
Figure 2.5 Derived coarse-grained potential for natural rubber with iterative Boltzmann Inversion: (a) B-B bond, (b) B-B-B angle, and (c) B-B pair.....	22
Figure 2.6 Comparison of structural conformation between the derived coarse-grained model and the representative all-atom model for natural rubber system: (a) bond length distribution of B-B, (b) bending angle distribution of B-B-B, and (c) radial density distribution of B-B pair	24
Figure 2.7 All-atomic model of vulcanized natural rubber; a number of crosslinked rubber molecules are used to establish the representative vulcanized natural rubber system.....	29
Figure 2.8 Coarse-grained mapping scheme for vulcanized rubber: (a) coarse-grained bead connector representation of vulcanized rubber molecule, and (b) coarse-grained	

vulcanized rubber system	30
Figure 2.9 Derived coarse grained bonded potential associated with vulcanizing agent: (a) B-S bond, (b) B-B-S angle, and (c) B-S-B angle	31
Figure 2.10 Derived coarse-grained pair potential potential associated with vulcanizing agent: (a) S-S pair and (b) B-S pair.....	33
Figure 2.11 Comparison of structural conformation between the derived coarse-grained model and the representative all-atom model for vulcanized natural rubber system: (a) bond length distribution of B-S, (b) bending angle distribution of B-B-S, (c) bending angle distribution of B-S-B, (d) radial density distribution of S-S pair, and (c) radial density distribution of B-S pair	34
Figure 2.12 Atomic unit cell configuration of silica-filled rubber nanocomposite	39
Figure 2.13 Coarse-grained mapping scheme for silica-filled rubber nanocomposite: (a) coarse-grained bead connector representation of silica nanoparticle, and (b) coarse-grained natural rubber/silica nanocomposite system.....	40
Figure 2.14 Derived coarse grained bonded potential associated with silica nanoparticle: (a) FF bond and (b) FFF angle	41
Figure 2.15 Simple atomic model to derive F-F pair interaction: 2,000 number of SiO ₂ molecules.....	42
Figure 2.16 Derived coarse-grained pair potential: (a) F-F pair potential and (b) radial density comparison between all-atom (AA) and coarse-grained (CG) model	43
Figure 2.17 Derived coarse-grained pair potential between F and B bead.....	44

Figure 2.18 Comparison of structural conformation between the derived coarse-grained model and the representative all-atom model for nanocomposite system: (a) bond length distribution of F-F, (b) bending angle distribution of F-F-F, and (c) radial density distribution of F-B pair.....	45
Figure 3.1 Dynamic scaling factor of NR1 system for temperature of (a) 263 K, (b) 300 K, and (c) 400 K; the dashed line shows the fitted curve by the equation	
$f_i(t) = 1 + \sum_i a_i (1 - e^{-t/\tau_i})$	55
Figure 3.2 Normalized time-dependent relaxation modulus for (a) 263 K, (b) 300 K, and (c) 400 K from all-atomistic (AA) simulation and from coarse-grained (CC) simulation after applying dynamic time scaling.....	57
Figure 3.3 Time-dependent relaxation modulus of (a) NR1 (10mer) and (b) NR4 (7000mer) with the fitting curve by the generalized Maxwell model	64
Figure 3.4 Relaxation spectrum $G(t)$ of unvulcanized natural rubber system for varying chain length	65
Figure 3.5 Frequency-dependent (a) storage modulus $G'(\omega)$ and (b) loss modulus $G''(\omega)$ with varying chain length; the dynamic modulus is computed with the Fourier transformation of relaxation spectrum $G(t)$	66
Figure 3.6 Comparison of relaxation spectrum $G(t)$ of vulcanized natural rubber system (VR1 and VR2) for different sulfur content with the unvulcanized natural rubber system (NR3).....	67

Figure 3.7 Frequency-dependent (a) storage modulus $G'(\omega)$ and (b) loss modulus $G''(\omega)$ for the vulcanized natural rubber system with varying sulfur content; the dynamic modulus is computed with the Fourier transformation of relaxation spectrum $G(t)$	68
Figure 3.8 Comparison of relaxation spectrum $G(t)$ of silica-filled natural rubber system (FR1 and FR2) for different filler volume fraction with the unvulcanized natural rubber system (NR3)	69
Figure 3.9 Frequency-dependent (a) storage modulus $G'(\omega)$ and (b) loss modulus $G''(\omega)$ for the vulcanized natural rubber system with varying sulfur content; the dynamic modulus is computed with the Fourier transformation of relaxation spectrum $G(t)$	70
Figure 4.1 Height-difference correlation function of a self-affine surface. The values of ξ_{\perp} , ξ_{\parallel} can be obtained from the cross-over point. H is the Hurst exponent.....	75
Figure 4.2 Visualization of the spectral power density as function of the spatial frequency. The exponent β is related to the surface fractal dimension D and to the Hurst exponent ($\beta = 2H + 1 = 7 - 2D$)	76
Figure 4.3 Smooth glass surface profile with the height-different correlation function which represents the surface characteristics with the variables ξ_{\perp} , ξ_{\parallel} , and H	83
Figure 4.4 Mean penetration depth with increasing sliding velocity.....	84
Figure 4.5 Different type of smooth surface: surface 1 with $H = 0.55$, $\xi_{\perp} = 4.42 \mu m$, and $\xi_{\parallel} = 10.0 \mu m$; surface 2 with $H = 0.60$, $\xi_{\perp} = 2.42 \mu m$, and $\xi_{\parallel} = 5.0 \mu m$; surface 3	

with $H = 0.65$, $\xi_{\perp} = 1.05 \mu m$, and $\xi_{ } = 2.0 \mu m$	85
Figure 4.6 Friction coefficient of natural rubber systems with a range of sliding velocity	86
Figure 4.7 Friction coefficient of vulcanized rubber system with a range of sliding velocity at different temperature (260 K, 300 K, and 400 K)	87
Figure 4.8 Effect of microstructural change on frictional behavior: (a) rubber vulcanization and (b) silica nanofiller inclusion	88
Figure 4.9 Frictional master curve with horizontal sliding velocity and normal pressure of natural rubber system: (a) vulcanized rubber and (b) unvulcanized rubber.....	89
Figure 4.10 Schematic description of hydraulic reciprocating O-ring seal system	92
Figure 4.11 Finite element model for O-ring seal.....	92
Figure 4.12 Finite element analysis of O-ring seal system considering the frictional contact: (a) vulcanized and (b) unvulcanized rubber seal	93
Figure A.1 Interfacial interaction energy density of crosslinked epoxy/silica nanocomposites with different crosslink densities	101
Figure A.2 Variation of non-bond characteristics (a) between epoxy molecules and silica, and (b) between N-C-O atoms and silica with crosslinking reaction	102
Figure A.3 Overall schematic of the multiscale modeling of the interphase property; blue-colored terms (For interpretation of the references to color in this figure legend, the reader is referred to the web version of the article.) indicate the values predicted from the multi-inclusion model.....	106
Figure B.1 Stress strain response of each phase (SiC particle and epoxy matrix) with	

varying crosslinking conversion: (a) 3% and (b) 5% of filler volume fraction..... 114

Figure B.2 Comparison of particle stress with strain between finite element model and molecular dynamics simulation: (a) 3% and (b) 5% of filler volume fraction..... 118

List of Tables

Table 2.1 Detailed composition of all atom (AA) and coarse-grained (CG) model for bulk natural rubber and density of equilibrated system.....	26
Table 3.1 Detailed composition of coarse-grained (CG) natural rubber system and equilibrium density at 300 K and 1 atm	49
Table 3.2 Comparison of instantaneous shear modulus from all-atomistic MD and CG MD simulation with the scaling parameter for relaxation modulus (f_G).	59

1. Introduction

1.1. Rubber friction

Frictional phenomena are of critical importance in almost every engineering application. Especially for engineering components with using elastomers, such as seals, tires, and bearing, these parts are prevalently exposed to finite deformations depending on various operating conditions in contact with other moving parts. Without a proper consideration on the frictional characteristics, many severe engineering problems involving friction-induced vibrations or system failure can occur. Unlike other engineering materials, the impact of deformations induced by the contact surface is relatively significant due to the distinct viscoelastic nature of elastomers. The finite deformations of elastomer from the relative motion at the contact surface generate the internal energy dissipation, which is one of key components to describe the frictional feature of elastomers. Thus, when it comes to dealing with the frictional contact of elastomer with other surfaces, a process inside the bulk medium needs to be taken into account, which implies a significant dependency on the material characteristics and the nature of the contact surfaces¹⁻¹⁴.

The investigation of frictional contact of elastomer materials with rough surfaces is challenging issue due to the complexity of frictional phenomenon which is associated with various components: macro geometry, detailed surface micro-topology,

relative tangential velocity, cleanliness of surface, temperature, material and surface properties of moving bodies, applied normal load, filler material and content, lubricant and its additives, and surface treatment/coating of harder counterpart⁷. Moreover, those sophisticated interactions encompass a wide range of length scale¹³. In order to describe these phenomena which actually occur at different length scales, multi-scale approaches have been introduced which applies the finite element (FE) method as the numerical simulation tool^{1, 3-4, 15-16}.

For the implementation of numerical simulations on frictional problems, Coulomb's law is prevalently employed which implies a constant friction coefficient with respect to material pairing. This assumption is reasonable and sufficient for many applications in solid mechanics. In the case of rubber friction, however, due to the extreme deformations of rubber materials under frictional contact and the sophisticated communication at the contact surface, Coulomb's law is not sufficient to describe the frictional processes of elastomers. Thus, to reflect the complex nature at the contact surface of elastomer with the harder counterpart, the fundamental frictional components of elastomers, hysteresis and adhesion friction, have been taken into account for the detailed numerical approaches^{1-3, 13, 17-18}.

The hysteretic friction is attributed to the dissipation of energy during cyclic deformations of the sliding rubber due to the surface asperities. The internal energy dissipation associated with damping effects within a viscoelastic body leads to a global horizontal frictional force. Thus, the combination of excitation frequencies due to the

rough surface and the material relaxation parameters affects the resulting friction coefficient. Adhesional effects are caused by the intermolecular attractive forces between the contact partners. Under wet conditions, it is generally agreed that the adhesion component of the total frictional effect is drastically reduced, whereas the hysteresis loss remains largely unaffected^{1, 19}. Therefore, in the present work the hysteresis friction is considered as a dominant contribution on the overall frictional behavior of rubber.

1.2. Viscoelastic nature of polymer

Natural rubber (NR) has been of great interest due to its many useful properties, such as high tensile strength, high elasticity, flexibility, good crack growth resistance and low heat build-up. Primarily due to its unique viscoelastic properties, rubber finds use in engineering products or structural components, such as tire treads, tank pads, building mounts, and automotive suspensions, where the dynamic behavior of filled rubber is of key importance²⁰⁻²⁶. The viscoelastic behavior of polymers is characterized by dynamic mechanical analysis. The dynamic mechanical properties are usually expressed in terms of the storage (the in-phase) and loss (the out-of-phase) modulus. Storage modulus is the immediate response to the application of force, whereas the loss modulus represents the energy dissipated as heat. Dynamic mechanical parameters have been used to determine the glass-transition region, relaxation modulus, degree of crystallinity, molecular orientation, crosslinking, phase separation, and so forth. Knowledge of the viscoelastic

properties of polymeric materials is important because most critical engineering applications are a combination of storage and loss modulus that dictate the failure of a polymer and its toughness under a given deformation history^{20, 27-42}.

Over different spans of time, numerous researches have established that the dynamic mechanical behavior depends remarkably on the different types of rubbers, fillers, the existence of interactions between filler and rubber matrix, strain magnitude, frequency, and temperature⁴³. However, the viscoelastic rheological characteristics of both uncured and cured elastomers filled with nanofillers are still lacking.

1.3. Viscoelastic property with molecular dynamic simulation

The development of a computational platform that can predict high-frequency viscoelastic properties from polymer chemistry and microstructure is thus motivated to improve the understanding of the viscoelastic properties of thermos-rheologically complex polymers^{27-28, 32, 34, 40, 42, 44-45}. However, creating such a platform remains a formidable task due to the wide range of spatial and temporal scales over which stress relaxation occurs. One approach toward bridging molecular simulations with macroscopic response is through hierarchical multiscale methods, where physical parameters of theoretical models are estimated from atomistic simulations. This approach was recently demonstrated by Li et al.⁴¹ to predict the viscoelastic properties of polyisoprene by combining atomistic and CG simulations with primitive chain analysis to

extract the parameters of the tube model of primitive paths, which is then bridged to a finite strain constitutive law. For more complex system with the reinforcing fillers, Chen et al.⁴⁶ provided an insight on the role of polymer–particle interactions in the strain-dependent viscoelasticity, by studying the cross-linked elastomeric systems containing various concentrations of monodispersed nanoparticles with different interfacial interactions via coarse-grained molecular dynamics simulation. Chen concluded the two important factors contributing to the “Payne effect” of filled elastomers, such as the breakage of the rigid polymer shell around nanoparticle and the rearrangement of polymer-shell-bridged nanoparticle network under oscillatory shear. While in the case of low loading the debonding of polymer monomers from the NP surfaces as well comes into play. Raos et al.⁴⁷ used the coarse-grained DPD simulation to study the change of the storage modulus of filled elastomers under the oscillatory shear flow. They observed a strain stiffening of the material (antiPayne behavior), different from those observed experimentally.

Some simulation works have been carried out to investigate the viscoelastic nature of polymer^{27-28, 34, 41}, however, the understanding of dynamic properties of polymer with the consideration of structure-property relationship is still limited.

1.4. Outline of the thesis

The aim of this study is to predict the viscoelastic characteristics of rubber and

the frictional behavior when sliding on a rough surface. Herein, a systematic simulation framework is proposed from the atomistic scale to the continuum regime, since the viscoelastic and frictional phenomena occur across a wide range of time and length scale.

In order to capture the viscoelastic nature of rubber, molecular dynamic simulation is employed. The applicable scales in terms of time and length are enlarged with using a coarse-grained mapping scheme. Structure-based bottom-up approach is used to derive the coarse-grained potential, and various rubber systems with the consideration of chain length, vulcanization, and reinforcing filler is studied.

Based on the viscoelastic characteristics obtained from the coarse-grained molecular dynamic simulation, the frictional behavior of rubber is examined. The self-affine surface model is employed to describe the random surface. Effects of length scale in the roughness of surface are captured by the power spectrum density in a spatial frequency domain. Numerical analysis is carried out to predict the frictional behavior, especially hysteresis friction contribution.

The detailed procedures and results are addressed in this dissertation that is organized as follows. **Chapter 2** provides the coarse-grained mapping method from the atomistic configuration to the coarse-grained domain. Based on the structural consideration of atomistic model, the coarse-grained potentials are derived and validated with their atomic counterparts. **Chapter 3** focuses on the viscoelastic nature of natural rubber system via coarse-grained molecular dynamic simulations. Variations of structural morphology are considered in terms of chain length, sulfur-induced vulcanization, and

silica nanofiller. The relaxation behavior and dynamic modulus are studied. **Chapter 4** demonstrates the procedure to examine the frictional characteristics when the rubber sliding on a rough surface. Hysteresis friction is captured which is attributed to the internal energy dissipation at the contact surface. **Chapter 5** summarizes the concluding remarks and outlines some future challenges.

2. Coarse-grained Modeling Methodology

2.1. Overview of coarse-grained molecular dynamics

Coarse-grained models provide an efficient means to simulate and investigate systems in which the desired behavior, property, or response is inherently at the mesoscale; those that are both inaccessible to full atomistic representations and inapplicable to continuum theory^{20, 48-64}. Granted, a developed coarse-grain model can only reflect the behavior included in their governing potentials and associated parameters, and consequently, the source of such parameters typically determines the accuracy and utility of the coarse-grain model. Hierarchical connection at each scale is crucial to predict structure–property relationships, to provide fundamental mechanistic understanding, and to enable predictive modeling and material optimization to guide synthetic design efforts. Indeed, a finer-trains-coarser approach is not limited to bridge atomistic to mesoscopic scales (which is the focus of the current discussion), but can also

refer to hierarchical parameterization transcending any scale, such as mesoscopic to continuum levels. Such a multiscale modeling paradigm establishes a fundamental link between atomistic behavior and the coarse-grain representation, providing a consistent theoretical approach to develop coarse-grain models for systems of various scales, constituent materials, and intended applications.

2.2. Iterative Boltzmann inversion

As a typical structure-based CG method, the Iterative Boltzmann inversion (IBI) provides effective ways to calibrate potentials between CG beads, aiming that the resulting equilibrium conformational distributions of CG system match the target distributions computed from the full-atomic MD simulations^{20, 63, 65-66}.

The atomically detailed coordinates in the all-atomistic system with n atoms are described by the set of Cartesian vectors, $\mathbf{r}^n = \{\mathbf{r}_1, \mathbf{r}_2, \dots, \mathbf{r}_n\}$, as illustrated in **Figure 2.1**. With the inter-atomic potential, $u(\mathbf{r}^n)$, the canonical equilibrium distribution function at the given volume, V , and temperature, T , is:

$$p_r(\mathbf{r}^n) = \frac{1}{z_n} \exp(-u(\mathbf{r}^n)/k_B T) \quad (2.1)$$

where $z_n = z(n, V, T) = \int d\mathbf{r}^n e^{-u(\mathbf{r}^n)/k_B T}$ is the canonical configurational integral over all atomic coordinates, the partition function, and k_B is the Boltzmann constant. By grouping a number of atoms into one super atom, CG bead, the atomic configuration can

be mapped into the CG model consisting of N beads. Herein, N CG sites are represented with the Cartesian vectors, $\mathbf{R}^n = \{\mathbf{R}_1, \mathbf{R}_2, \dots, \mathbf{R}_N\}$, as shown in **Figure 2.1**. Based on the relationship between \mathbf{r}^n and

\mathbf{R}^N , the corresponding mapping operator $\mathbf{M}_{\mathbf{R}}^N$ can be derived as the following:

$$\mathbf{R}^N = \mathbf{M}_{\mathbf{R}}^N(\mathbf{r}^n) = \{\mathbf{M}_{\mathbf{R}_1}(\mathbf{r}^n), \mathbf{M}_{\mathbf{R}_2}(\mathbf{r}^n), \dots, \mathbf{M}_{\mathbf{R}_N}(\mathbf{r}^n)\} \quad (2.2)$$

Similar to the approach used in the atomic configuration, with the inter-bead potential, $U(\mathbf{R}^N)$, the canonical probability distribution for the given CG configurations, V and T is:

$$P_R(\mathbf{R}^N) = \frac{1}{Z_N} \exp\left(\frac{-U(\mathbf{R}^N)}{k_B T}\right) \quad (2.3)$$

where $Z_N = Z(N, V, T) = \int d\mathbf{R}^N e^{-U(\mathbf{R}^N)/k_B T}$ is the canonical partition function of the

CG system. In order to match the equilibrium conformational distributions of the CG system with the atomic counterpart, the following condition should be satisfied,

$$P_R(\mathbf{R}^N) = p_R(\mathbf{R}^N) \quad (2.4)$$

where $p_R(\mathbf{R}^N) = \int d\mathbf{r}^n p_r(\mathbf{r}^n) \delta(\mathbf{R}^N - \mathbf{M}_{\mathbf{R}}^N \mathbf{r}^n)$ is the equilibrium CG conformational distribution. Throughout the process, the relationship between the potential functions for both systems, $u(\mathbf{r}^n)$ and $U(\mathbf{R}^N)$, can be derived as the following:

$$e^{-U(\mathbf{R}^N)/k_B T} = \frac{Z_N}{z_n} \int d\mathbf{r}^n e^{-u(\mathbf{r}^n)/k_B T} \delta(\mathbf{R}^N - \mathbf{M}_{\mathbf{R}}^N \mathbf{r}^n) \quad (2.5)$$

From the relationship in Eq. (2.5), it is clearly noted that the derived CG potential, $U(\mathbf{R}^N)$, is different with the conventional potential function.

The probability density distribution function of the all-atomistic system, $p_r(\mathbf{r}^n)$, can be obtained from the representative trajectories of full-atom MD simulations. The potential function of the CG system is defined as,

$$U(\mathbf{R}^N) = -k_B T \ln p_R(\mathbf{R}^N) \quad (2.6)$$

In general, the probability distribution function can be expressed by the following conformational quantities: bond length, l , bending angle, θ , dihedral angle, ψ , and pair distance, r . With the assumption that those variables are independent each other, the probability distribution can be written as the following:

$$p_R(\mathbf{R}^N) = p_R(l, \theta, \psi, r) = p_R(l)p_R(\theta)p_R(\psi)p_R(r) \quad (2.7)$$

The potential function for the CG system then can be defined as,

$$U(\mathbf{R}^N) = U(l, \theta, \psi, r) = U(l) + U(\theta) + U(\psi) + U(r) \quad (2.8)$$

$$\begin{aligned} U_{bonded} &= U(l) + U(\theta) + U(\psi) \\ U_{nonbonded} &= U(r) \end{aligned} \quad (2.9)$$

where U_{bonded} and $U_{nonbonded}$ refer to the bonded and non-bonded interactions.

● Bonded potential

The probability density distribution function of the bonded terms, $p_R(q)$ with $q = l, \theta, \psi$ (bond length, bending angle, and dihedral angle), can be obtained from the CG coordinates mapped from the all-atomistic representative trajectories. Thus, the CG potential for the bonded terms is derived as the followings:

$$\begin{aligned}
U(l) &= -k_B T \ln \left(\frac{p_R(l)}{l^2} \right) \\
U(\theta) &= -k_B T \ln \left(\frac{p_R(\theta)}{\sin(\theta)} \right) \\
U(\psi) &= -k_B T \ln(p_R(\psi))
\end{aligned} \tag{2.10}$$

To parameterize the CG potential with a specific analytic function, the multi-centered Gaussian function is implemented. The CG potential for the bonded terms is fitted by a sum of the Gaussian functions, then can be expressed as:

$$\begin{aligned}
U(l) &= -k_B T \ln \left[\sum_{i=1}^n a_i \exp \left\{ -\left(\frac{l-l_i}{b_i} \right)^2 \right\} \right] \\
U(\theta) &= -k_B T \ln \left[\sum_{i=1}^n a_i \exp \left\{ -\left(\frac{\theta-\theta_i}{b_i} \right)^2 \right\} \right] \\
U(\psi) &= -k_B T \ln \left[\sum_{i=1}^n a_i \exp \left\{ -\left(\frac{\psi-\psi_i}{b_i} \right)^2 \right\} \right]
\end{aligned} \tag{2.11}$$

where l_i , θ_i , and ψ_i are the center positions of the i -th Gaussian functions (for bond length, bending angle, dihedral angle, respectively), and a_i and b_i are fitting constants. In practice, the dihedral term in the bonded CG potential is prevalently neglected considering its marginal effect compared to other bonded terms associated with bond stretch and bending. In that regard, the dihedral potential in CG model is not considered in the present work.

● Non-bonded potential

To account the probability density distribution of pair distance, $p_R(r)$, in the

system, the radial distribution function (RDF) is computed from the CG reference trajectories obtained from the all-atomistic MD simulations. Herein, an initial guess for the non-bonded potential, $U^0(r)$, is set from the Boltzmann inversion of the RDF, $g(r)$, computed from the representative trajectories;

$$U^0(r) = -k_B T \ln(g(r)) \quad (2.12)$$

With the initial guess for the CG pair, the RDFs of resulting CG system, $g^0(r)$, do not reproduce the target conformational distribution of the pair distance, $g(r)$. It is generally because of the fact that many-body interactions are not fully taken into account in the CG system. To calibrate the CG pair potential, the potential is modified as

$$U^1(r) = U^0(r) - \alpha k_B T \ln\left(\frac{g^0(r)}{g(r)}\right) \quad (2.13)$$

where α is an adjustable correction factor for a better correction convergence. The calibration is performed iteratively, the i -th step of pair potential modification process is written with the target function, f_{target} , which represents the degree of convergence, as the followings:

$$U^{i+1}(r) = U^i(r) - \alpha k_B T \ln\left(\frac{g^i(r)}{g(r)}\right) \quad (2.14)$$

$$f_{target}^i = \int_0^{r_c} w(r) \{g(r) - g^i(r)\}^2 dr \quad (2.15)$$

where r_c is the cut-off distance for the pair distance of RDF (2.0 nm in this work), and $w(r) = \exp(-r)$ is a weighting function to penalize deviations at small distances⁶⁶.

During the CG potential updating procedure, the resulting pressure of CG system is also

monitored. Even after matching the system conformation represented by the RDF, the pressure computed from the CG model might be different with the representative system, resulting in reproducing a different system density. To resolve the issue related to the system pressure, the pressure correction, $\Delta U_{pc}(r)$, is considered with the implementation of linear tail function:

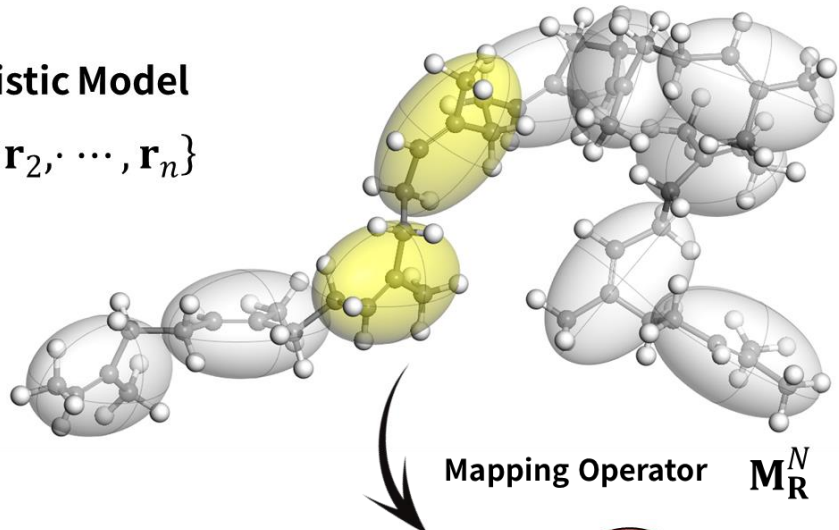
$$\Delta U_{pc}(r) = \beta k_B T \left(1 - \frac{r}{r_c} \right) \quad (2.16)$$

where the value of β depends on the deviation from the target pressure; a negative value when the resulting CG pressure is higher than the target pressure, and a positive value for the opposite case. Plus, the absolute value of β is also tuned considering the level of deviation from the target pressure.

The continuous iterations are proceeded to match the RDF and the resulting equilibrium density with the target system using potential modifications and pressure corrections (Eq. (2.16)). The convergence criteria are checked with the target function and the equilibrium pressure of CG model, where the order of the target function is $f_{target} \approx 1.0 \times 10^{-5}$ and the equilibrium pressure is 1 atm. The overall schematic view of IBI method is illustrated in **Figure 2.2**.

All-atomistic Model

$$\mathbf{r}^n = \{\mathbf{r}_1, \mathbf{r}_2, \dots, \mathbf{r}_n\}$$



Coarse-grained Model

$$\mathbf{R}^N = \{\mathbf{R}_1, \mathbf{R}_2, \dots, \mathbf{R}_N\}$$

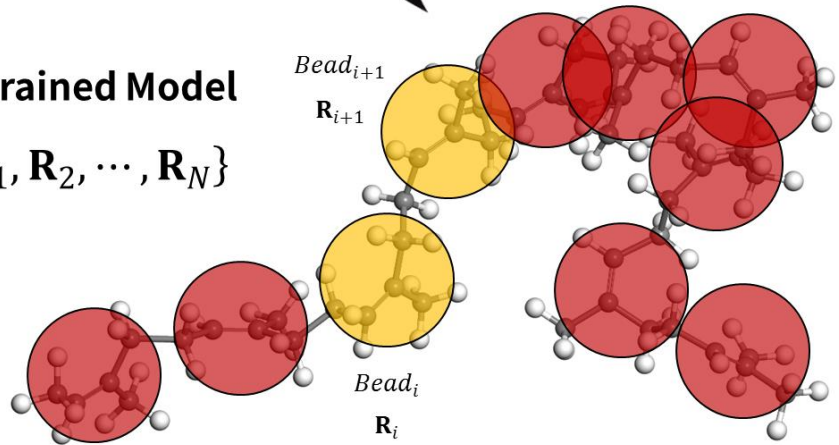


Figure 2.1. Illustration of coarse-grained mapping from the all-atomistic model to the coarse-grained model.

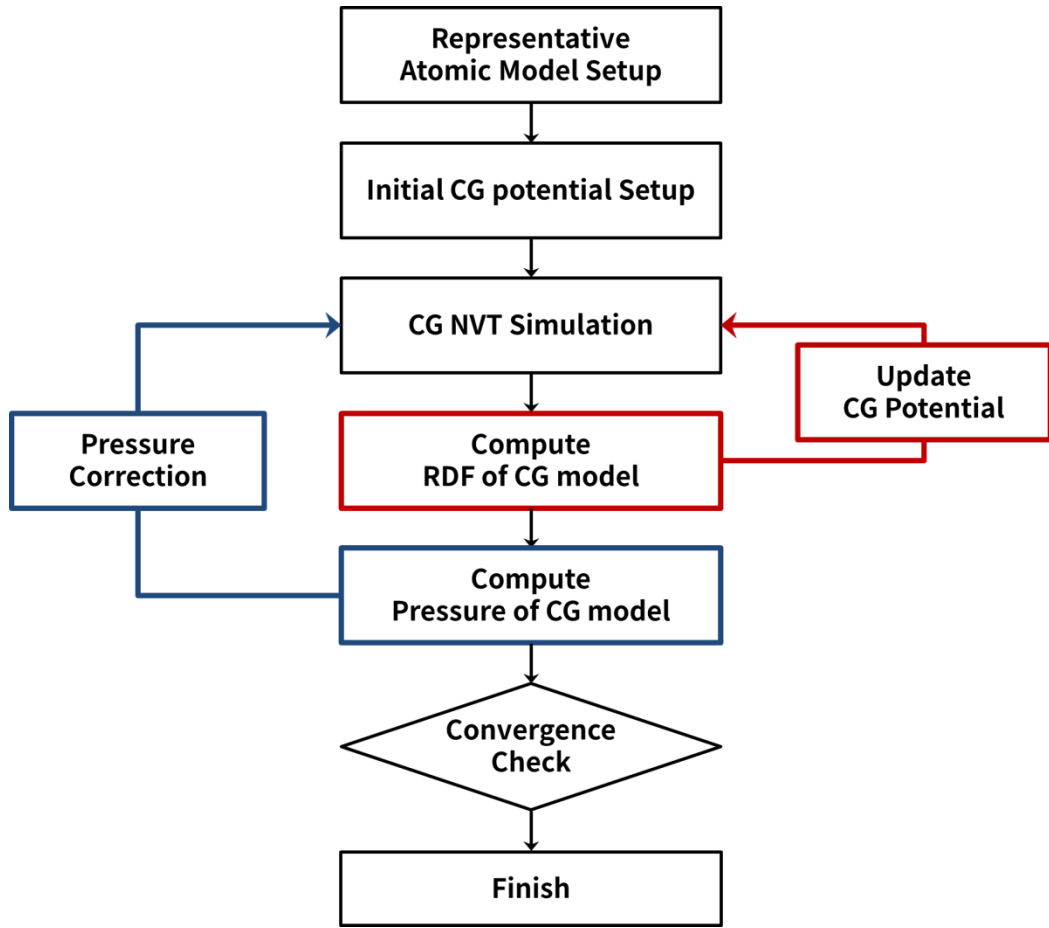


Figure 2.2. Overall schematic of iterative Boltzmann inversion method to derive coarse-grained potential.

2.3. Coarse-grained modeling of rubber system

This section introduces the detailed procedure for establishing the CG potential of NR systems, consisting of three steps: (1) preparing proper full-atomic models as the representative model of a target system, (2) mapping of the atomic structures into CG particle systems and (3) deriving new interbead interactions between CG particles. The representative atomic models were properly constructed with the aid of commercial molecular simulation software, Materials Studio⁶⁷. For full-atomic MD simulations, PCFF (*polymer consisting force field*) was used to describe the interactions between individual atoms. The iterative ensemble simulations for CG models required during the IBI procedure were conducted using the Mesocite module of Materials Studio. The initial configurations for CG models were modeled with the aid of Mesostructure Template module in Materials Studio. The desired ensemble simulations and the production runs for the CG models were conducted using LAMMPS (Large-scale Atomic/Molecular Massively Parallel Simulator)⁶⁸, developed at Sandia National Laboratories.

2.3.1. Coarse-grained potential for bulk natural rubber

IBI method is basically based on the representative atomic model. First of all, the full-atomic model of bulk NR was prepared from the chemical structure (*cis*-1, 4

Polyisoprene). The initial atomic model with 100 NR chains (10 monomers per each chain) was established using the Amorphous module in Materials Studio at the target density of 0.7 g/cm³ and a periodic boundary condition was imposed. The chemical composition and the full-atomic NR model are shown in **Figure 2.3**. The initial model consisting of 13,200 atoms was equilibrated first at an elevated temperature of 500 K with 2 ns of NVT (isothermal) ensemble. Then, the NR system was relaxed using 2 ns of NVT ensemble at 300 K followed by 5 ns of NPT (isothermal-isobaric) ensemble at 300 K and 1 atm condition. From the equilibrated model, a production run was conducted with NVT ensemble at 300 K for 1 ns and 2,000 trajectories were stored for every 500 fs to obtain the reliable distributions of bonds, angles, and the radial density distribution functions (RDF) of the representative model. The ensembles of full-atomic MD simulations were carried out with the time step of 1 fs.

The initial CG model of NR was prepared by mapping the monomers into the equivalent super atoms. The center of mass of each monomer of the equilibrated full-atomic NR system was replaced by B bead. The mass was defined as the summation of mass of associated atoms for each monomer. The connectivity between NR monomers was described with the bead connectors. The mapping scheme for bulk NR system is shown in **Figure 2.4**.

From the representative atomic trajectories, the probability density distributions of bonded terms (bond length of B-B and bending angle of B-B-B) were calculated and the bonded CG potentials were derived using BI (Eq. (2.11)) with implementing the

multi-centered Gaussian functions for fitting. The initial guess for the non-bonded CG pair potential (B-B pair) were derived from the RDF computed in the representative atomic trajectories. With the bonded CG potential and the initial guess for B-B pair, the iteration process was proceeded to match the RDF of CG system with that of the representative atomic model as described in the previous section of 2.2. The derived bonded CG potential and the final non-bond CG potential for the bulk NR system were shown in **Figure 2.5**.

After the convergence of non-bond CG potential was made, 10,000 frames of CG trajectories during 10 ns with the time step of 1 fs were stored with using the final CG potential (**Figure 2.5**) computed via IBI method. From the CG trajectories, the probability density distributions of bonded terms and the RDF were calculated and compared with those from the representative atomic trajectories. **Figure 2.6** clearly shows that the structural conformation in terms of both bonded and non-bond terms are reasonably reproduced with the present CG potential as intended in IBI scheme.

To compare the system density with the atomic counterparts, NR systems for both full-atomic and CG models with varying chain length were modeled. The atomic models were equilibrated at 300 K and 1 atm with using the same manner applied previously for the representative atomic system. Using the present CG potential for NR, the CG models were equilibrated; 25 ns of NVT ensemble at an elevated temperature of 500 K, and 25 ns of NVT ensemble at 300 K followed by 50 ns of NPT at 300 K and 1 atm with the time step of 5 fs. The detailed compositions of both atomic and CG NR

systems are described in **Table 2.1** with the comparison of system densities computed from the final equilibrated models.

As far as the structural features and the system density at 300 K and 1 atm condition are concerned, the comparison results (**Figure 2.6 and Table 2.1**) clearly demonstrate that the present CG potential can successively replicate the structural conformation of NR in the CG MD environment.

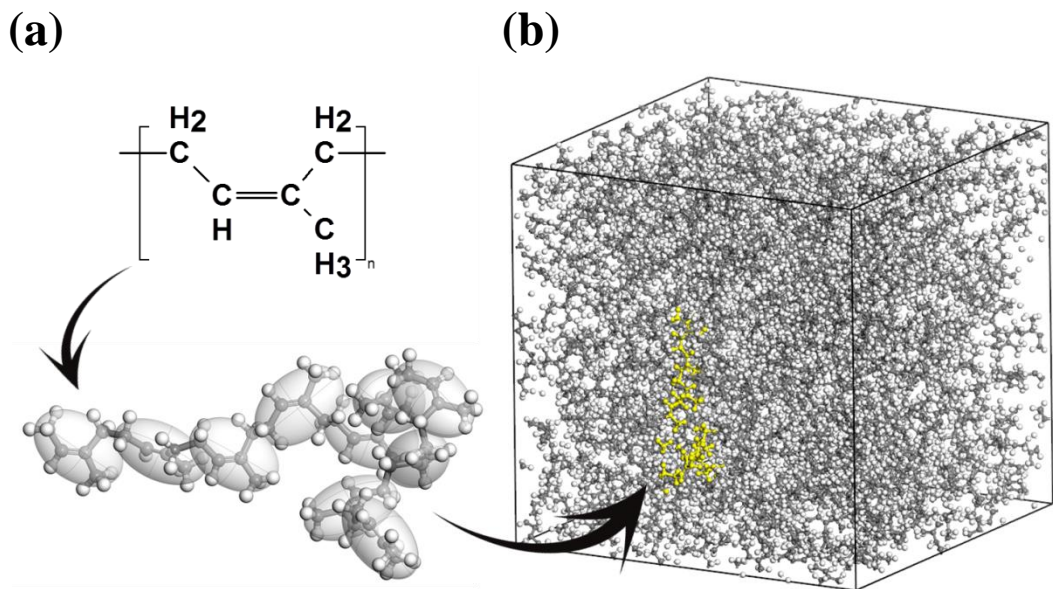
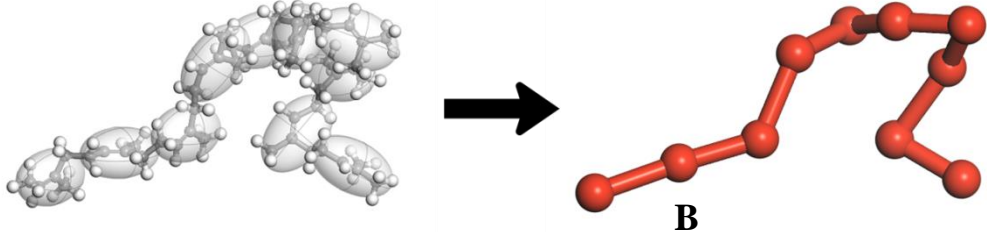


Figure 2.3. (a) Chemical composition of natural rubber (*cis*-1, 4 Polyisoprene) and (b) full-atomic model of NR.

(a)



(b)

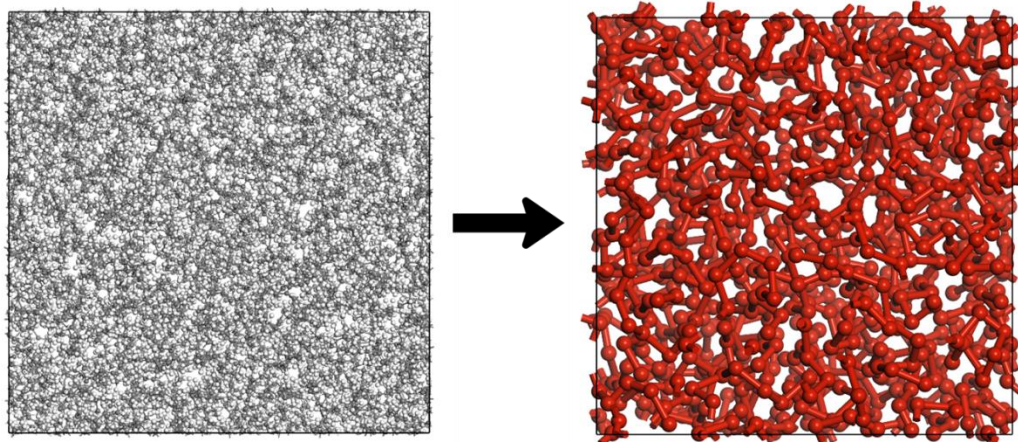
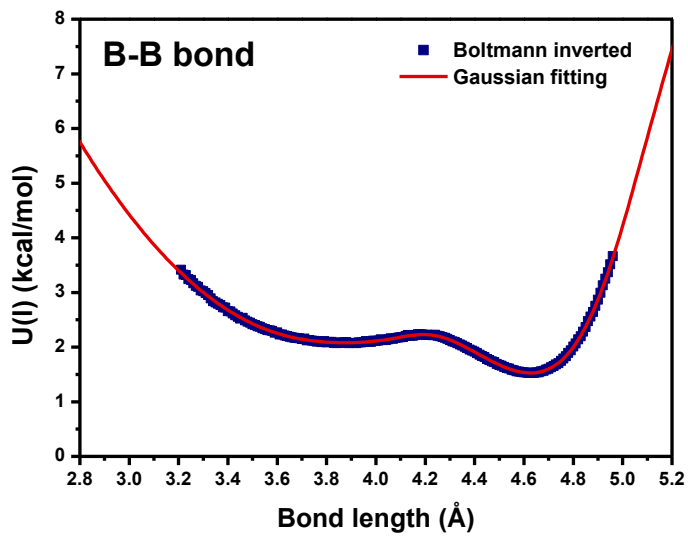
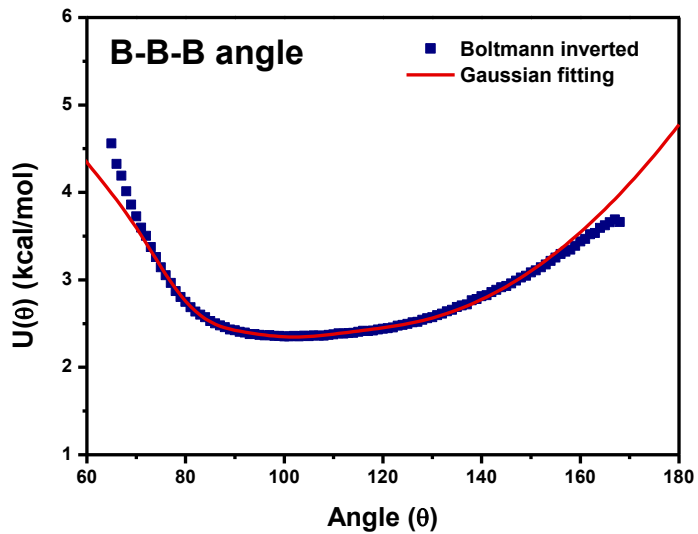


Figure 2.4. Coarse-grained mapping of natural rubber: (a) bead connector representation of single natural rubber chain and (b) coarse-grained bulk natural rubber system.

(a)



(b)



(c)

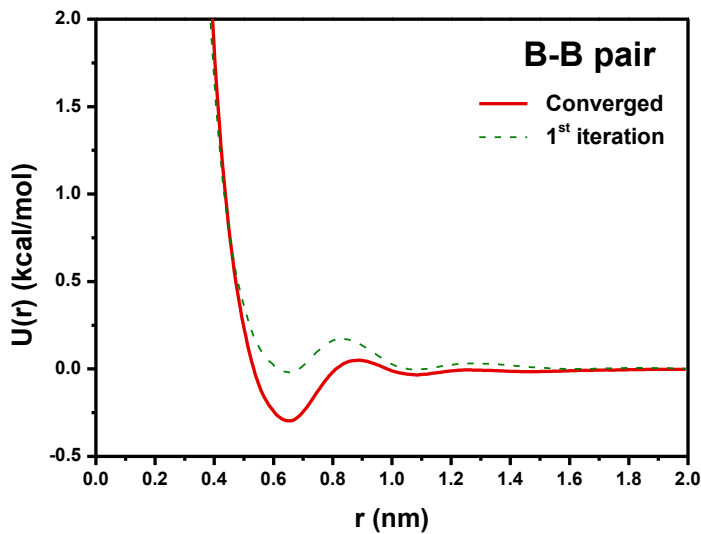
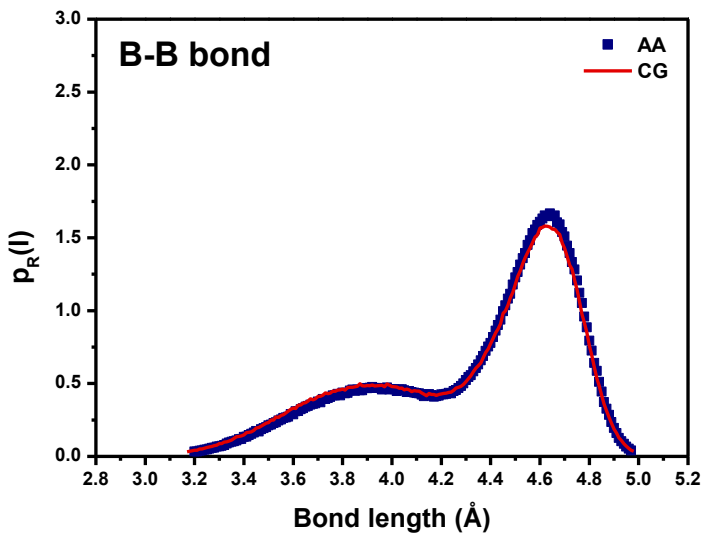
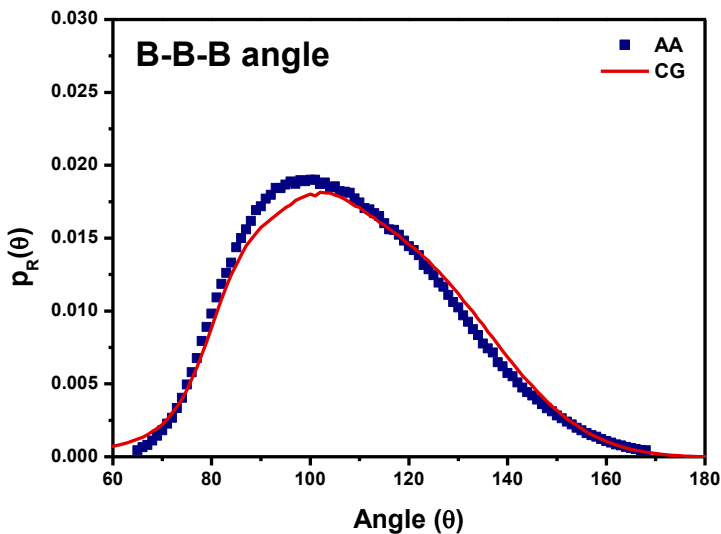


Figure 2.5. Derived coarse-grained potential for natural rubber with iterative Boltzmann Inversion: (a) B-B bond, (b) B-B-B angle, and (c) B-B pair.

(a)



(b)



(c)

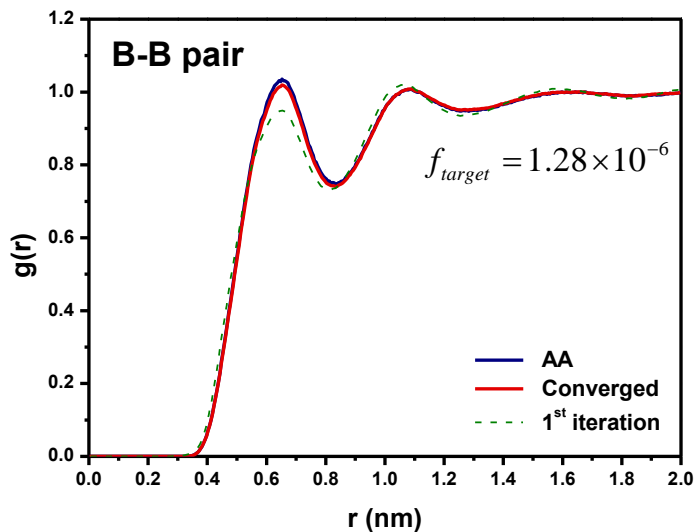


Figure 2.6. Comparison of structural conformation between the derived coarse-grained model and the representative all-atom model for natural rubber system: (a) bond length distribution of B-B, (b) bending angle distribution of B-B-B, and (c) radial density distribution of B-B pair.

Table 2.1. Detailed composition of all atom (AA) and coarse-grained (CG) model for bulk natural rubber and density of equilibrated system.

No. of monomers	Composition of unit cell					Density (g/cm ³)	
	AA		CG			AA	CG
	No. of chains	No. of atoms	Cell length (Å)	No. of chains	No. of beads		
10	100	13,200	51.96	3,536	35,360	172.01	0.8089 0.7861
100	20	26,040	64.63	354	35,400	167.89	0.8387 0.8464
200	10	26,020	64.56	164	32,800	163.45	0.8413 0.8497
300	7	27,314	65.66	109	32,700	163.21	0.8404 0.8510
500	4	26,008	64.54	71	35,500	167.48	0.8418 0.8521
1000	2	26,004	64.55	35	35,000	166.84	0.8422 0.8527

2.3.2. Coarse-grained modeling of rubber vulcanization

Rubber vulcanization is a chemical reaction associated with sulfur additives to produce crosslink junctions between rubber chains. To derive the CG potential for the vulcanized NR system, the initial atomic model was prepared; 96 NR chains (10 monomers per each chain) and 48 sulfur atoms. Herein, a single sulfur atom was considered as a vulcanizing agent. The sulfur atoms produce crosslinks between NR chain, forming vulcanized networks as shown in **Figure 2.7**. The atomic model for vulcanized NR was relaxed at 300 K and 1 atm condition with the same manner used in the NR system previously. From the equilibrated atomic configuration, 2,000 frames of representative atomic trajectories for the vulcanized NR system were stored during 1 ns of NVT ensemble at 300 K.

To establish the CG bead system, the NR chains were mapped with the same mapping scheme used in the bulk NR system. The vulcanizing agents, single sulfur atoms, were replaced by S beads and the crosslinking junctions between the NR chains and sulfur was represented with B-S bead connectors. The mapping scheme for the vulcanized NR system is shown in **Figure 2.8**.

From the representative trajectories of vulcanized NR system, the probability density distributions for the newly-introduced bonded terms were computed: B-S bond, B-B-S angle, and B-S-B angle. Then, the bonded CG potentials were derived as shown in **Figure 2.9**. With the obtained bonded CG potentials, IBI method was applied to compute

the non-bond CG potentials. The iterations to match the RDF of S-S and B-S pair and the system density for the vulcanized NR system were carried out following the IBI scheme.

The converged non-bond CG potentials are shown in **Figure 2.10**.

Once the convergence was achieved, the probability density distributions and the RDFs were compared with the all-atomic reference, as shown in **Figure 2.11**. Plus, the equilibrium density of CG system was compared with that of the atomic representative model: 0.8305 g/cm³ of the CG model and 0.8391 g/cm³ of the representative atomic model.

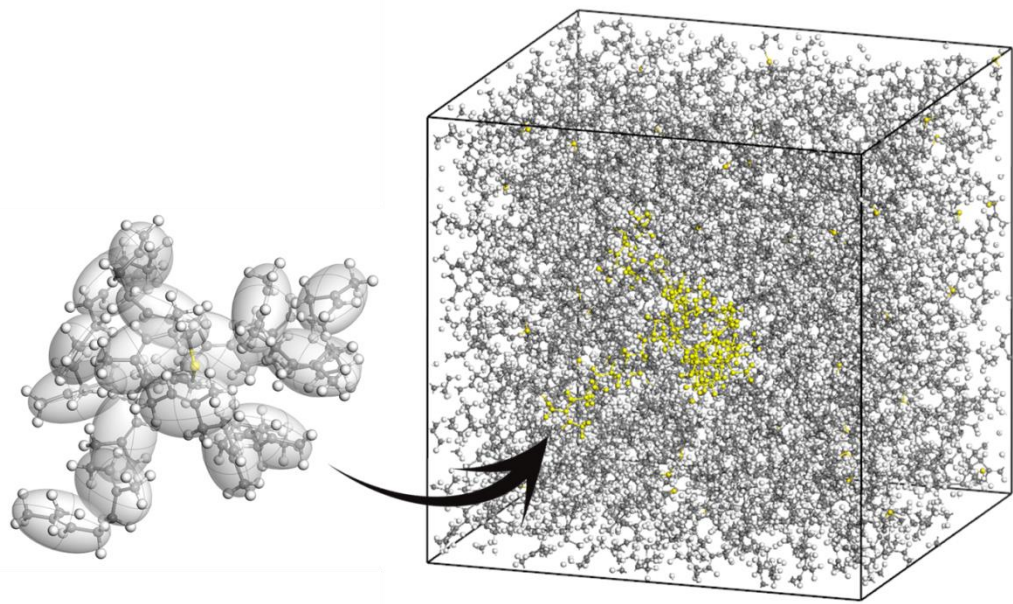
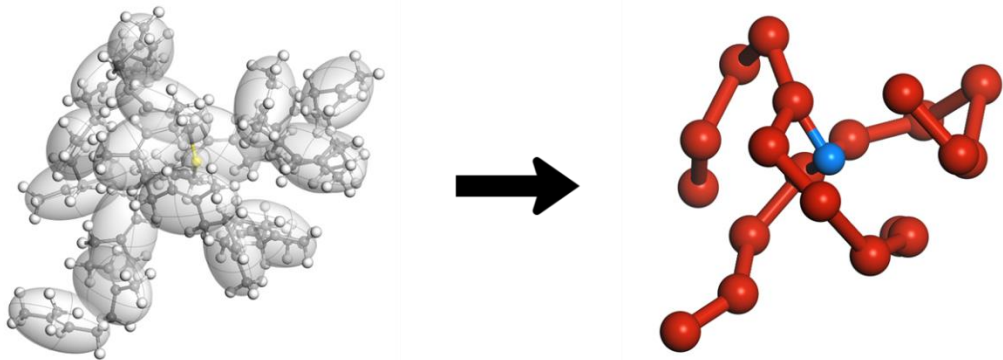


Figure 2.7. All-atomic model of vulcanized natural rubber; a number of crosslinked rubber molecules are used to establish the representative vulcanized natural rubber system.

(a)



(b)

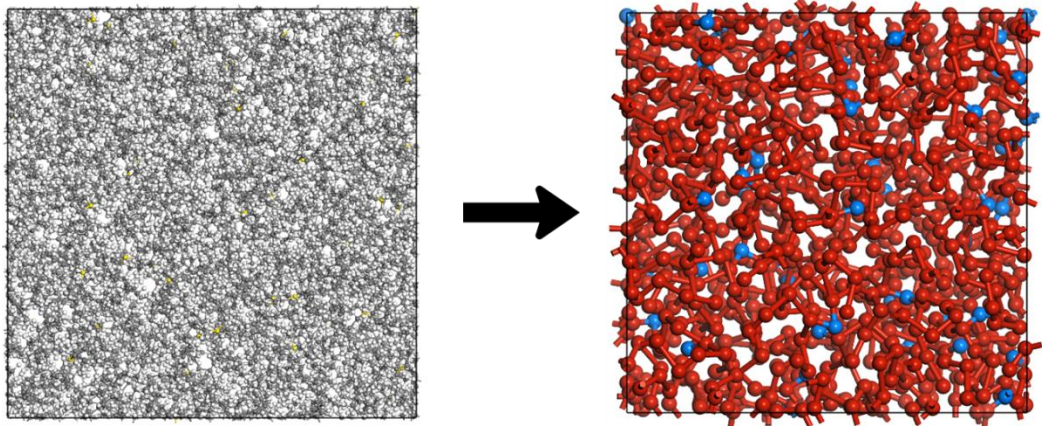
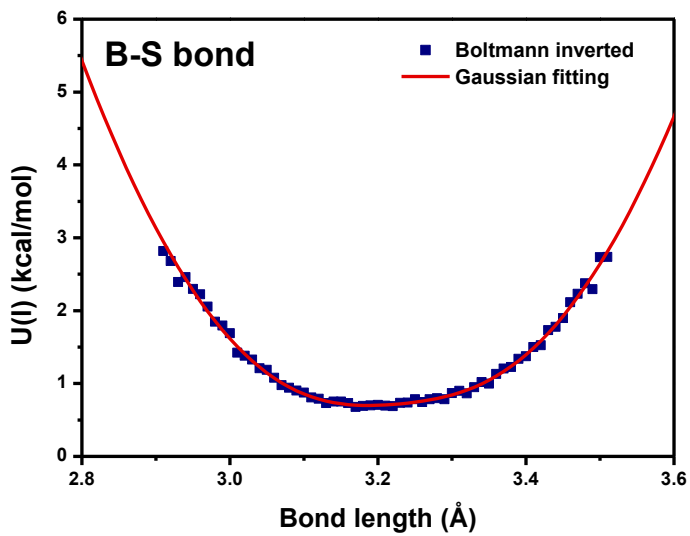
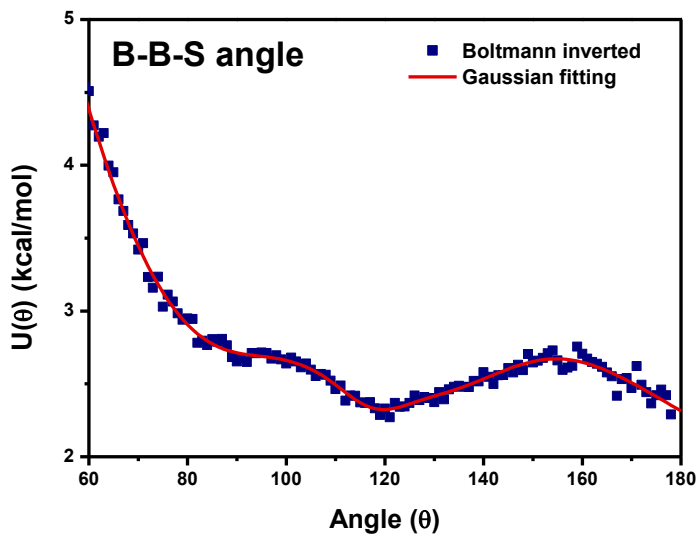


Figure 2.8. Coarse-grained mapping scheme for vulcanized rubber: (a) coarse-grained bead connector representation of vulcanized rubber molecule, and (b) coarse-grained vulcanized rubber system.

(a)



(b)



(c)

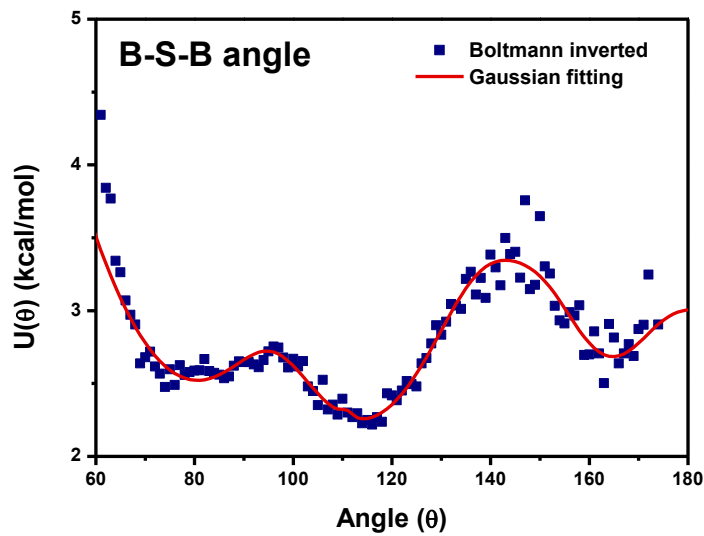
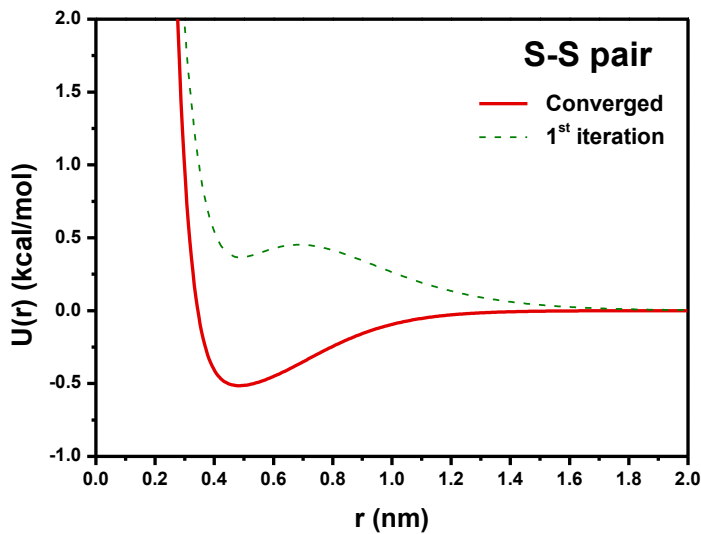


Figure 2.9. Derived coarse grained bonded potential associated with vulcanizing agent: (a) B-S bond, (b) B-B-S angle, and (c) B-S-B angle.

(a)



(b)

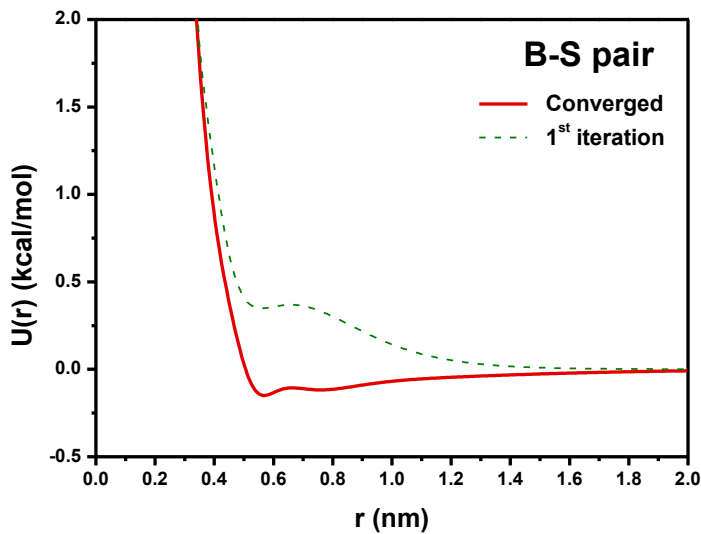
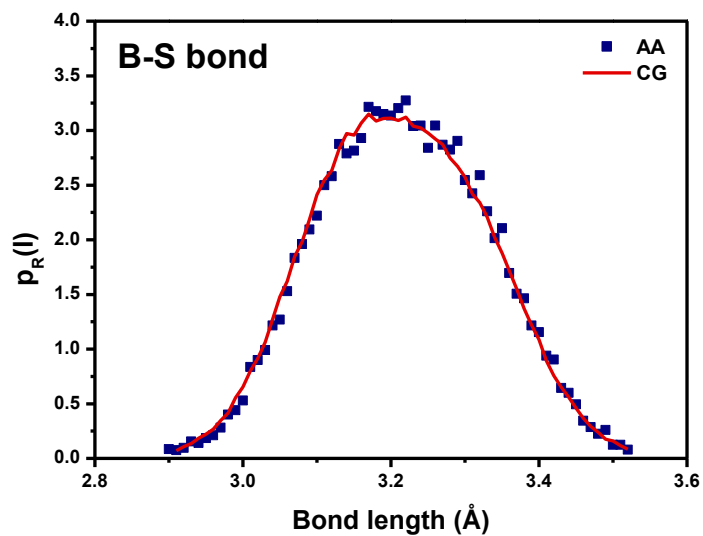
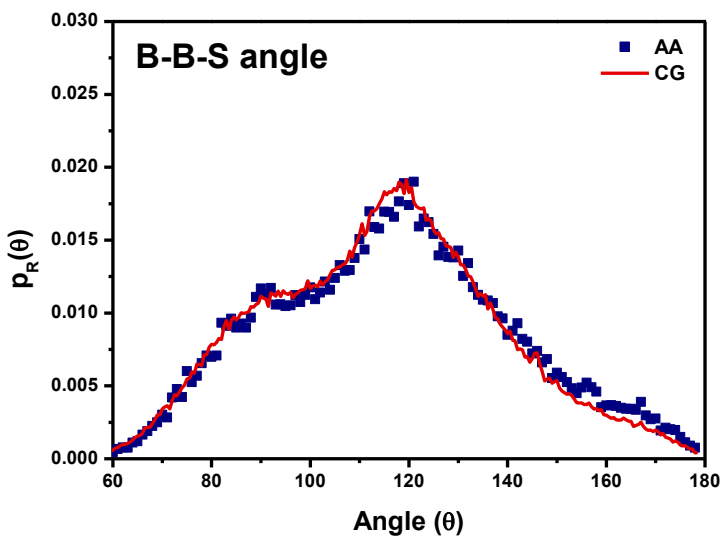


Figure 2.10. Derived coarse-grained pair potential potential associated with vulcanizing agent: (a) S-S pair and (b) B-S pair.

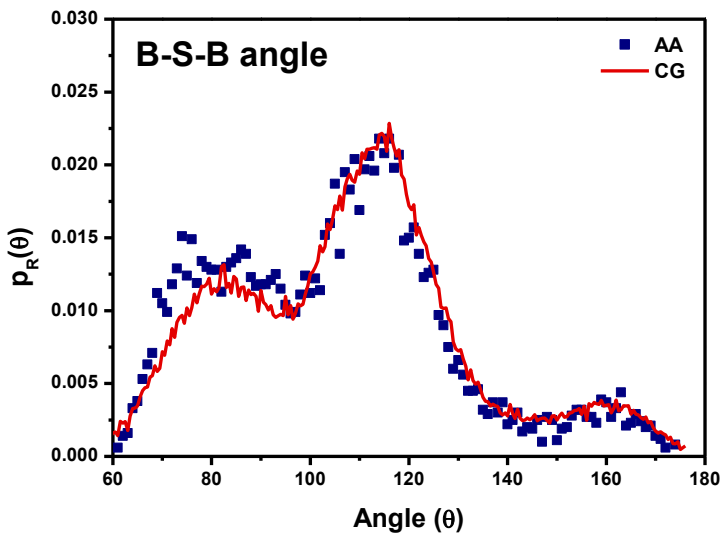
(a)



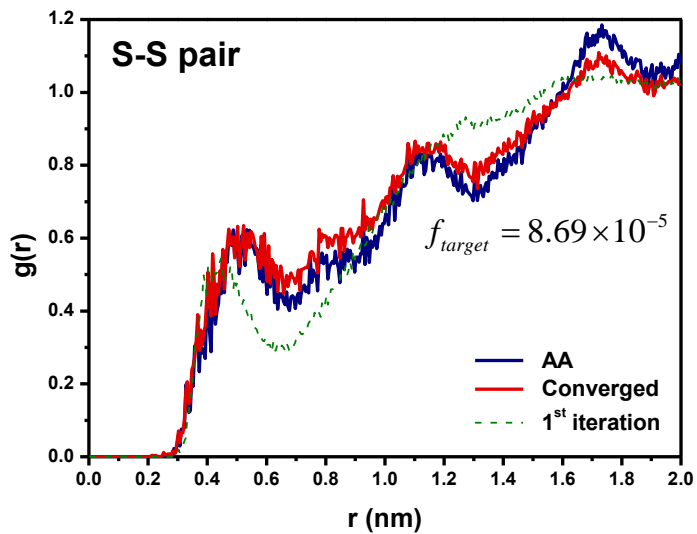
(b)



(c)



(d)



(e)

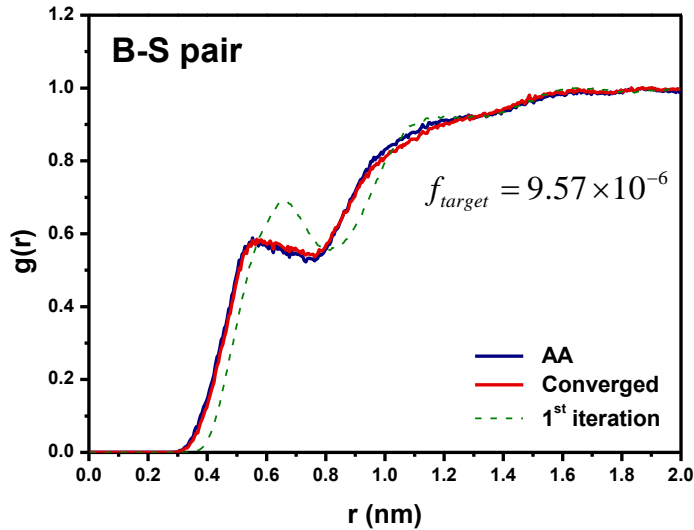


Figure 2.11. Comparison of structural conformation between the derived coarse-grained model and the representative all-atom model for vulcanized natural rubber system: (a) bond length distribution of B-S, (b) bending angle distribution of B-B-S, (c) bending angle distribution of B-S-B, (d) radial density distribution of S-S pair, and (e) radial density distribution of B-S pair.

2.4. Introduction of nanoparticle into rubber

Nano-sized Carbon black and silica fillers have been extensively used to improve the functionality and performance of rubber in various industrial fields. In order to derive CG potential regarding a nanocomposite system with NR and silica fillers, the representative atomic model for NR/silica was prepared. A spherical shape of silica nanoparticle with the radius of 1 nm was embedded into the NR matrix as illustrated in **Figure 2.12**. The atomic model of nanocomposite was equilibrated at 300 K and 1 atm condition with the same manner as applied in Section 2.3.1 for NR system. Then, 2,000 frames of representative trajectories for the NR/silica nanocomposite system were stored for every 500 fs during 1 ns of NVT ensemble at 300 K.

For establishing the CG bead model for the silica particle, the positions of silicon atoms were replaced by F beads that have the equivalent mass of SiO_2 . The atomic connectivities between Si-O-Si atoms were then replicated F-F bead connectors. The detailed mapping scheme for the silica nanofiller and NR/silica nanocomposite system are illustrated in **Figure 2.13**.

From the representative trajectories of NR/silica system, the probability density distribution of F-F bond length and F-F-F bending angle were computed. Following the same procedure described Section 2.3.1., the bonded CG potentials (F-F bond and F-F-F angle) were derived (**Figure 2.14**).

Non-bond interactions associated with the F bead in the NR/silica

nanocomposite system are F-F and F-B pair. Herein, the F-F non-bond interaction is directly related with the inter-particle interaction that determines the degree of dispersion of nanoparticles within the rubber matrix medium. In order to define the F-F pair interaction, a simple molecular system containing 2,000 molecules of SiO_2 was prepared in a 3-D periodic box (**Figure 2.15**). The simple atomic system of SiO_2 was equilibrated at 300 K and 1 atm condition with 2 ns of NVT ensemble and 5 ns of NPT ensemble. From the equilibrated system, 2,000 frames of trajectories were stored for 2 ns of NVT ensemble simulation at 300 K. Then, the RDF of centroid of SiO_2 molecules was computed and the pair potential of F-F was derived using Boltzmann inversion (Eq. 2.12). In **Figure 2.16**, the derived F-F pair potential and the resulting RDF of F-F in a CG model with using the F-F pair potential was compared with the RDF of SiO_2 atomic system.

In the nanocomposite system, the interfacial interaction between the filler and matrix phase is of a critical importance to determine the interphase region. In the NR/silica nanocomposite system, the pair interaction between F and B bead plays a significant role in describing the interfacial communication. To define the non-bond interaction of F-B pair, the IBI method was applied with the representative model for the nanocomposite system (see **Figure 2.12**). The obtained CG potential for the F-B pair interaction is shown in **Figure 2.17**.

With the final set of CG potentials associated with the NR/silica nanocomposite system, the structural conformations of CG model were compared with those of the

representative atomic model, showing a reasonable agreement with their counterparts (detailed procedure is described in Section 2.3.1.). In terms of density from the equilibrated system, the present CG potential set for the nanocomposite provides a reliable value as compared to the reference density computed from the atomic system: 0.8526 g/cm³ of the CG model and 0.8433 g/cm³ of the representative atomic model.

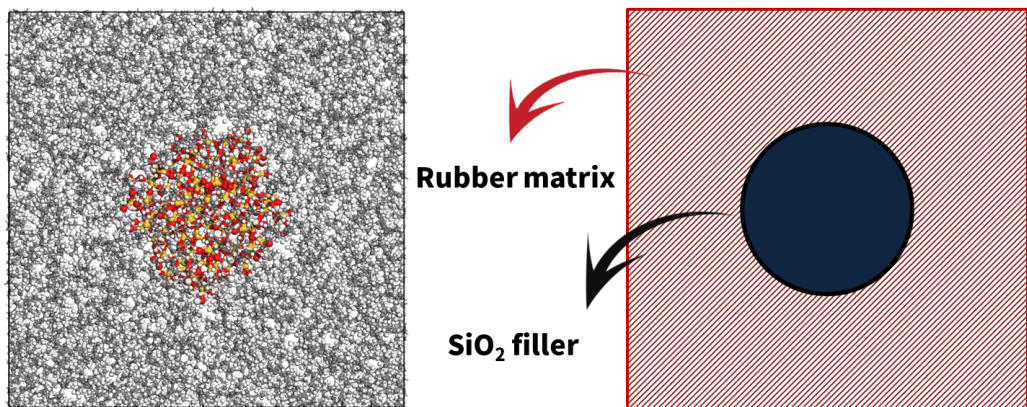
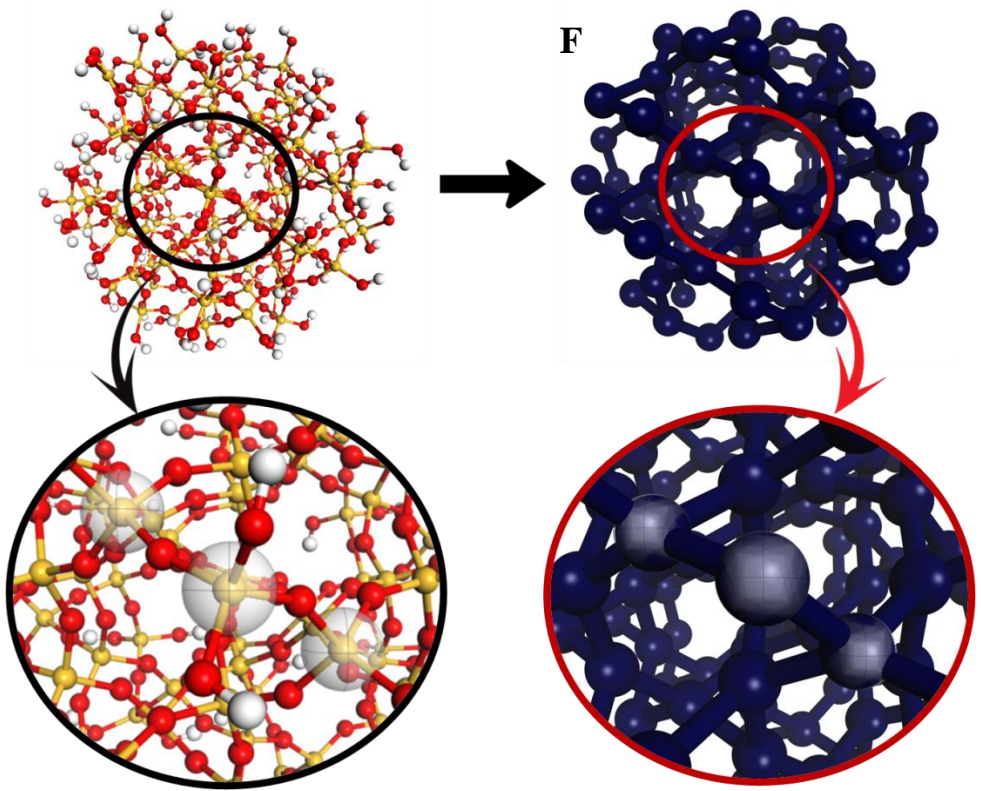


Figure 2.12. Atomic unit cell configuration of silica-filled rubber nanocomposite.

(a)



(b)

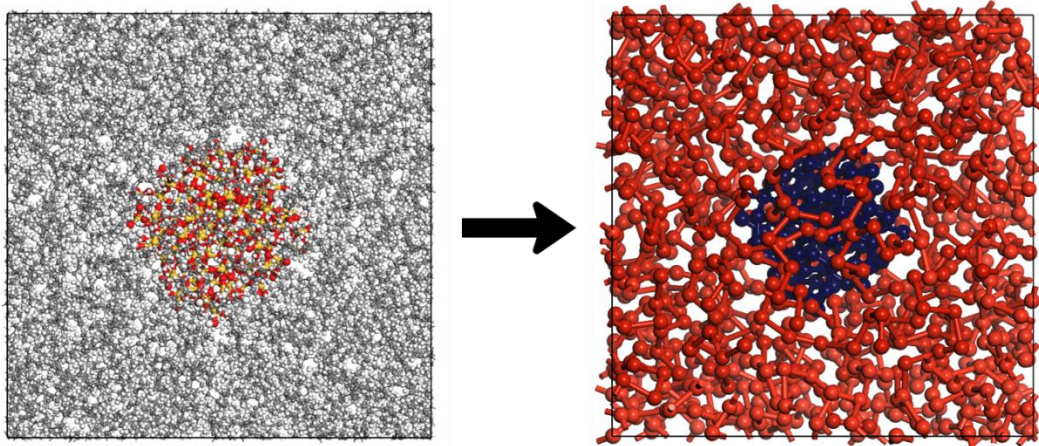
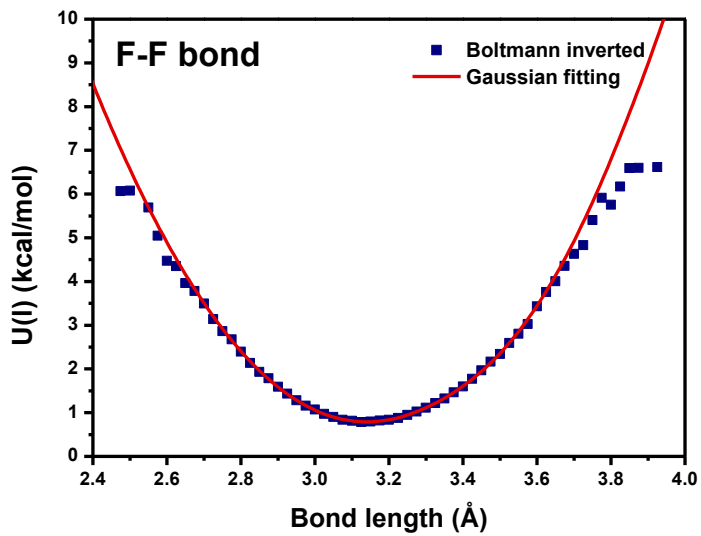


Figure 2.13. Coarse-grained mapping scheme for silica-filled rubber nanocomposite:

(a) coarse-grained bead connector representation of silica nanoparticle, and (b)

coarse-grained natural rubber/silica nanocomposite system.

(a)



(b)

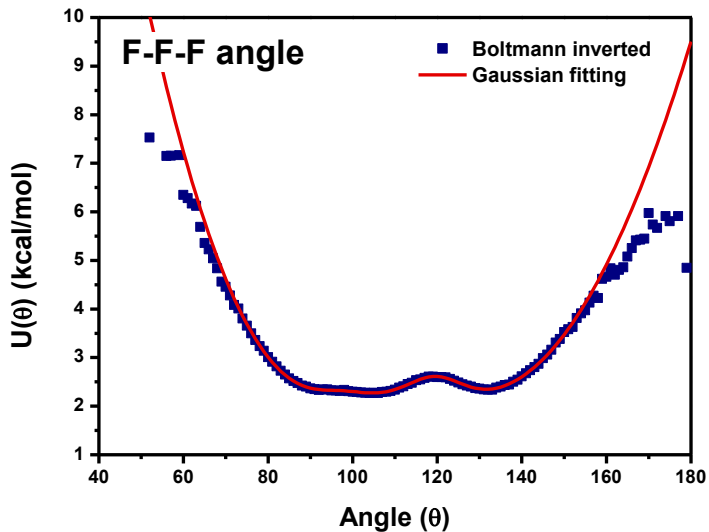


Figure 2.14. Derived coarse grained bonded potential associated with silica nanoparticle: (a) FF bond and (b) FFF angle.

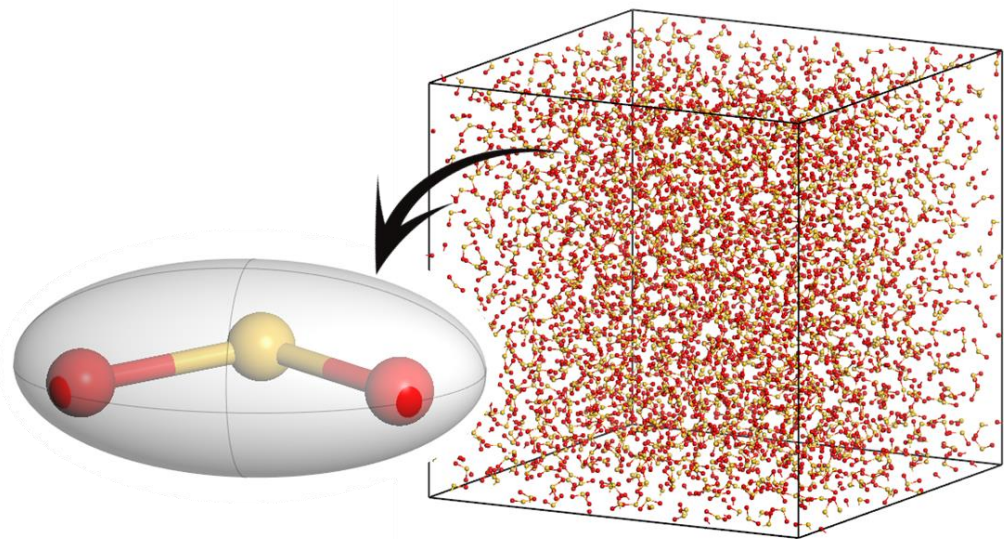
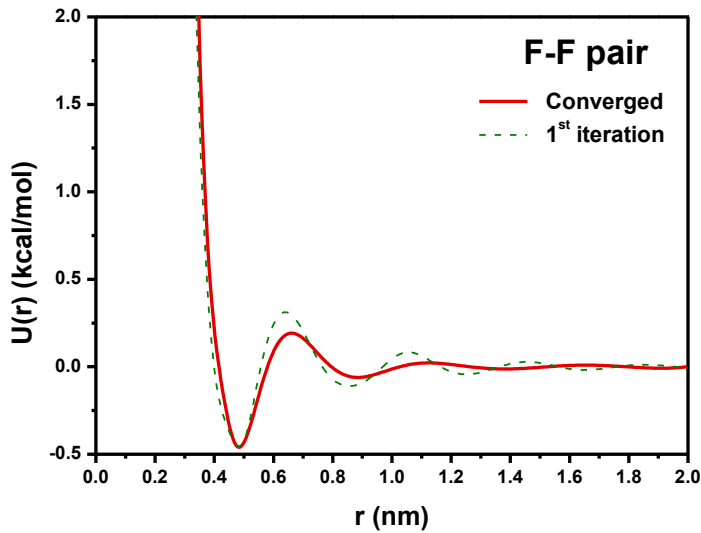


Figure 2.15. Simple atomic model to derive F-F pair interaction: 2,000 number of SiO_2 molecules.

(a)



(b)

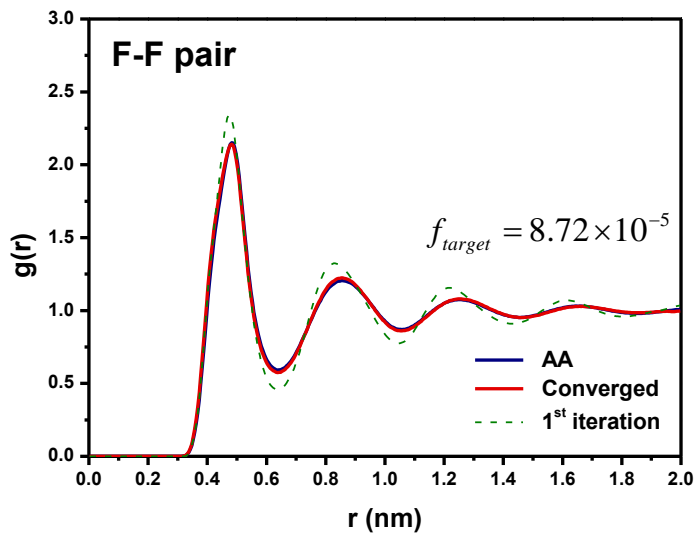


Figure 2.16. Derived coarse-grained pair potential: (a) F-F pair potential and (b) radial density comparison between all-atom (AA) and coarse-grained (CG) model.

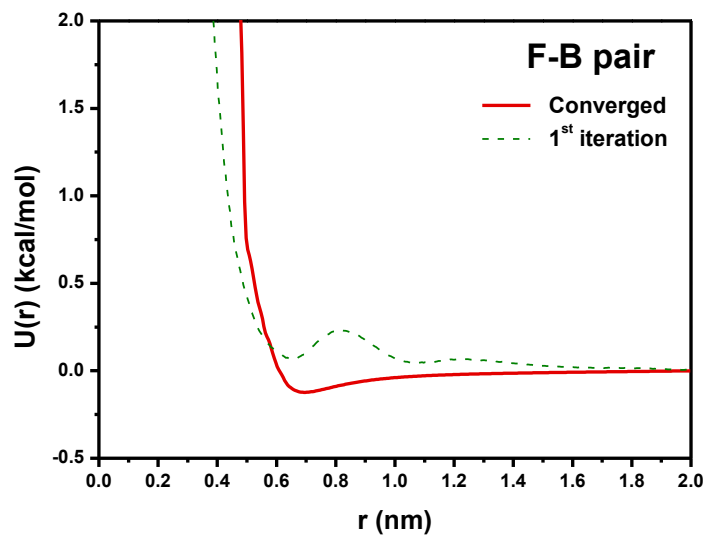
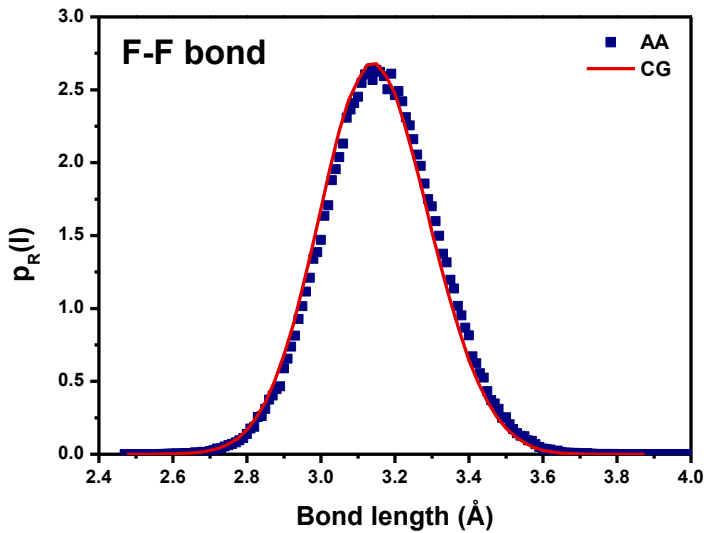
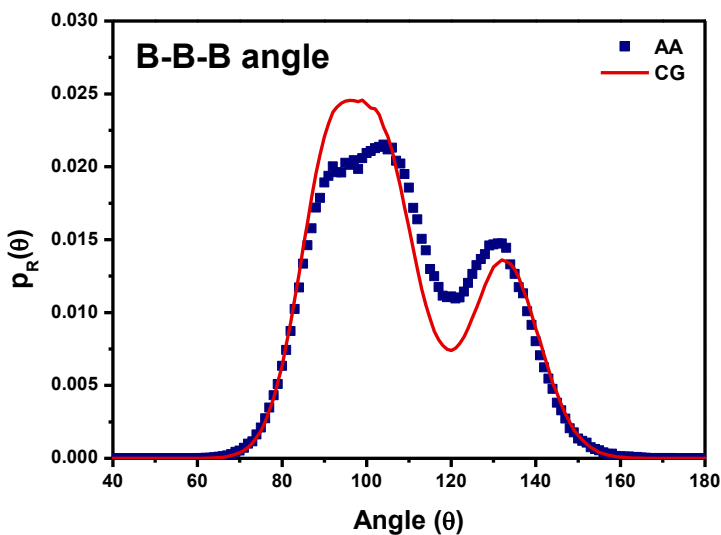


Figure 2.17. Derived coarse-grained pair potential between F and B bead.

(a)



(b)



(c)

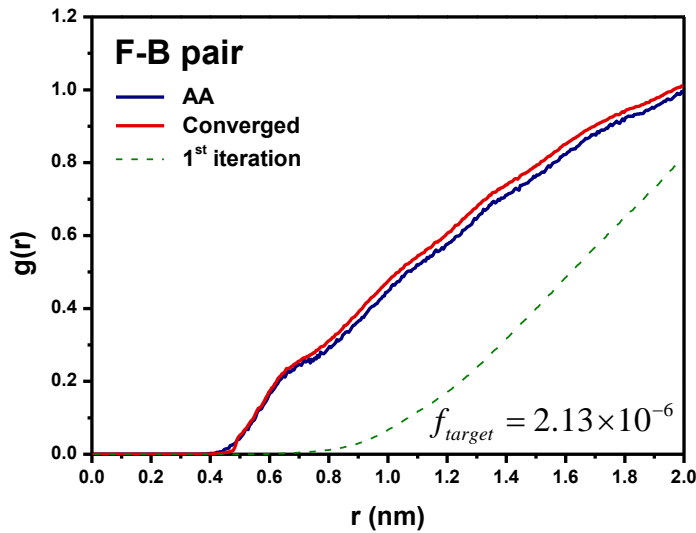


Figure 2.18. Comparison of structural conformation between the derived coarse-grained model and the representative all-atom model for nanocomposite system: (a) bond length distribution of F-F, (b) bending angle distribution of F-F-F, and (c) radial density distribution of F-B pair.

3. Viscoelastic Behavior of Natural Rubber

3.1. Coarse-grained molecular dynamics simulation setup

The viscoelastic nature of polymer is strongly attributed to the macromolecular size^{44-45, 69-71}. The characteristic relaxation time is substantially affected by the internal motions. In that regards, various NR systems were considered in terms of NR chain length, vulcanization, and filled-NR system.

● Unvulcanized natural rubber

In order to understand the effect of polymer chain length on the viscoelastic behavior of natural rubber, the unvulcanized systems with varying molecular weight were considered. The initial random chain configurations for unvulcanized NR were established using Mesostructure Builder in Materials Studio. Herein, unvulcanized NR systems with a wide range of NR chain length were modeled; NR1, NR2, NR3, and NR4 having 10, 100, 1000, and 7000 beads per chain, respectively.

● Vulcanized natural rubber

To investigate chain network effect due to rubber vulcanization, NR and sulfur mixture was modeled. For NR chains, 25 number of NR chains consisting of 1000 beads were used. To capture the influence of different vulcanization ratio, VR1 and VR2 were

considered containing 1 phr and 2 phr of sulfur, respectively. The initial mixture VR1 and VR2 were equilibrated at 300 K and 1 atm condition. The crosslinking between NR chains and sulfur was conducted using “fix bond/create” command in LAMMPS.

- **Silica-filled natural rubber**

For silica-filled NR system, spherical shape of silica nanoparticle with the radius of 1 nm was used as a reinforcing filler material. In this work, FR1 and FR2 were modeled considering filler volume fraction of 5% and 10%, respectively. A number of particles associated designed volume fraction were embedded into unvulcanized NR matrix.

Detailed system compositions for unvulcanized NR, vulcanized NR, and silica-filled NR are described in **Table 3.1**.

Table 3.1. Detailed composition of coarse-grained (CG) natural rubber system and equilibrium density at 300 K and 1 atm.

System type	No. of monomers per chain	No. of beads	No. of crosslinks	No. of particles	Cell length (Å)	Equilibrium density (g/cm³)
NR1	10	35,360	-	-	172.01	0.7861
NR2	100	35,400	-	-	167.89	0.8464
NR3	1000	35,000	-	-	166.84	0.8527
NR4	7000	35,000	-	-	165.46	0.8538
VR1	1000	25,534	534	-	147.37	0.8749
VR2	1000	26,057	1,057	-	147.61	0.8971
FR1	1000	33,904	-	17	161.67	0.8849
FR2	1000	33,808	-	34	159.42	0.9187

3.2. Characterization of viscoelastic properties

The established NR systems as described in the previous section were equilibrated at desired temperature and pressure condition (1 atm). In order to capture the variation of properties with temperature, a range of temperature from 263 K to 400 K was considered. The systems were equilibrated at an elevated temperature of 500 K with the NVT ensemble of 25 ns, and then further relaxed at the target temperature and pressure condition with using the NVT ensemble of 25 ns and the NPT ensemble of 50 ns. During the ensemble simulations for the equilibrium process, the temperature and pressure were controlled with the Langevin thermostat and the Berendsen barostat, respectively, and the time step of 5 fs was employed.

From the equilibrated CG model, the stress relaxation function, $G(t)$, was computed with the implementation of the stress autocorrelation function (SACF)⁴²;

$$G(t) = \frac{V}{k_B T} \langle \sigma_{\alpha\beta}(t) \sigma_{\alpha\beta}(0) \rangle \quad (3.1)$$

where $\sigma_{\alpha\beta}$ is the instantaneous shear stress ($\alpha \neq \beta$), and $\langle \cdot \rangle$ denotes ensemble average. The stress $\sigma_{\alpha\beta}$ was calculated using the virial theorem,

$$\sigma_{\alpha\beta} = \frac{1}{V} \left[\sum_{i=1}^n m_i v_{i\alpha} v_{i\beta} + \sum_{i=1}^{n-1} \sum_{j=1}^n r_{ij\alpha} F_{ij\beta} \right] \quad (3.2)$$

where m_i , $v_{i\alpha}$, and $v_{i\beta}$ are the mass and α - and β -component velocities of i -th bead, respectively, and $r_{ij\alpha}$ and $F_{ij\beta}$ are the α -component of separation distance and β -component of force between i -th and j -th beads. For the production run to calculate

$G(t)$, a small perturbation was imposed on the system and the microcanonical (NVE) ensemble simulation was employed for 1 μ s with time step of 10 fs. Since the system is isotropic, the three off-diagonal stress tensor, σ_{xy} , σ_{yz} , and σ_{xz} , are averaged out to obtain the SACF for a single production run. To obtain smoother estimates of the SACF for $G(t)$, three independent production runs were carried out for each system.

The storage modulus, $G'(\omega)$, and the loss modulus, $G''(\omega)$, can be computed from the frequency-dependent complex shear modulus, $G^*(\omega)$, that is calculated as the Fourier transform of $G(t)$:

$$G^*(\omega) = i\omega \int_0^\infty e^{-i\omega t} G(t) dt \quad (3.3)$$

where $G'(\omega)$ and $G''(\omega)$ are the real and complex components of $G^*(\omega)$, respectively:

$$G'(\omega) = \omega \int_0^\infty G(t) \sin(\omega t) dt \quad (3.4)$$

$$G''(\omega) = \omega \int_0^\infty G(t) \cos(\omega t) dt \quad (3.5)$$

3.3. Dynamic scaling between coarse-grained system and all-atomistic system

In the CG mapping scheme, a group of atoms is lumped together into a bead. Since the internal degree of freedom in the CG bead system has been reduced, the

entropy and the free-energy landscape can be changed^{27, 42}. Thus, the internal dynamics of the system are substantially altered after coarse-graining. In general, the CG system inherently exhibits a faster dynamics due to the smoothed energy landscape and the reduced frictional force between the associated CG beads. It is therefore necessary to rescale the dynamics of CG system.

The rescaling method adopted in the present work is to use the mean-squared displacement (MSD) of the system as the time-scaling metric, since the MSD is inversely proportional to the friction coefficient for unentangled polymer chains. The time-dependent scaling function, $f_t(t)$, is defined as the ratio of the MSD in CG system (MSD_{CG}) and the MSD in its atomistic counterpart (MSD_{AA}):

$$f_t(t) = \frac{MSD_{CG}}{MSD_{AA}} \quad (3.6)$$

At very short time scales, the value of the dynamic rescaling function is unity, and at longer time scales, the rescaling function increases monotonically and saturates at a certain level. Herein, the dynamic scaling functions for the NR1 system were computed at each temperature considered in this work. Then, the obtained dynamic scaling functions were fitted to an exponential series:

$$f_t(t) = 1 + \sum_i a_i (1 - e^{-t/\tau_i}) \quad (3.7)$$

where the characteristic simulation times, τ_i , reflect time scales over which the simulated dynamics are accelerated by the corresponding time factor, a_i . The computed dynamic scaling factors with the fitting results are illustrated in **Figure 3.1**. Using the

dynamic scaling function, the stress relaxation spectrum of the CG model, $G_{CG}(t)$, is rescaled with the rescaled time, t_{scaled} , as follows:

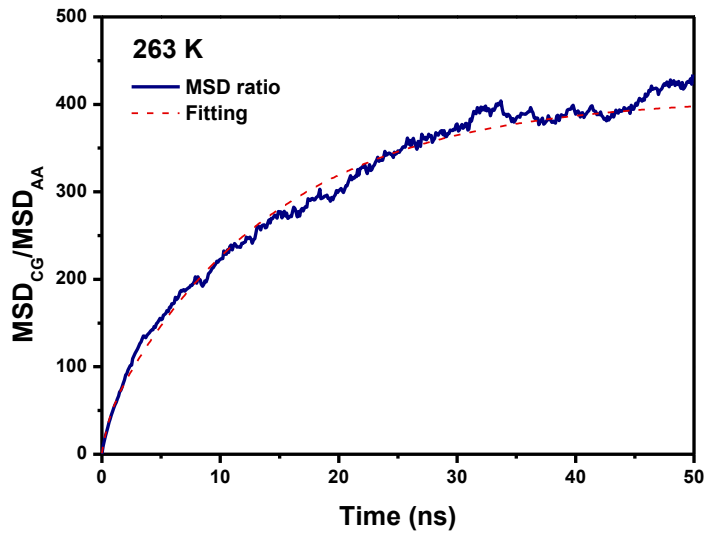
$$\begin{aligned} t_{scaled} &= f_t(t) \\ G(t) &= G_{CG}(t_{scaled}) \end{aligned} \quad (3.8)$$

To verify the present scaling scheme in terms of its viscoelastic properties, the normalized relaxation spectra computed from atomistic and CG simulations are compared in **Figure 3.2**. As can be seen in **Figure 3.2**, the dynamic scaling factors reasonably rescale the CG systems for the considered temperature range as compared to their atomistic counterparts.

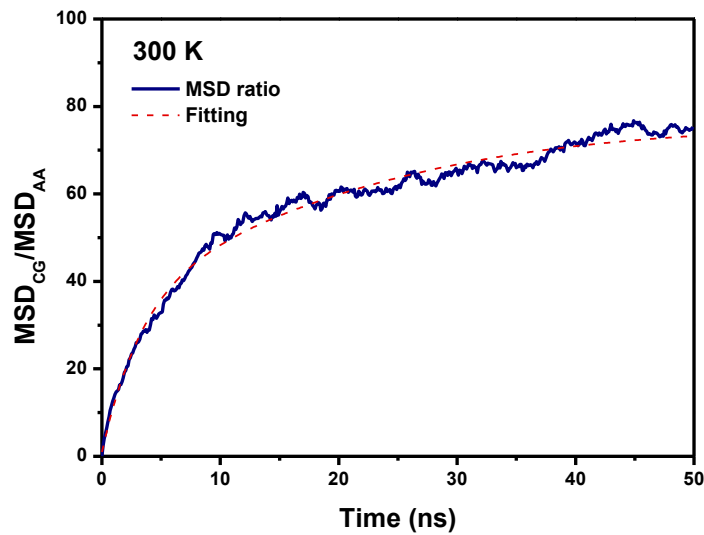
As far as the characterization of thermomechanical properties with CG MD is concerned, the discrepancy is prevalently observed; especially structure-based bottom up CG methods do not demonstrate thermomechanical consistency with their atomistic counterparts. In that sense, the determination of thermodynamic scaling relationships is necessary to make quantitative predictions from CG systems. Herein, a comprehensive scaling parameter for $G(t)$ was computed empirically by the ratio of $G(0)$ from all-atomistic simulation and CG simulation. We assumed that this scaling parameter for $G(t)$ is time-independent and independent of the length and the temperature. The computed scaling parameters for the unvulcanized NR systems are listed in **Table 3.2**. In order to quantify the relaxation spectrum $G(t)$ for the CG system, the time and the modulus axes need to be rescaled by the scaling factor $f_t(t)$ and f_G . However, this is quite challenging for such long NR chains, especially obtaining $f_t(t)$, which requires

enormous time of computation with both all-atomistic and CG MD simulations. Therefore, in this work, the scaling factor $f_t(t)$ for a given temperature is assumed to be identical for other CG systems having different chain length, vulcanized networks, and silica reinforcing nanoparticles. Plus, based on the observation of f_G for varying temperature and chain length, the averaged scaling parameter of 58.90 was used to quantify the relaxation spectrum of $G(t)$ from the CG MD simulations. Although such a dynamic rescaling method does not have rigorous theoretical foundations, it has been used successfully for low degrees of coarse graining.

(a)



(b)



(c)

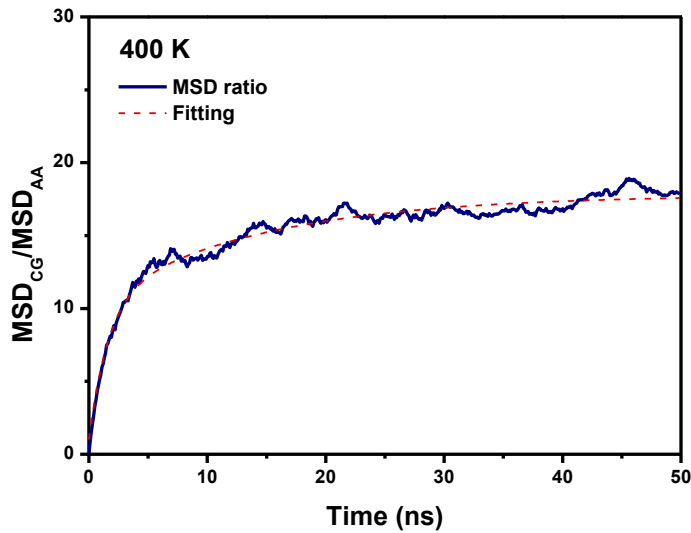
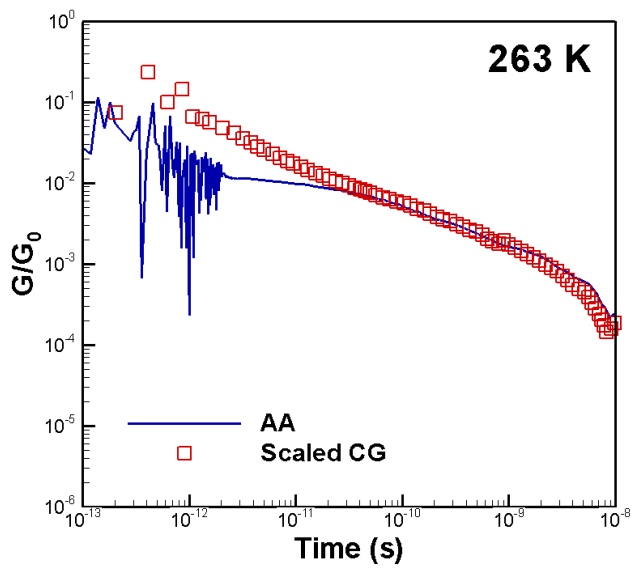


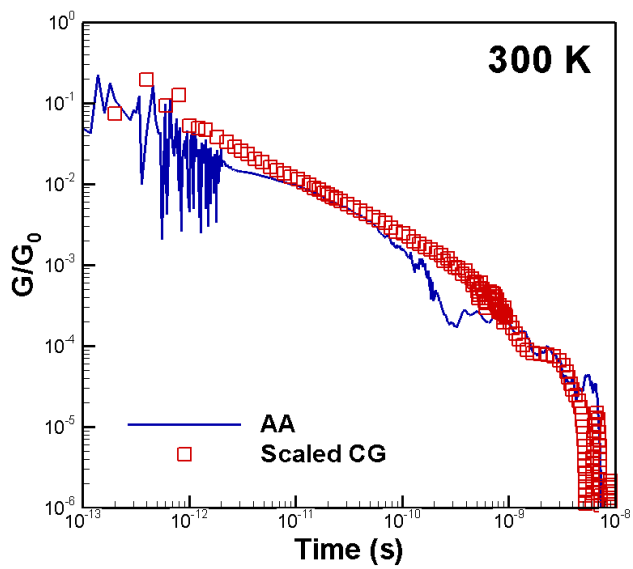
Figure 3.1. Dynamic scaling factor of NR1 system for temperature of (a) 263 K, (b) 300 K, and (c) 400 K; the dashed line shows the fitted curve by the equation

$$f_t(t) = 1 + \sum_i a_i (1 - e^{-t/\tau_i}).$$

(a)



(b)



(c)

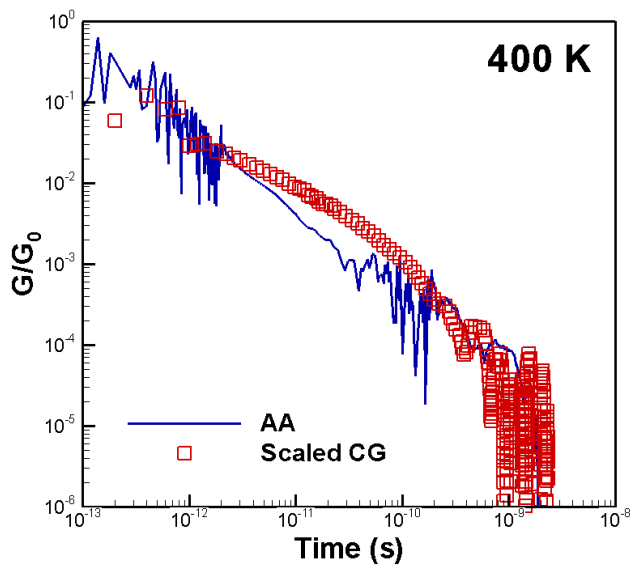


Figure 3.2. Normalized time-dependent relaxation modulus for (a) 263 K, (b) 300 K, and (c) 400 K from all-atomistic (AA) simulation and from coarse-grained (CG) simulation after applying dynamic time scaling.

Table 3.2. Comparison of instantaneous shear modulus from all-atomistic MD and CG MD simulation with the scaling parameter for relaxation modulus (f_G).

Temperature (K)	System type	$G_{AA}(0)$ (GPa)	$G_{CG}(0)$ (GPa)	$f_G = \frac{G_{AA}(0)}{G_{CG}(0)}$
263	NR1	42.16	0.71	59.38
	NR4	-	0.81	-
300	NR1	40.69	0.68	60.18
	NR2	43.41	0.77	56.33
	NR3	43.92	0.78	56.29
	NR4	-	0.78	-
400	NR1	37.61	0.60	62.34
	NR4	-	0.73	-

3.4. Viscoelastic property of natural rubber system

The relaxation spectra of $G(t)$ were computed from the SACFs with the implementation of effective scaling scheme for both time and shear modulus axes in terms of the following parameters: chain length of NR, systematic vulcanization, reinforcing filler inclusion.

- **Effect of chain length**

From the unvulcanized NR system with varying chain length, the time-dependent relaxation modulus, $G(t)$, was computed. To provide a clear comparison with the parameters and to perform the Fourier transformation for achieving dynamic modulus, the data of relaxation modulus were fitted by the generalized Maxwell model, which is a sum of exponentially decaying terms:

$$G(t) = \sum_n G_n \exp\left(-\frac{t}{\tau_n}\right) \quad (3.9)$$

where G_n and τ_n are the amplitude and relaxation time of the n -th mode, respectively. In **Figure 3.3**, the obtained relaxation modulus data for NR1 and NR4 with the fitted curve are illustrated. For other unvulcanized NR systems, the same fitting process was applied and the results of relaxation spectra are given in **Figure 3.4**. From the results, it can be easily gleaned that the relaxation times of the unvulcanized NR systems rise with increasing NR chain length. In the shorted chain length system of NR1, the rapid

decaying in modulus with time is observed. As the chain length increases, the decaying rate declines so that the hint of rubbery plateau can be captured.

With the implementation of the Fourier transformation, the relaxation spectrum can be transformed into the frequency domain demonstrating the dynamic modulus, storage and loss modulus as shown in Eqs (3.4) and (3.5). The computed relaxation spectra were transformed into the frequency domain using the Fourier transformation as shown in **Figure 3.5**. From the results of NR1, a liquid-like terminal behavior at low frequency can be observed; $G'(\omega) \approx \omega^2$ and $G''(\omega) \approx \omega^1$. As the molecular weight increases, the NR systems show departure from the above scaling with $G'(\omega) \approx \omega^\nu$ and $G''(\omega) \approx \omega^\mu$, where $\nu < 2$ and $\mu < 1$. This nonterminal behavior indicates that the NR with longer chain behave as an intermediate to a Newtonian fluid ($G''(\omega) \approx \omega^1$) and a solid ($G''(\omega) \approx \omega^0$). Moreover, the NR systems exhibit larger storage and loss modulus along the entire frequency range, yielding better capability to store and dissipate deformation energy across the frequency range considered in this work. This tendency becomes more prominent as the frequency range decreases. Plus, at low frequencies, a crossover occur, that is, $G'(\omega) < G''(\omega)$, the materials behave more dissipative than elastic. At this regime, the storage and loss modulus show a plateau, respectively, which are typically indicative of entanglement effects.

● Effect of vulcanization

The viscoelastic characteristics of vulcanized NR systems were calculated

regarding two different sulfur contents, 1 phr and 2 phr. The addition of sulfur in NR chains forms crosslinked networks between chains. This significant variation on the microstructure in NR system alters not only the time-dependent modulus but also the relaxation nature. As can be observed in **Figure 3.6**, with the formation of crosslinked networks the reinforcement on the shear modulus can be observed. As far as the decaying rate of $G(t)$ is concerned, a significant change on the relaxation behavior with the vulcanization can be captured. In the VR2 system that contains larger amount crosslinked junction with the sulfur and NR, the plateau of $G(t)$ can be clearly observed, and under the present time scale range the terminal behavior cannot be captured due to the lack of computation time.

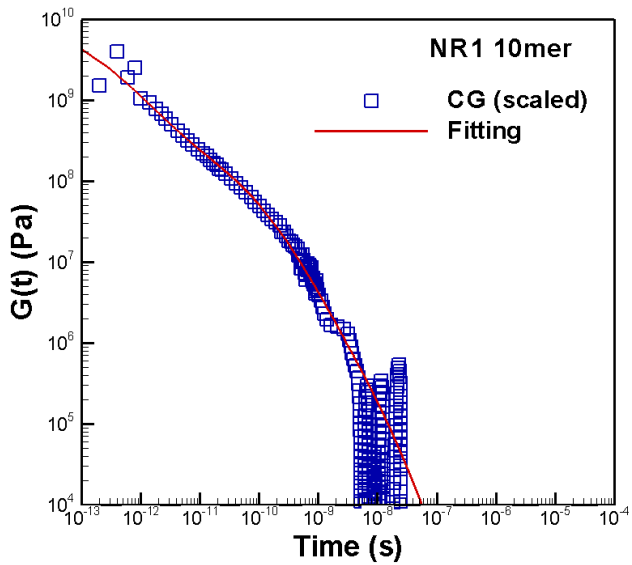
The dynamic modulus of the vulcanized NR systems was represented in **Figure 3.7**. At higher frequencies, the reinforcement in both storage and loss modulus can be captured, and with the formation of more vulcanized networks the degree of reinforcement is also enhanced. At the regime of intermediate frequencies, the crossover where the region shows $G'(\omega) < G''(\omega)$ is prominent, that is the dissipative regime. Moreover, the plateau of $G'(\omega)$ and $G''(\omega)$ is more prominent in the VR2 system, showing an agreement as compared to a general feature of frequency-dependent master curve of rubber compound.

● Effect of reinforcing filler

To investigate the effect of nanofiller on NR, the spherical shape of silica

nanoparticles were embedded into the unvulcanized NR model considering two different filler volume fractions (0.05 and 0.1), and the viscoelastic behavior was examined. For the relaxation spectrum, as can be seen in **Figure 3.8**, a monotonic reinforcement effect with increasing filler loading can be observed along the entire frequency range considered in this study. The general trend of relaxation modulus with time does not change much relatively other effects considered previously. As expected from this observation, the frequency-dependent dynamic modulus (see **Figure 3.9**) shows a similar feature, that is a monotonic enhancement in both storage and loss modulus. At low frequencies, a slight modification can be seen; the plateau region begins to develop compared to the unvulcanized NR system. Main reason behind this observation is that the silica nanoparticle has a relatively weak interfacial interaction with NR chains. Thus, the overall relaxation behavior of NR chains is likely to be unchanged due to this weak interfacial communication nature attributed to the silica nanoparticulates.

(a)



(b)

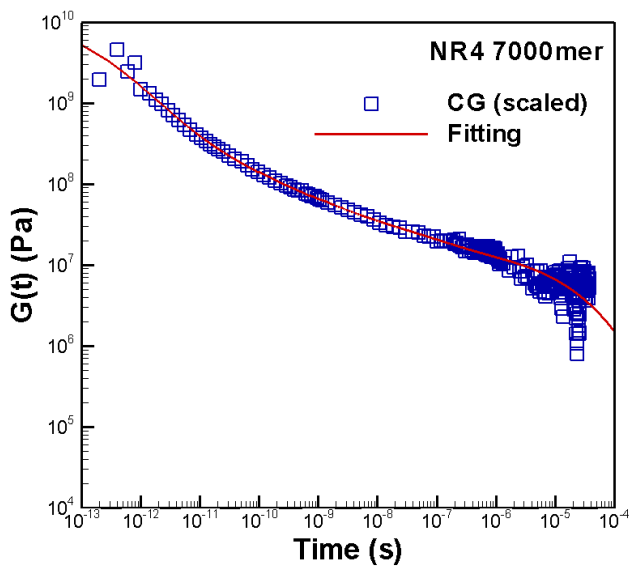


Figure 3.3. Time-dependent relaxation modulus of (a) NR1 (10mer) and (b) NR4 (7000mer) with the fitting curve by the generalized Maxwell model.

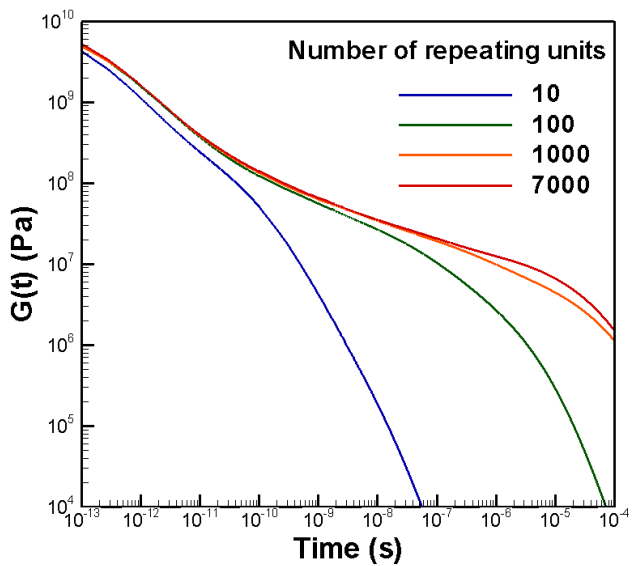
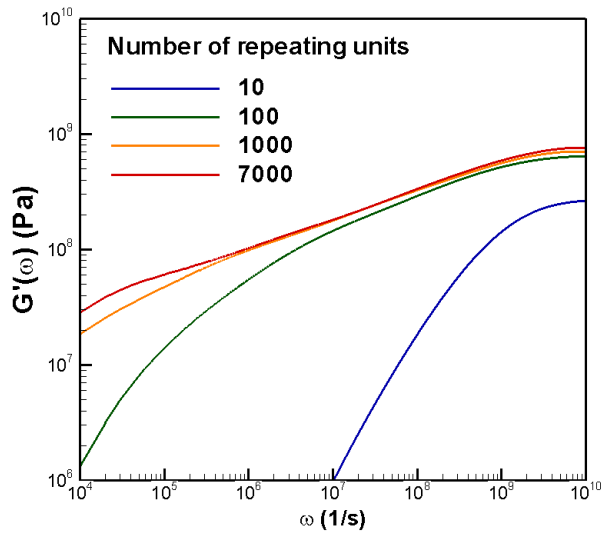


Figure 3.4. Relaxation spectrum $G(t)$ of unvulcanized natural rubber system for varying chain length.

(a)



(b)

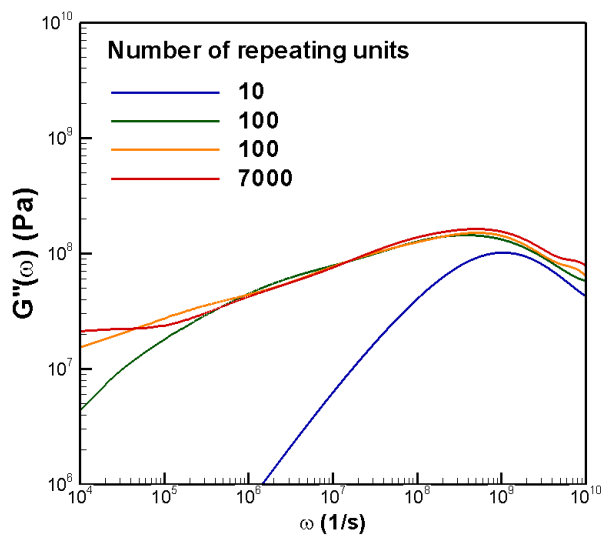


Figure 3.5. Frequency-dependent (a) storage modulus $G'(\omega)$ and (b) loss modulus $G''(\omega)$ with varying chain length; the dynamic modulus is computed with the Fourier transformation of relaxation spectrum $G(t)$.

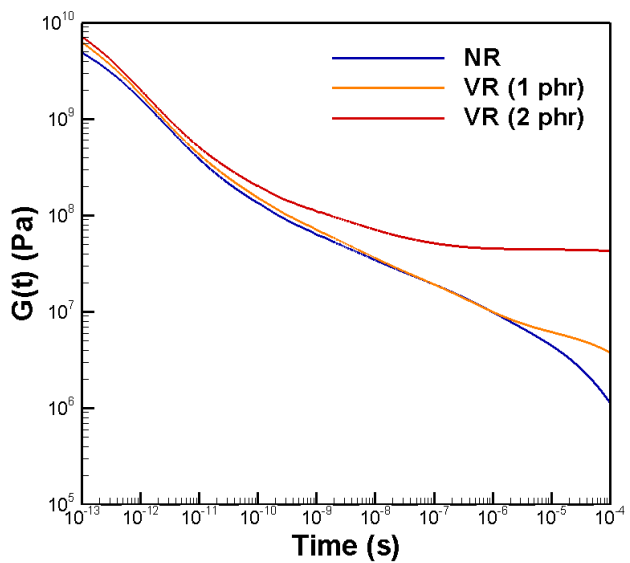
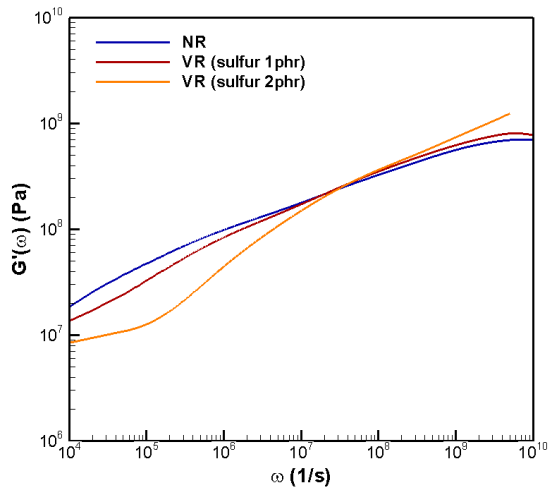


Figure 3.6. Comparison of relaxation spectrum $G(t)$ of vulcanized natural rubber system (VR1 and VR2) for different sulfur content with the unvulcanized natural rubber system (NR3).

(a)



(b)

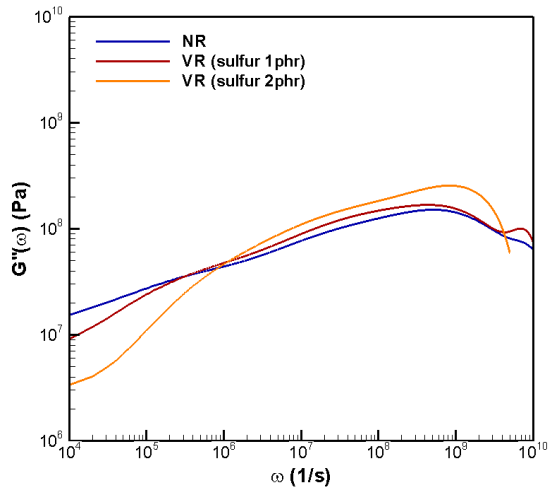


Figure 3.7. Frequency-dependent (a) storage modulus $G'(\omega)$ and (b) loss modulus $G''(\omega)$ for the vulcanized natural rubber system with varying sulfur content; the dynamic modulus is computed with the Fourier transformation of relaxation spectrum $G(t)$.

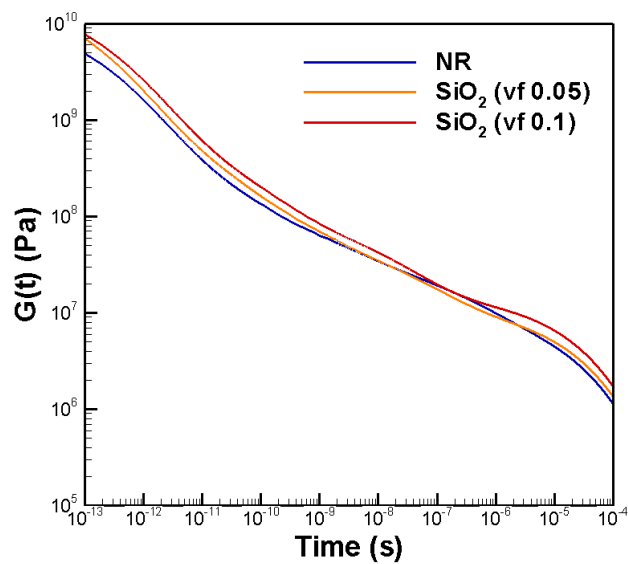
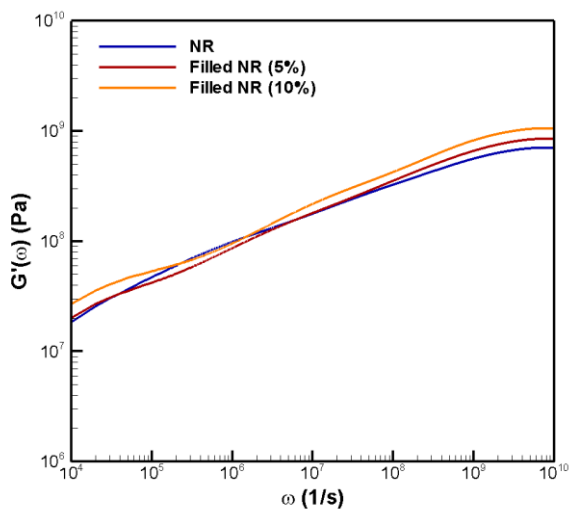


Figure 3.8. Comparison of relaxation spectrum $G(t)$ of silica-filled natural rubber system (FR1 and FR2) for different filler volume fraction with the unvulcanized natural rubber system (NR3).

(a)



(b)

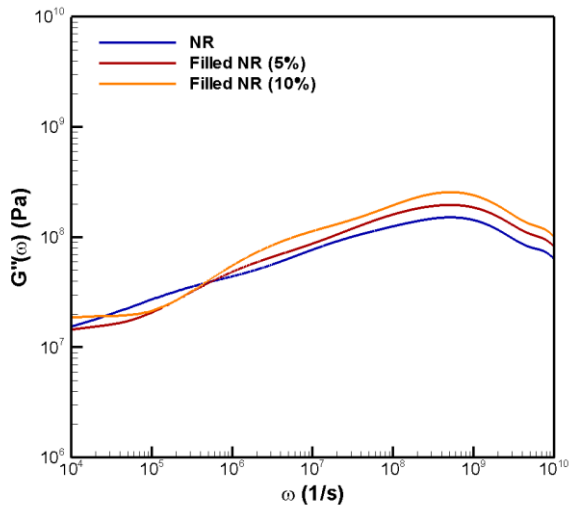


Figure 3.9. Frequency-dependent (a) storage modulus $G'(\omega)$ and (b) loss modulus $G''(\omega)$ for the vulcanized natural rubber system with varying sulfur content; the dynamic modulus is computed with the Fourier transformation of relaxation spectrum $G(t)$.

4. Hysteresis Friction Behavior of Natural Rubber

4.1. Characterization of surface roughness

Many studies of the fractal nature of surfaces (including road surfaces) have appeared in the literature. In many cases a self-affine behavior was observed. The term “self-affinity” was introduced when he studied geometrical objects that are statistically invariant under anisotropic dilations^{1,4}. It represents a generalization of the term “self-similarity” that denotes invariance under isotropic dilation. If the profile, $z(x)$, of a rough surface, i.e. of vertical cross-section of the surface, is considered, then the surface is self-affine if the transformation $x \rightarrow \lambda x$, $x \rightarrow \lambda^H x$ leaves the surface statistically invariant. The exponent, H ($0 < H < 1$) is called the roughness- or the Hurst-exponent. It is related to the local fractal dimension. D , of the surface:

$$D = d - H \quad (4.1)$$

where d is the dimension of the Euclidean imbedding space, e.g. $d = 3$ for surfaces in three-dimensional (3D) space or $d = 2$ for 2D cross-sections of the surface.

In addition to the surface fractal dimension D , two further length scales are necessary to characterize a self-affine surface: (i) the correlation length ξ_{\parallel} parallel to the surface, and (ii) the variance, i.e. the root mean square fluctuations around the mean height:

$$\varphi^2 = \langle (z(x) - \langle z \rangle)^2 \rangle \quad (4.2)$$

Here, $\langle z \rangle$ is the mean height of the surface points and $\langle \bullet \rangle$ is the average over the set of observations of surface topography. The variance φ can also be expressed by the correlation length ξ_{\perp} normal to the surface ($\varphi^2 = 2\xi_{\perp}^2$).

For an estimation of the correlation lengths ξ_{\perp} , ξ_{\parallel} and the surface fractal dimension D , the height-difference correlation function is considered as follows:

$$C_z(\lambda) = \langle (z(x+\lambda) - z(x))^2 \rangle \quad (4.3)$$

It describes the mean square height-fluctuations of the surface with respect to the horizontal length scale λ . For self-affine surfaces $C_z(\lambda)$ follows a power law with exponent $2H$ on small length scales for $\lambda < \xi_{\parallel}$ and approaches the constant value ξ_{\parallel}^2 for $\lambda > \xi_{\parallel}$,

$$C_z(\lambda) = \left(\frac{\lambda}{\xi_{\parallel}} \right)^{2H} \xi_{\perp}^2 \quad (4.4)$$

The values of ξ_{\parallel} and ξ_{\perp} can be obtained from the cross-over point of $C_z(\lambda)$. This is shown schematically in **Figure 4.1**.

An alternative approach to the fractal analysis of rough surfaces considers the height-correlation function $\Gamma_z(\lambda)$ that is also termed an auto-correlation function:

$$\Gamma_z(\lambda) = \langle z(x+\lambda) \cdot z(x) \rangle - \langle z(x)^2 \rangle \quad (4.5)$$

It characterizes the correlation of heights at two different positions and goes to zero at

large distances for $\lambda > \xi_{\parallel}$, where the two heights become uncorrelated. The two correlation functions given in Eqs a and b, are related by the equation

$$C_z(\lambda) = 2(\varphi^2 - \Gamma_z(\lambda)) \quad (4.6)$$

For stationary surfaces the Fourier-transform of $\Gamma_z(\lambda)$ equals the spectral power density $S(f)$, where f is the spatial frequency:

$$\Gamma_z(\lambda) = \int_{f_{\min}}^{\infty} S(f) e^{2\pi i f \lambda} df \quad (4.7)$$

The minimum frequency f_{\min} corresponds to the inverse correlation length ξ_{\parallel} and represents the maximum wave length of the modulations of the surface ($f_{\min} = 1/\xi_{\parallel}$).

Statistically isotropic, self-affine surfaces, which have no scale and whose height is well defined but non-differentiable, have spectra of the fractal form,

$$S(f) = K f^{-\beta} = K f^{-(2H+1)} \quad (4.8)$$

The prefactor K is a scaling factor that can be expressed by the characteristic parameters of the surface ($K = H \xi_{\perp}^2 \xi_{\parallel}^{(1-\beta)}$). Eq. (4.8) can be rewritten in the following form:

$$S(f) = k \left(\frac{f}{f_{\min}} \right)^{-\beta} \quad (4.9)$$

The prefactor $k = K f_{\min}^{-\beta}$, that is termed “topothesy”, is related to the geometrical surface parameters as follows:

$$k = H \xi_{\perp}^2 \xi_{\parallel} \quad (4.10)$$

An estimation of the spectral power density from the auto-correlation function enables a complete characterization of self-affine surfaces via the exponent $\beta = 2H + 1 = 7 - 2D$,

the scaling factor k and the spatial cut-off frequency $f_{\min} = 1/\xi_{\parallel}$, because there is a direct correspondence between the parameter sets $(D, \xi_{\perp}, \xi_{\parallel})$ and (β, k, f_{\min}) . The behavior of the spectral power density is shown schematically in **Figure 4.2**.

The profile $z(x)$ of a non-reentrant, self-affine surface can be obtained by stylus measurements or by optical techniques. For a sufficient set of measurement points, to ensure stationarity, the spectral power density can be evaluated via Eqs. (4.5) and (4.7), where the parameters β , k , and f_{\min} are found as fitting parameters.

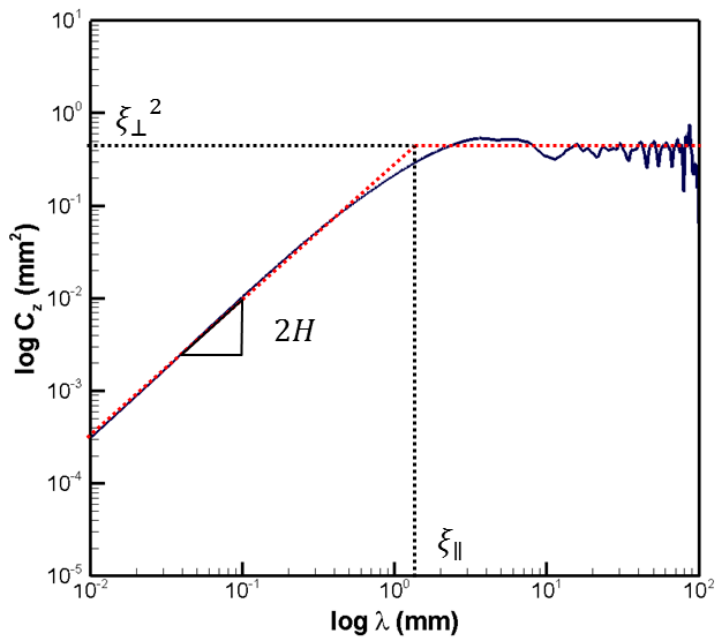


Figure 4.1. Height-difference correlation function of a self-affine surface. The values of ξ_{\perp} , ξ_{\parallel} can be obtained from the cross-over point. H is the Hurst exponent.

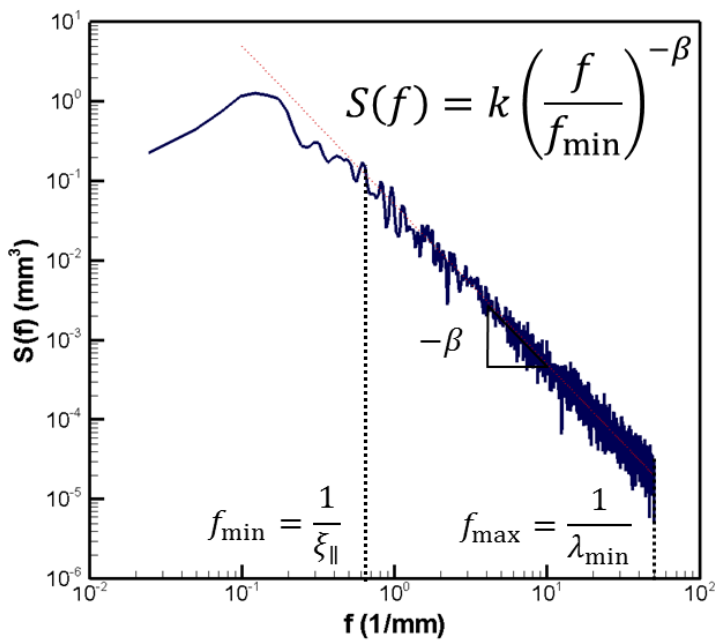


Figure 4.2. Visualization of the spectral power density as function of the spatial frequency. The exponent β is related to the surface fractal dimension D and to the Hurst exponent ($\beta = 2H + 1 = 7 - 2D$).

4.2. Analytical model for hysteresis friction

We consider the profile of a counterface of the sliding rubber (e.g. a road surface) as a realization of a stochastic process $z(x)$ where the heights determine the local strains of the rubber. Then, the total macroscopically observable energy dissipated as hysteretic friction becomes

$$\Delta E_{diss} \equiv \langle \Delta \tilde{E}_{diss} \rangle = + \frac{V}{2(2\pi)^2} T \int d\omega \omega E''(\omega) S(\omega) \quad (4.11)$$

Here, $S(\omega)$ denotes the spectral power density that—according to the Wiener–Khinchin theorem—corresponds to the Fourier-transform of the auto-correlation of the roughness induced strain during the sliding process of rubber over stationary surfaces (Section 2):

$$\langle \hat{\varepsilon}(\omega) \hat{\varepsilon}^*(\omega') \rangle = \frac{1}{2} S(\omega) \delta(\omega - \omega') \quad (4.12)$$

$T = 2\pi\delta(0)$ in Eq. (4.11) is the total time the oscillating stress has acted on the rubber solid. If F_n is the normal force, then $\sigma_0 = F_n/A_0$ is the normal stress. The quantity $A_0 = L^2$ is the contact area with L a length of order the diameter of contact area between the substrate and the rubber surface. The main part of the energy dissipation occur in a volume $V = A_0 \langle z_p \rangle$ where $\langle z_p \rangle$ is the average penetration depth of the rubber into the surface.

The energy dissipation per unit time $\Delta E_{diss}/T$ must equal the product $F \cdot v$ between the friction force F and the sliding velocity v . Then, one obtains

$$F = \frac{V}{2(2\pi)^2} \frac{1}{v} \int d\omega \omega E''(\omega) S(\omega) \quad (4.13)$$

and the friction coefficient

$$\mu = \frac{F}{F_n} = \frac{1}{2(2\pi)^2} \frac{\langle z_p \rangle}{\sigma_0 v} \int d\omega \omega E''(\omega) S(\omega) \quad (4.14)$$

In the case of a self-affine track the spectral power density is given according to the power law Eq. (4.9). In the frequency scale it takes the form:

$$S(\omega) = S_0 \left(\frac{\omega}{\omega_{\min}} \right)^{-\beta} \quad \text{for } \omega > \omega_{\min} \quad (4.15)$$

with $\omega = 2\pi\nu f$ and $\omega_{\min} = 2\pi\nu/\xi_{||}$. The front factor S_0 can be evaluated similar to the procedure described in section 4.1 if now the time dependent auto-correlation function $\Gamma_\varepsilon(t)$ is considered. Then, the variance is given by $\varphi^2 = \Gamma_\varepsilon(0) = \varepsilon_{\max}^2/2$ where $\varepsilon_{\max} = \xi_{\perp}/\xi_{||}$ indicates the maximum strain. This yields, similar to Eq. (4.9):

$$S_0 = \frac{H\varepsilon_{\max}^2\xi_{||}}{2\pi\nu} = \frac{H\xi_{\perp}^2}{2\pi\nu\xi_{||}} \quad (4.16)$$

Contrary to the topothesy k , the front factor S_0 depends on the sliding velocity and $\dim[S_0] = \dim[S(\omega)] = \text{time}$. If Eqs. (4.15) and (4.16), are inserted into Eq. (4.14) one obtains for the hysteretic friction coefficient:

$$\mu = \frac{1}{2(2\pi)^3} \frac{(\beta-1)}{2} \frac{\langle z_p \rangle \xi_{\perp}^2}{\sigma_0 \xi_{||} v^2} \int_{\omega_{\min}}^{\omega_{\max}} \omega \left(\frac{\omega}{\omega_{\min}} \right)^{-\beta} E''(\omega) d\omega \quad (4.17)$$

with the cut-off frequencies

$$\omega_{\max} = 2\pi \frac{v}{\lambda_{\min}} \quad \text{and} \quad \omega_{\min} = 2\pi \frac{v}{\xi_{||}} \quad (4.18)$$

Here, we have now introduced an upper cut-off frequency ω_{\max} into the integral. The corresponding lower cut-off length λ_{\min} of the spectra of road asperities always exists for physical systems.

4.3. Frictional behavior of natural rubber system

To capture the frictional characteristics of NR systems, the glass surface was considered as shown in **Figure 4.3**. Here, the viscoelastic modulus obtained using the CG MD simulations were used to calculate how the friction depends on the sliding velocity. We assumed that there are two contributions to the friction, one from the viscoelastic deformations of the rubber surface by the roughness of substrate, and one from the area of contact. To handle the contact area, the following relation for the mean penetration depth was used which was proposed by Heinrich model:

$$\langle z_p \rangle \approx \frac{\pi \xi_{||}}{E'(\omega_{\min})} \sigma_0 \quad (4.19)$$

Under the normal loading of 0.3MPa, the mean penetration depth was calculated considering the range of velocity from 10^{-1} to 10^3 m/s (**Figure 4.4**). As expected, with increasing sliding velocity, the penetration depth tends to decrease so that the contact area will decrease.

- **Influence of surface characteristics**

The friction coefficient was computed with using Eq. (4.17) for the NR system, unvulcanized NR, vulcanized NR, and filled-NR. The results for vulcanized NR with the different types of surface (see **Figure 4.5**) are illustrated in **Figure 4.6**. Overall, in a relatively rough surface, higher friction coefficients are observed and varying with sliding velocity. Depending on the excitation frequency which is determined by sliding velocity, the dynamic moduli of rubber are varied as observed in the previous section 3.4. Thus, as the sliding velocity increases, the frictional coefficients are changed. With the comparison to other simulation result and experiment, the present results show a good agreement in terms of both quantitative and qualitative senses.

- **Influence of temperature change**

The variation of temperature is of significant factor to modify the fundamental characteristics polymer materials. In that regard, the frictional behavior is substantially influenced by temperature. Herein, for the surface 1, the friction coefficients were calculated with different temperature ranges from 263 K to 400 K. As shown in **Figure 4.7**, the overall friction coefficient tends to decrease with increasing temperature. Main reason behind this observation is attributed to a reduction of loss modulus with temperature increment. Another important feature can be seen from the result is that the velocity at a peak friction coefficient is increasing with temperature. It is generally understood that the frictional behavior is governed by the frequency-dependent loss factor.

With the temperature rise, the frequency range where the peak of loss factor exists also increases. Thus, under a given sliding velocity and surface geometry, with increasing temperature it is natural to observe a peak friction coefficient at a higher velocity region.

- **Influence of microstructure change**

As already observed in the section 3.4, the viscoelastic characteristics are significantly modified with microstructural changes: vulcanization of rubber chain and reinforcing nanofillers. In **Figure 4.8**, the effects of both microstructural variations on the frictional behavior are illustrated. As expected, vulcanization and silica filler inclusions are likely to increase friction coefficient, since these microstructural modifications lead a moderate increment in frequency-dependent loss modulus, which is attributed to internal energy dissipation due to surface-induced deformation.

- **Influence of normal pressure**

When it comes to dealing with the area of contact in reality, the applied normal pressure is of a critical importance. To understand the influence of normal pressure on frictional behavior, a range of normal pressure from 0.1 MPa to 0.5 MPa was applied on VR2 and NR4 system. As can be seen in **Figure 4.9**, frictional master curves regarding varying velocity and normal pressure can be obtained. With increasing applied normal pressure, friction coefficients tend to slightly decrease. The area of contact is increasing with the increment of normal pressure; however, the tangential frictional force generated

from roughness-induced deformation is not affected much.

Frictional behavior is complex nature since it is influenced by many variables: viscoelastic property, roughness, temperature, sliding velocity, and normal pressure. Herein, based on the viscoelastic properties obtained from the CG MD simulations, the influences of those parameters were examined and discussed with using the analytical model, and the detailed friction coefficients were quantified. Considering the operation condition for the mechanical component composed of rubber, the present simulation framework can provide a reasonable guideline for designing a mechanical device in contact with other components.

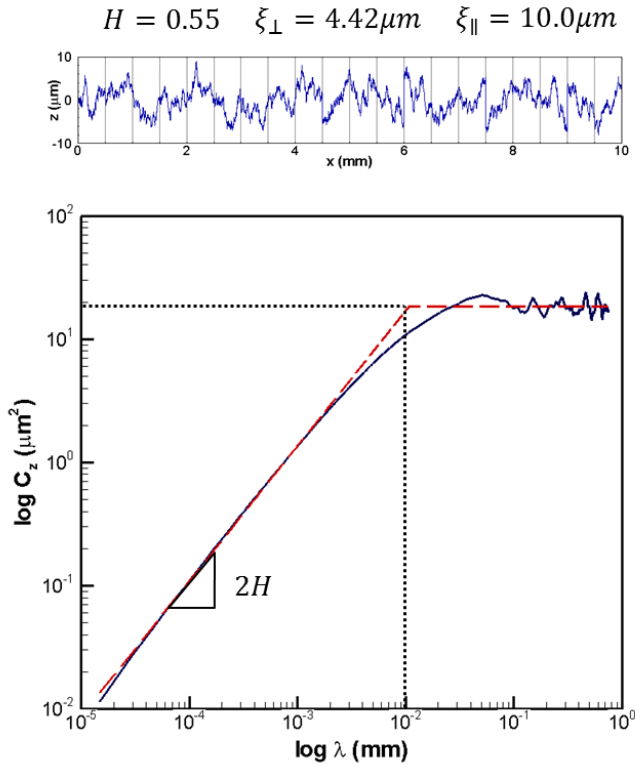


Figure 4.3. Smooth glass surface profile with the height-different correlation function which represents the surface characteristics with the variables H , ξ_{\perp} , and ξ_{\parallel} .

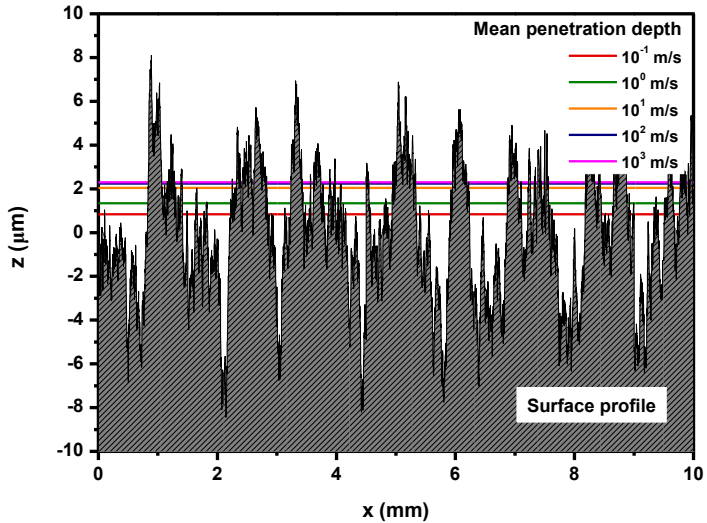
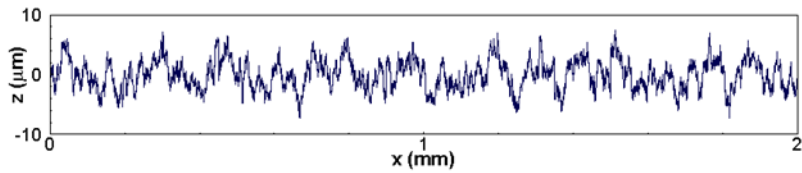
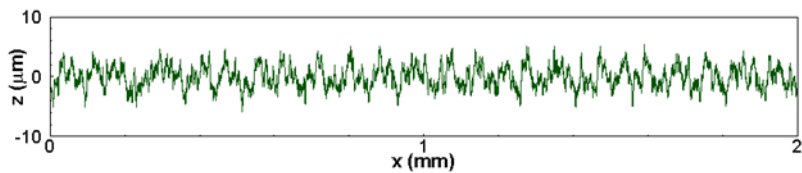


Figure 4.4. Mean penetration depth with increasing sliding velocity.

Surface 1



Surface 2



Surface 3

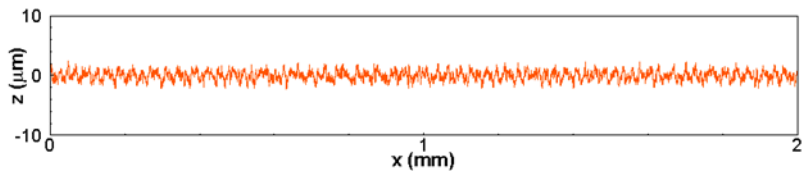


Figure 4.5. Different type of smooth surface: surface 1 with $H = 0.55$, $\xi_{\perp} = 4.42 \mu m$, and $\xi_{\parallel} = 10.0 \mu m$; surface 2 with $H = 0.60$, $\xi_{\perp} = 2.42 \mu m$, and $\xi_{\parallel} = 5.0 \mu m$; surface 3 with $H = 0.65$, $\xi_{\perp} = 1.05 \mu m$, and $\xi_{\parallel} = 2.0 \mu m$.

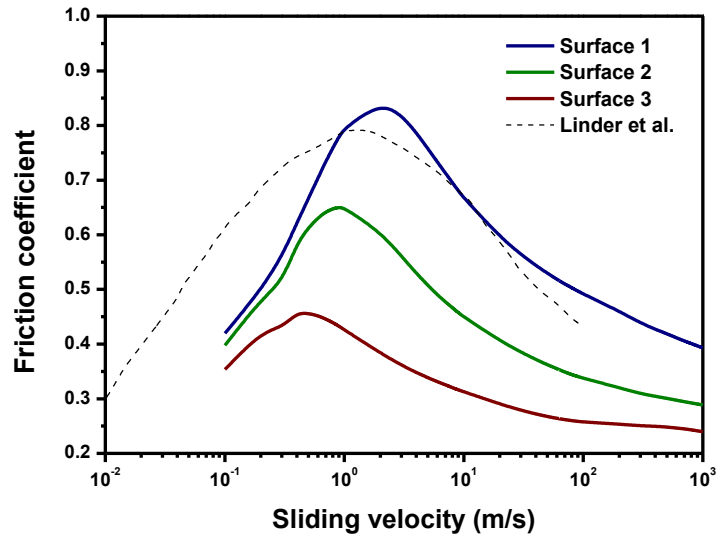


Figure 4.6. Friction coefficient of natural rubber systems with a range of sliding velocity.

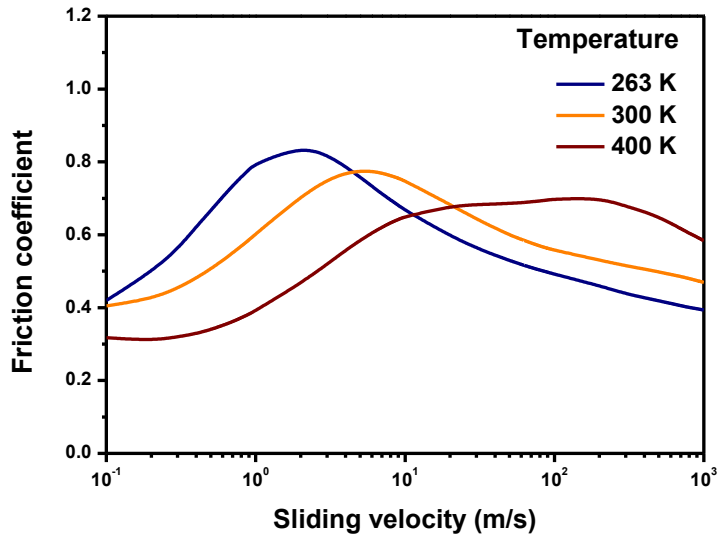
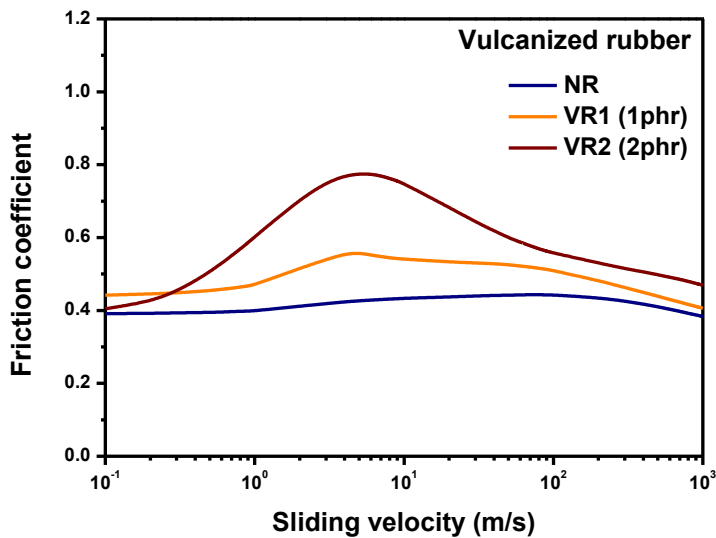


Figure 4.7. Friction coefficient of vulcanized rubber system with a range of sliding velocity at different temperature (260 K, 300 K, and 400 K)

(a)



(b)

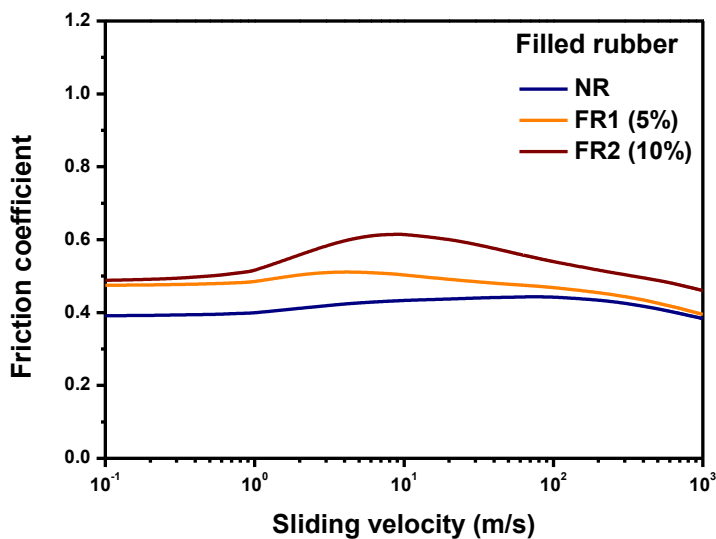
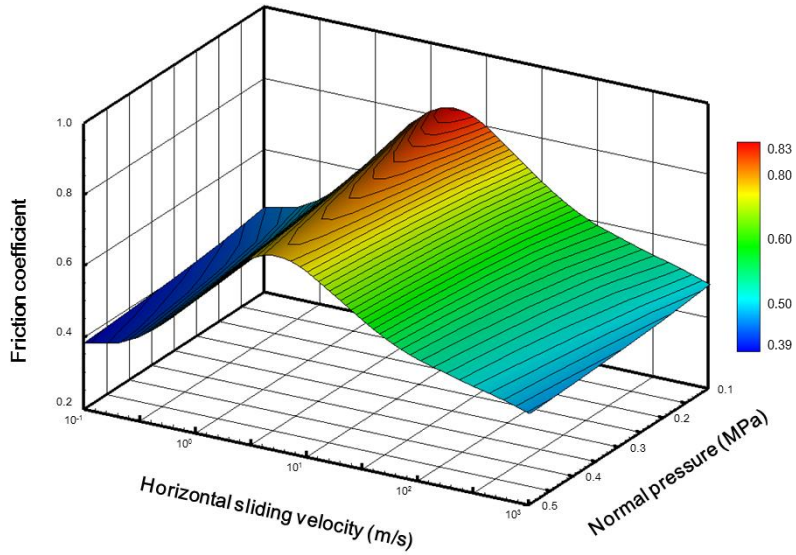


Figure 4.8. Effect of microstructural change on frictional behavior: (a) rubber vulcanization and (b) silica nanofiller inclusion.

(a)



(b)

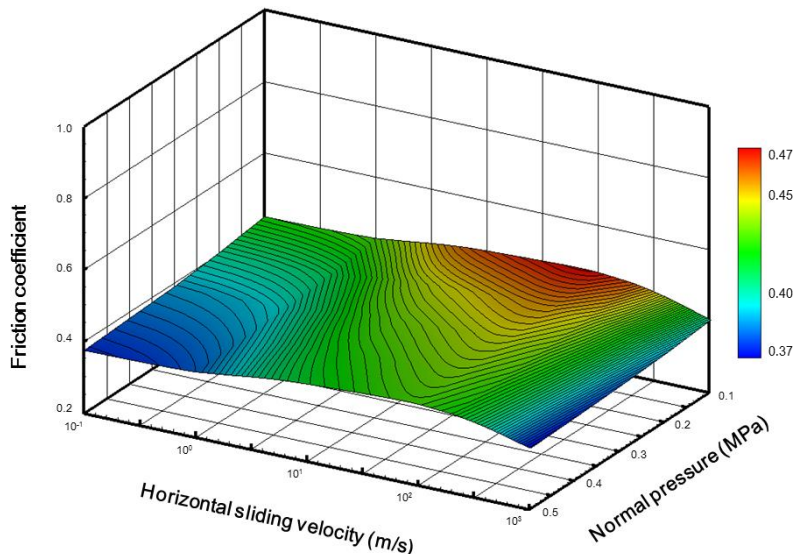


Figure 4.9. Frictional master curve with horizontal sliding velocity and normal pressure of natural rubber system: (a) vulcanized rubber and (b) unvulcanized rubber.

4.4. Numerical application: dynamic seal system

To avoid possible system failure associated frictional forces, a thorough consideration is necessary in a designing stage. Dynamic seals are one of key components for preventing fluid leakage out of mechanical equipment such as hydraulic systems, or fuel tanks. In many cases, seals undergo reciprocating frictional forces in contact with other moving components. Herein, to investigate the influence of friction on the mechanical element during the operation condition, hydraulic reciprocating O-ring seals are chosen as illustrated in **Figure 4.10**.

For the FE process, ABAQUS was employed; CPE3H elements (3-node linear plane strain triangle, hybrid with constant pressure) were used and the FE model is illustrated in **Figure 4.11**. To describe the contact condition between the rubber and groove of casing, the hard contact was applied for the normal behavior and the friction formulation was implemented for the tangential behavior via the penalty method. For the material property of rubber, the viscoelastic property obtained from the CG MD simulations is used with Prony coefficients. The groove of casing was regarded as a rigid body having the surface roughness of surface type 1 (**Figure 4.5**) without considering the relatively marginal deformation of groove surface. Considering the operating condition of temperature of 300 K, normal pressure of 0.3 MPa, and velocity of 3 m/s, the frictional coefficients for VR2 and NR4 were used from **Figure 4.9**.

The responses of rubber seal with both VR2 and NR4 were analyzed via

ABAQUS and the results are shown in **Figure 4.12**. As expected, the vulcanized rubber seal experiences larger deformation due to the frictional contact with groove, showing a hint of possible failure associated with seal extrusion. Though the result is based on the static approach without considering a realistic reciprocating motion, or variations of operating condition with time, it provides an important insight regarding rubber friction regarding the vulcanization. In the perspective of long-term durability, the further crosslinking of rubber can not only change the material property but also alter the frictional behavior. Therefore, to achieve a robust mechanical design for rubber material in contact with other component, the variation of frictional nature with aging or further crosslinking needs to be taken into account.

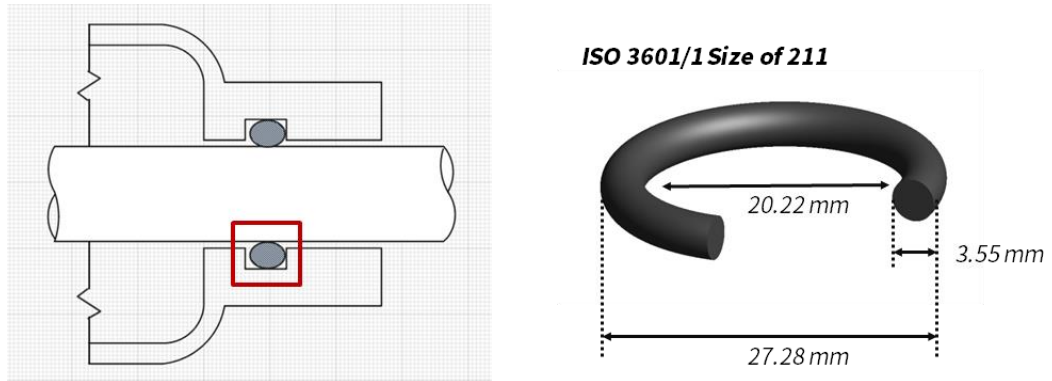


Figure 4.10. Schematic description of hydraulic reciprocating O-ring seal system.

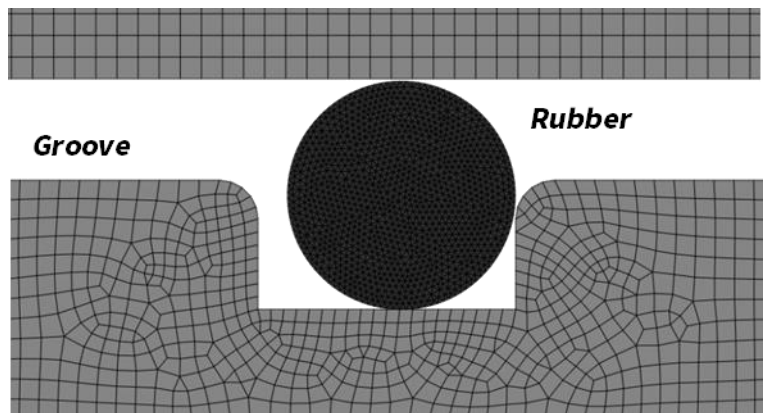
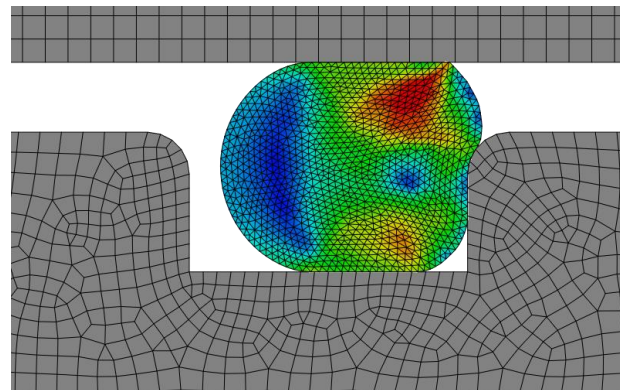


Figure 4.11. Finite element model for O-ring seal.

(a)



(b)

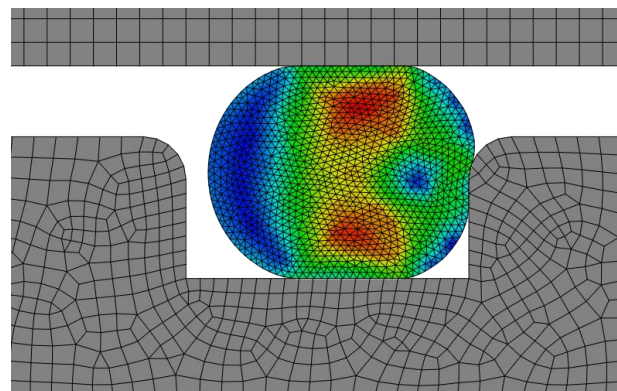


Figure 4.12. Finite element analysis of O-ring seal system considering the frictional contact: (a) vulcanized and (b) unvulcanized rubber seal.

5. Conclusion and Recommendation

In the present dissertation, the systematic multiscale simulation framework is proposed to predict the viscoelastic behavior and frictional characteristics of NR systems. When it comes to dealing with the dynamics nature of polymer, especially thermoplastic or elastomer, the conventional atomistic MD simulations have a limitation in time and length scale. To provide breakthrough in terms of applicable scale in MD simulations, the CG mapping scheme is employed, based on the atomistic structural features observed in the representative atomistic model. Herein, variations in micro-structural traits are examined: the molecular weight, rubber vulcanization, and silica reinforcing filler. Using an equilibrium MD technique, the time-dependent relaxation spectra of shear modulus are thoroughly studied. Moreover, to capture the frequency-dependent viscoelastic characteristics, the Fourier transformation is used to obtain the dynamic modulus of NR systems. The computed viscoelastic properties show reasonable agreements with the experimental observations.

The frictional characteristics of rubber are strongly related with the internal energy dissipation due to the deformation of rubber at the contact surface. Thus, this hysteresis friction can be computed from the dynamic modulus which is calculated from the CG MD simulations. With using the analytical method proposed by Heinrich and Klüppel, the friction coefficient when the rubber block sliding on the surface is predicted.

The present multiscale framework provides an effective way to assess the

viscoelastic behavior of elastomer system considering varying design parameters. Plus, with the contact circumstance in an engineering application, this method can predict the frictional coefficient and resulting stresses and displacements in the target materials. As a simulation-oriented method across a wide range of scale, from the atomistic consideration to the continuum scale, this method can provide valuable insights in the relaxation dynamics of polymeric systems which is directly connected to the viscoelastic behavior of polymer systems. Moreover, from the observation in the atomistic scale, the hysteresis friction behavior is successfully captured by up-scaling the information to the continuum regime.

This work can be expanded the following ways. In the MD simulation perspectives, the viscoelastic properties of various polymer materials can be predicted. With the implementation of CG potential, the polymer properties can be reasonably reproduced in the CG domain and the time and length scale are substantially expanded. Following this mapping scheme, the viscoelastic behavior of other polymeric materials can also be predicted. In terms of time and length scale, it is possible to extend further. The degree of freedoms in the system can be more reduced using a lower-level CG mapping approach. In that case, the sensitivity regarding the level of CG needs to be thoroughly examined.

For the frictional behavior of elastomer, other contributions such as adhesion and flash temperature can be included. Combined with those terms in the frictional characteristics, more precise prediction can be made. Moreover, with the implementation

of finite element analysis, other friction-induced phenomena can be taken into account as an extension of the present work.

Appendix A. Multiscale Modeling of Interphase in Crosslinked Epoxy Nanocomposites

A.1. Overview

Polymer crosslinking has extended engineering applications of polymer materials providing enhanced performances compared to the linear polymers. Epoxy resins, defined as thermoset polymers, exhibit high specific stiffness, high strength, thermal stability, and chemical resistance property due to the crosslinked polymer networks by strong covalent bonds⁷². In addition to excellent property, the ease of processing of epoxy offers various applications for matrix materials with the incorporation of reinforcing fillers⁷³⁻⁷⁵. The fundamental characteristics of epoxy resins are substantially modified according to the degree of crosslinking⁷⁶.

The region of the polymer matrix near the filler surface is typically termed the interphase, where polymer-filler interactions modify the dynamics and physical properties of polymer segments. With decreasing filler dimensions to a nanometer scale, the polymer dynamics change as the interfacial interactions become prominent since nanoparticles have an extremely high surface area to volume ratio⁷⁵. Moreover, while a

relatively small interphase region exists in conventional micron-filled composites, it has been demonstrated that with the presence of well-dispersed nanofillers in the polymer matrix, the interphase zones can percolate into the entire nanocomposites system, thus dominating the bulk polymer properties⁷⁷⁻⁸⁰.

In order to predict and control the properties of polymer nanocomposites quantitatively, the interfacial region needs to be characterized in terms of the various design parameters considered in the nanocomposites systems. Based on the general agreement that the formation of the interphase zones is attributed to the retarded polymer dynamics by the interfacial interactions between the fillers and polymer matrix^{77, 81}, the interphase creation and the interfacial characteristics of nanocomposites with crosslinked polymer need profound consideration, since the polymer dynamics near the surface are simultaneously influenced by the interfacial interactions and the crosslinked network topology^{78, 82}. While the perturbations of local structural and dynamical properties of thermoplastic polymer matrix surrounding embedded nanofillers have been intensively investigated by experimental and computational methods⁸³⁻⁸⁴, understanding of the interphase zones of nanocomposites with crosslinked polymer is still limited.

The nature of experiments makes it challenging to independently distinguish one effect from many parameters that affect the properties of nanocomposites, such as the interfacial characteristics and the interphase properties in epoxy nanocomposites. Regarding this aspect, molecular dynamics (MD) simulations have been used to provide valuable insights for understanding polymer physics especially in the interfacial zone of

nanocomposites systems with thermoset matrix^{83, 85-87}. Together with the MD simulations, a multiscale framework combined with a continuum regime has offered effective ways to understand nanoscale physics regarding the interphase in composite systems.

A.2. Interfacial nature of crosslinked epoxy with nanofiller

The MD simulation offers a reasonable way to understand the interfacial communication between the polymer matrix and nanofillers⁸⁸. In the present molecular models without considering any surface modifications, non-bond interactions between the silica particle and epoxy matrix govern the communication of interfacial dynamics, which play a key role in determining the interphase characteristics. To evaluate the changes of intrinsic adhesion strength at the interface with varying crosslink densities and filler sizes, the non-bond interfacial interaction energy/unit volume was calculated from the equilibrated unit cells, defined as:

$$\rho_{interaction} = \frac{E_{composite} - (E_{particle} + E_{matrix})}{V_{particle}} \quad (\text{A.1})$$

where $E_{composite}$, $E_{particle}$, and E_{matrix} denote the potential energy of the nanocomposite, particle, and matrix, respectively, each of which was obtained from the single point energy of the final configuration of nanocomposites after the equilibration process, and $V_{particle}$ is the volume of particle for each nanocomposite

The interfacial interaction energy density (see **Figure A.1**), where the negative

values of non-bonding energy represent the interfacial attraction of the polymer matrix with the silica particle, provides an important physical interpretation regarding the variation of interfacial attraction with the particle size and crosslink density. As the embedded filler size decreases, the particle tends to entail high non-bonding interaction energy density, which corresponds to the increasing number of non-bonding pairs per unit volume of particle. Interestingly, the interfacial adhesive interactions between the particle and matrix are weakened by the presence of more crosslinks. The highly crosslinked epoxy matrix is relatively less attractive to the silica surface than the matrix with lower crosslink densities. This behavior is most likely due to the disturbed interfacial communications at the particle surface with increasing crosslinking conversion.

From a simple molecular structure consisting of a planar silica layer, one molecular of EPON 862, and two molecules of TETA, the changes of non-bond characteristics between epoxy have been observed. As can be seen in **Figure A.2 (a)**, non-bond characteristics between epoxy molecules and silica are altered with curing degrees compared to the uncured reference state; the magnitude of the attractive non-bond interactions of epoxy to the silica surface decreases, and the equilibrium distance between the epoxy molecules and the silica gradually increases with producing more crosslinks. This interfacial degradation with crosslinking is supported by the variation of non-bond characteristics of participating atoms during the curing reaction as given in **Figure A.2 (b)**. In the uncured reference state, the N-C-O atoms (the specific part of resin and hardener involving the crosslinking reaction with atomic connectivity changes) have

intrinsically repulsive interfacial characteristics (positive sign) to the silica surface. With the formation of crosslinks, new covalent bonds between C and N atoms are formed, accompanied with the valence changes of the N-C-O atoms, increases in the magnitude of repulsion between the N-C-O and silica, and further increases in the equilibrium distance.

This MD and MM simulation result offers an important insight into the nature of interfacial communications at the surface especially with crosslinking which is governed by the non-bond interactions between the epoxy and silica. As the number of crosslinks increases, the repulsive interactions of participating atoms (N-C-O) with silica gradually increase, inducing the degradation of interfacial interactions in highly crosslinked epoxy nanocomposites. Since the interphase properties are strongly influenced by the non-bond interactions at the interface in this study, the variations of interfacial interactions during the crosslinking reaction demand a thorough consideration to understand the interphase characteristics of crosslinked epoxy nanocomposites.

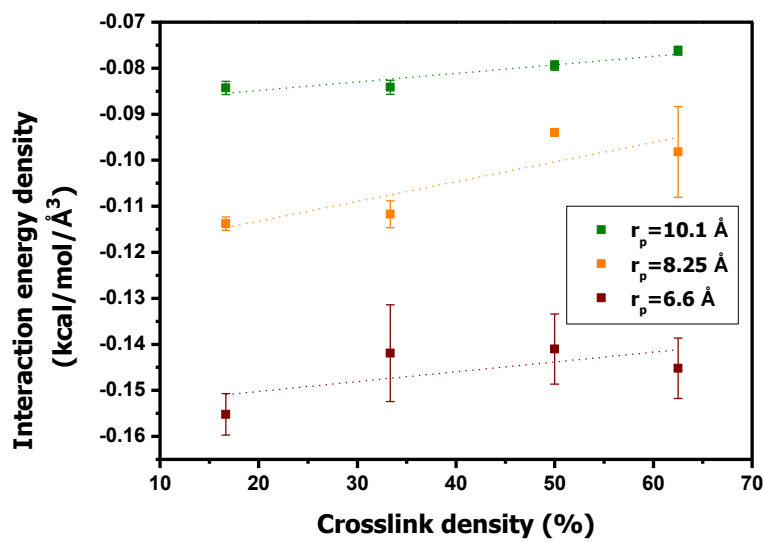
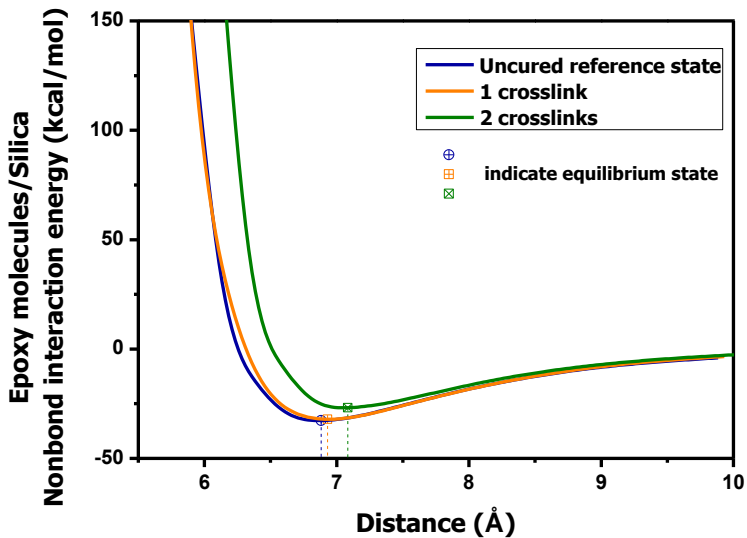


Figure A.1. Interfacial interaction energy density of crosslinked epoxy/silica nanocomposites with different crosslink densities.

(a)



(b)

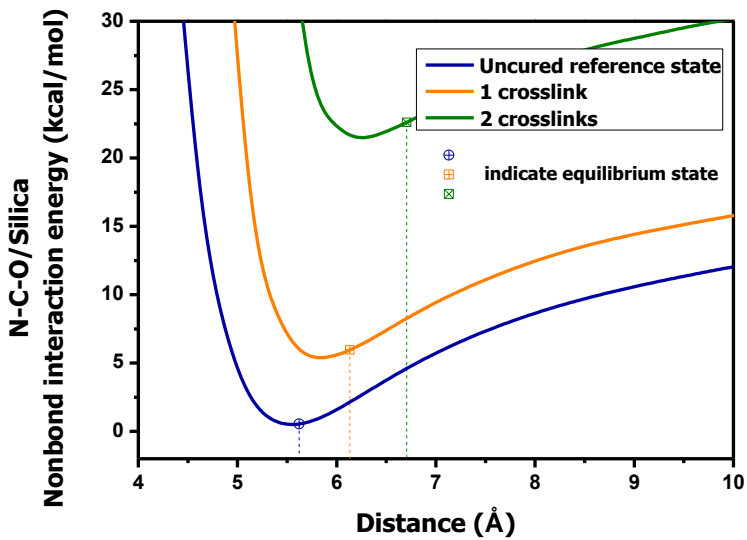


Figure A.2. Variation of non-bond characteristics (a) between epoxy molecules and silica, and (b) between N-C-O atoms and silica with crosslinking reaction.

A.3. Characterization of interphase property with multiscale modeling

In order to characterize the interphase behavior, the multi-inclusion model consisting of three-homogeneous and isotropic coaxial phases is implemented. Each phase is embedded into an infinite medium and perfectly bonded to other phases.

The closed form solution of the effective stiffness tensor of the present three-phased model \mathbf{C} is defined as,

$$\mathbf{C} = \mathbf{C}_\infty \left[\mathbf{I} + (\mathbf{S} - \mathbf{I}) \left(f_p \boldsymbol{\Phi}_p + f_i \boldsymbol{\Phi}_i + f_m \boldsymbol{\Phi}_m \right) \right] \left[\mathbf{I} + \mathbf{S} \left(f_p \boldsymbol{\Phi}_p + f_i \boldsymbol{\Phi}_i + f_m \boldsymbol{\Phi}_m \right) \right]^{-1} \quad (\text{A.2})$$

where f is the volume fraction of each phase, and the terms in bold typeface refer to the tensor quantities; \mathbf{C}_∞ is the stiffness of the infinite domain, \mathbf{S} and \mathbf{I} are the Eshelby tensor⁸⁹ for the spherical inclusion and identity tensor, respectively, and $\boldsymbol{\Phi}$ is the fourth-order eigenstrain concentration tensor of each phase. The subscripts p , i , and m denote the nanoparticle, interphase, and matrix, respectively. The eigenstrain concentration tensor $\boldsymbol{\Phi}$ for the (\bullet) phase is given by,

$$\boldsymbol{\Phi}_{(\bullet)} = \left[\left(\mathbf{C}_\infty - \mathbf{C}_{(\bullet)} \right)^{-1} \mathbf{C}_\infty - \mathbf{S} \right]^{-1}. \quad (\text{A.3})$$

The overall CTE of the three-phased composites in the multi inclusion model is given as,

$$\alpha = \mathbf{C}^{-1} \mathbf{C}_\infty [\mathbf{I} + \Phi \mathbf{S}]^{-1} \\ \left[f_p (\Phi_p (\mathbf{S} - \mathbf{I}) + \mathbf{I}) : \alpha_p + f_i (\Phi_i (\mathbf{S} - \mathbf{I}) + \mathbf{I}) : \alpha_i + f_m (\Phi_m (\mathbf{S} - \mathbf{I}) + \mathbf{I}) : \alpha_m \right] \quad (A.4)$$

where $\Phi = \sum_i f_i \Phi_i$.

The volume fraction of the interphase for each nanocomposite was obtained based on the constant thickness of 6.9 Å for simplicity. The stiffness tensor of the infinite medium was defined as $\mathbf{C}_\infty = \mathbf{C}_m$ considering the moderate concentration effect of nanofillers. The stiffness and CTE of the matrix phase are assumed to be the same as those of pure epoxy systems, corresponding to a specific crosslink conversion. The elastic and thermal properties of the interphase can then be calculated using the inverse form of Eqs. (A.2)-(A.4). As observed in the previous MD and MM results illustrated in Figures. A.1 and A.2, the interfacial adhesion is likely to be varied with crosslinking degree and particle size. By replacing the filler-matrix interfacial compatibility with a perfect bonding condition between each phase, the interphase properties obtained from the micromechanics model used herein is interpreted as the effective interphase properties⁸⁸ which inherently include the variations of both structural characteristics and interfacial compliance with crosslinking and filler size.

Although the effective interphase concept does not specifically distinguish between the interphase property and the interfacial compliance, it can be implemented in a continuum model to reflect the degradation of the interphase effect with increasing

crosslinking as well as embedded particle size. According to the present multi-inclusion model, the elastic modulus and CTE of composites as given in **Eqs. (A.2)-(A.4)** can be defined as the following,

$$\begin{aligned}\mathbf{C} &= \mathbf{C}(\mathbf{C}_p, \mathbf{C}_m, \mathbf{C}_i, f_p, f_m, f_i) \\ \alpha &= \alpha(\mathbf{C}_p, \mathbf{C}_m, \mathbf{C}_i, \alpha_p, \alpha_m, \alpha_i, f_p, f_m, f_i)\end{aligned}\quad (\text{A.5})$$

Herein, the effective interphase has been characterized as $\mathbf{C}_i = \mathbf{C}(\xi, r_p^*)$ and $\alpha_i = \alpha(\xi, r_p^*)$, which represent the variation of elastic modulus and CTE of the interphase region and the interfacial compliance, respectively. Together with the assumption that the property of the epoxy matrix is the same as that of neat epoxy, $\mathbf{C}_m = \mathbf{C}(\xi)$ and $\alpha_m = \alpha(\xi)$, the thermomechanical properties can be predicted from the micromechanics-based multi-inclusion model using **Eqs. (A.2)-(A.4)** with the incorporation of the effective interphase. **Fig. A.3** shows the overview of the present multiscale model; refer to the article for the detailed formulations and results⁹⁰.

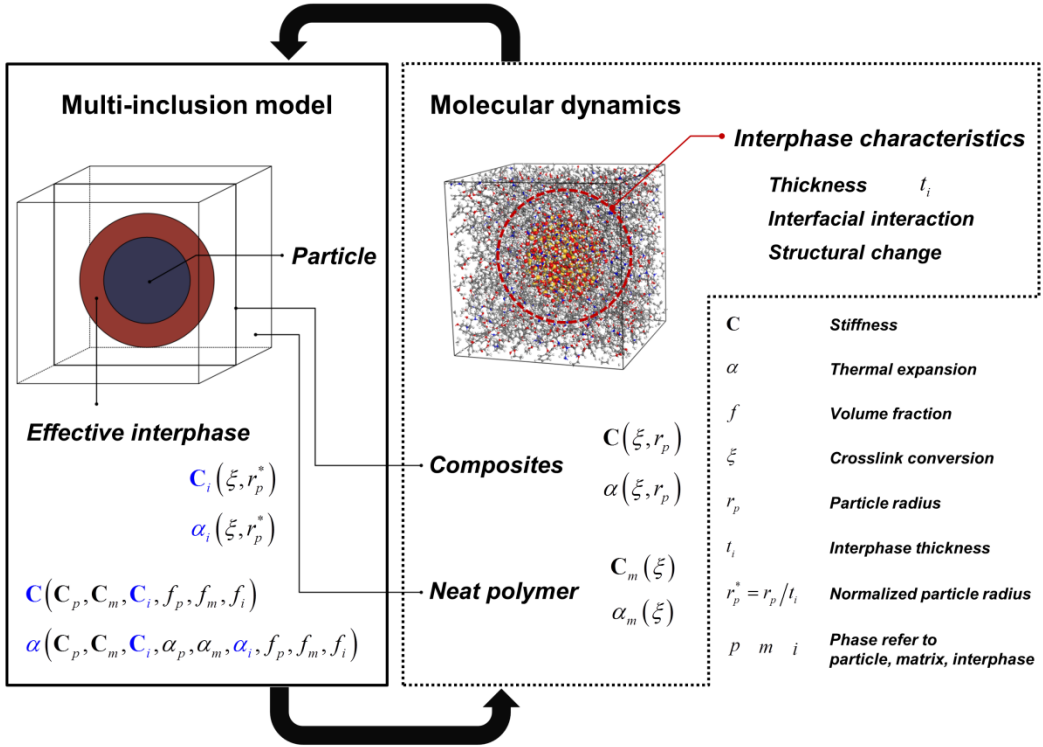


Figure A.3. Overall schematic of the multiscale modeling of the interphase property; blue-colored terms (For interpretation of the references to color in this figure legend, the reader is referred to the web version of the article⁹⁰). indicate the values predicted from the multi-inclusion model.

A.4. Summary of appendix A

Atomic simulations were performed to investigate the interfacial characteristics of epoxy/silica nanocomposites with the crosslinking conversions of epoxy matrix. The results of MD and MM simulations demonstrate that the nature of the interfacial interactions between the silica and epoxy matrix show a clear dependency with the degree of crosslinking; the interfacial adhesions are substantially disturbed with the formation of further crosslinks in the epoxy, resulting in disturbed enhancing effects on stiffness and thermal stability with crosslinking. As far as the structural conformation change of the interphase with the conversion degree is concerned, important features were observed supporting the reduction of interfacial characteristics. The results of the radial mass density profiles, the local crosslinks distributions, and the free volumes at the filler surface consistently demonstrate that the structural characteristics are substantially influenced by the nature of interfacial communication with the crosslink conversion. Since the behavior of the interphase zone is strongly governed by the interfacial communication at the filler surface, the variations of interfacial characteristics with crosslinking need to be taken into account to understand the interphase of epoxy nanocomposite systems as well as their reinforcing mechanism. In this work, together with profound considerations of varying crosslink conversion and filler size in epoxy nanocomposites, a multiscale scheme to characterize the interphase region is proposed with the incorporation of molecular simulations and a micromechanics-based continuum

model. Based on the findings of the atomistic simulations, the elastic modulus and CTE of nanocomposites are characterized in terms of crosslink conversion and normalized filler size. From the modeled thermomechanical properties of epoxy/silica nanocomposites, the interphase zone is further characterized with the aid of the multi-inclusion continuum model. The effective interphase zone is addressed to reflect the variations of interfacial adhesion and the interphase property. The degradation of the effective interphase zone is modeled with crosslink conversion and filler size. The micromechanics predictions from the effective interphase for the thermomechanical properties of nanocomposites are confirmed and compared to the MD results and the present model for composites.

From the multiscale framework presented herein, the information at the molecular level regarding the interphase region of epoxy nanocomposites is transferred to the equivalent continuum model. Addressing the effective interphase concept, the interphase properties obtained from the present multi-inclusion model are termed as an effective interphase property. Since a perfect interfacial bonding condition is applied in the continuum model, the effective interphase property is not an independent property of the interphase but an effective property which reflects the variations of both structural and interfacial characteristics with the crosslink conversion and particle size. However, the present multiscale modeling using the effective interphase concept will serve as an efficient bridging scheme to understand the complex interfacial nature of crosslinked epoxy composite systems and their structure-property relationship, providing a design

guideline for epoxy nanocomposites in their static property (elastic modulus and CTE) on the basis of the detailed interphase characteristics with varying crosslink conversions and particle sizes. The multiscale modeling scheme proposed herein can be further extended to the various multifunctional characteristics and the dynamic behavior with a profound consideration of the interfacial region in the nanocomposites system.

Appendix B. Multiscale Analysis of Load Transfer in Crosslinked Epoxy Nanocomposites

B.1. Overview

Nanoparticles have extensively broadened the engineering applications of epoxy resins in various industrial fields such as coatings, adhesives, electronic, automobile, and aerospace, etc⁹¹. With the incorporation of nanoparticles in crosslinked epoxy matrices, nanocomposite materials offer enhanced thermomechanical, electrical, or viscoelastic properties compared to the neat epoxy resins. Overall, the properties of polymer-based composite system are attributed to the combination of the filler and polymer matrix, and a variety of combinations with a diverse class of fillers and polymer materials can strengthen the functionality of composites.

The inorganic nanoparticles have a much higher strength and modulus than engineering polymers which can be used as reinforcements for nanocomposite systems to

enhance the mechanical properties. As the filler materials are introduced into polymer matrices, structural morphologies and polymer dynamics are substantially perturbed by the interfacial interactions between the filler and polymers, resulting in altered properties and characteristics of polymers in the vicinity of the filler. Given the large surface area to volume ratio with nanoparticles, the interfacial region (i.e., interphase) is regarded as a significant factor directly affecting the mechanical property by influencing the load transfer from the polymer matrices to the reinforcing filler. Hence, it is quintessential that the nanoscale interface should be thoroughly understood to efficiently tailor and design the bulk properties of nanocomposite system.

Experimental works have been conducted to investigate the load transfer in polymer nanocomposites considering the variations of structural and dynamic characteristics of polymer chains due to the presence of the polymer-nanoparticle interaction. The Raman spectroscopy has been successively employed to obtain detailed information regarding the stress responses in the domains of nanocomposites. Gong et al.⁹² reported that the stress transfer in graphene nanocomposites was investigated at the atomistic level with using an experimental technique associated with the Raman spectroscopy. Further, the interfacial load transfer in more complex composite system known as a nanohybrid was investigated by Nie et al.⁹³ While experimental techniques have contributed to characterize the load transfer in nanocomposites, it is challenging to distinguish and quantify one effect from many other parameters that influence the nature of interfacial region.

Regarding this aspect, MD simulations have been extensively used to provide valuable insights on the interfacial characteristics of polymer-based nanocomposites. In particular, the interfacial load transfer between the graphene and polyethylene (PE) polymer were studied by Awasthi et al.⁸⁵ with using a representative bilayer structure. Li and Seidel⁹⁴ reported a multiscale modeling for the elastic properties of carbon nanotube-PE nanocomposites which is based on the nanoscale load transfer characteristics with MD simulations. Although many attempts have been made to investigate the load transfer in polymer nanocomposites, understanding of interfacial nature of nanocomposites with thermoset resin is still limited.

In this section, a detailed load transfer characteristics in epoxy-based nanocomposites is investigated with the aid of MD simulations. Given a mechanical loading on the nanocomposite system, the variations of structural morphologies and interfacial polymer dynamics are monitored at the atomistic scale. The influence of different crosslinking conversions of epoxy matrix and filler volume fractions are also taken into account. Based on the findings in MD simulations, a multiscale model is proposed to describe the nature of internal stress transfer of nanocomposites from the matrix to the filler.

B.2. Internal stress transfer in interfacial region

To examine the detailed stress transfer from the crosslinked epoxy matrices to

the SiC nanoparticle, a mechanical loading was imposed on the equilibrated structures of epoxy/SiC nanocomposites via non-equilibrium MD methods. The mechanical responses of the systems for each phase, the crosslinked epoxy matrix and the SiC nanoparticle, were monitored. To impose the tensile loading on the system with proper ensembles, LAMMPS⁶⁸ was implemented. Constant strain was introduced along the x, y, and z directions with the fix deform command at the engineering strain rate of 1×10^9 /s. While the unit cell was deformed for each direction, the dimensions of system in the other two directions were set to be adjustable under the atmospheric pressure (1 atm) and 300 K condition in the NPT ensemble, reflecting Poisson's effect in a given tensile deformation. From the tensile simulations, the stresses for each atom in both phases were calculated by the virial theorem defined in Eq. (B.1):

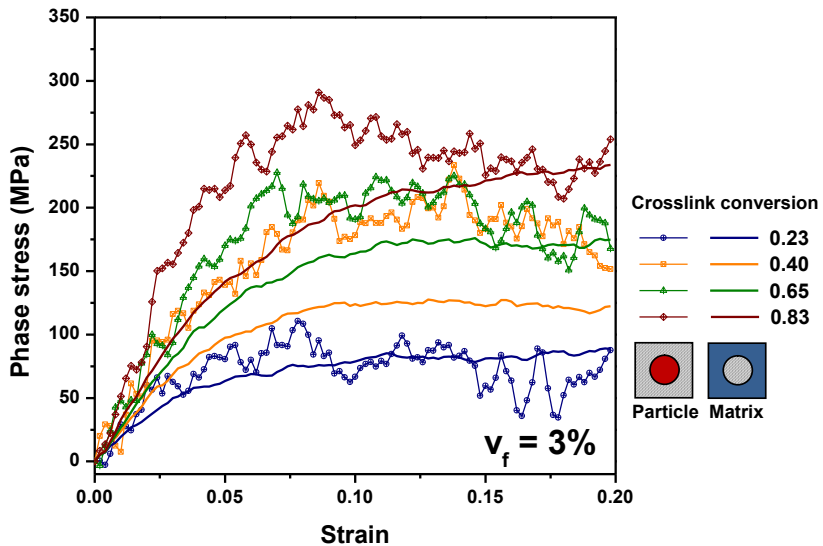
$$\sigma_{ij} = \frac{1}{V} \sum_{\alpha} \left[\frac{1}{2} \sum_{\alpha \neq \beta} (r_i^{\beta} - r_i^{\alpha}) f_j^{\alpha\beta} - m^{\alpha} (u_i^{\alpha} u_i^{\alpha}) \right] \quad (\text{B.1})$$

where V is the total volume, r^{α} , m^{α} , and u^{α} represent the position, mass, and velocity of the particle α , respectively, β indicates the neighbors of atom α in the system, f is the force exerted on alpha particle by beta particle, and the subscript i and j denote the value along the direction x, y, and z.

The stress-strain responses for each phase with respect to the given strain of overall nanocomposite systems are illustrated in **Figure B.1**. Given the same amount of deformation in the system, the interesting thing to be noted is that the particle phase accommodates much higher stresses and the stress deviation between the particle and

matrix phase is raised as the crosslinking conversion increases. In the system with the lower conversion of 0.23, both phases shows a similar stress-strain response for the strain range considered in this work. On the other hand, in the highly crosslinked nanocomposites (conversion of 0.83), it can be observed that the particle phase entails substantially higher stresses values with deformation as compared to the values of epoxy matrix phase. Herein, the stress deviation between the phases qualitatively indicates the amount of stress transfer from the matrix phase to the nanoparticle region. This result clearly indicates that the stress transfer characteristics in crosslinked epoxy nanocomposites tend to enhance as the crosslinking conversion increases.

(a)



(b)

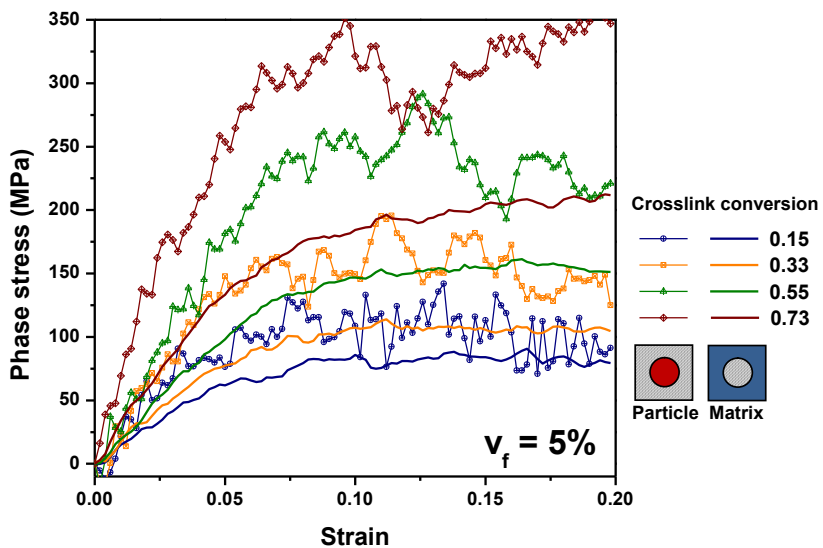


Figure B.1. Stress strain response of each phase (SiC particle and epoxy matrix) with varying crosslinking conversion: (a) 3% and (b) 5% of filler volume fraction.

B.3. Multiscale modeling of load transfer characteristics

To take into account the variation of internal stress transfer characteristics in the matrix domain with the crosslinking conversion and filler size, the weakened interface concept is introduced. The filler and matrix region is connected by the linear spring layer (without occupying volume) to describe the weakened interface characteristics near the reinforcing particulate depending on the curing conversion or filler dimension. Employing the weakened interface concept with the linear spring layer, the interface between the filler and matrix domain satisfies continuity in traction with discontinuity in displacement:

$$\begin{aligned}\Delta\sigma_{ij}n_j &= \left[\sigma_{ij}(S^+) - \sigma_{ij}(S^-) \right] n_j = 0 \\ \Delta u_i &= \left[u_i(S^+) - u_i(S^-) \right] = \eta_{ij}\sigma_{jk}n_k\end{aligned}\quad (\text{B.2})$$

where S and n_i represent the interface and its unit outward normal vector. Here, the superscripts + and – indicate the positive and negative sides, respectively, and the second order tensor η_{ij} is determined by the compliance of the weakened interface in the tangential (αT) and normal (αN) directions, respectively.

$$\eta_{ij} = \alpha_T \delta_{ij} + (\alpha_N - \alpha_T) n_i n_j \quad (\text{B.3})$$

where the second order tensor δ_{ij} is the Kronecker delta tensor. To describe the discontinuous displacement fields near the nanoparticle just in the normal direction (i.e., no sliding condition), we determine that the tangential directional coefficient (αT) is zero. The detail computational finite element homogenization procedures including the

weakened interfacial bonding condition with the cohesive zone modeling can be found in the work done by Song et al.⁹⁵ To minimize the differences of the effective nominal stress of the nanoparticles between the molecular dynamics simulations and the finite element homogenization analysis, we introduce the additional criteria as follows:

$$L(K_{nn}) = \int_0^{\varepsilon_{max}} \left| \Sigma_{par,xx}^{(MD)} - \Sigma_{par,xx}^{(Homog.)}(K_{nn}) \right| d\varepsilon_{xx,comp} \quad (\text{B.4a})$$

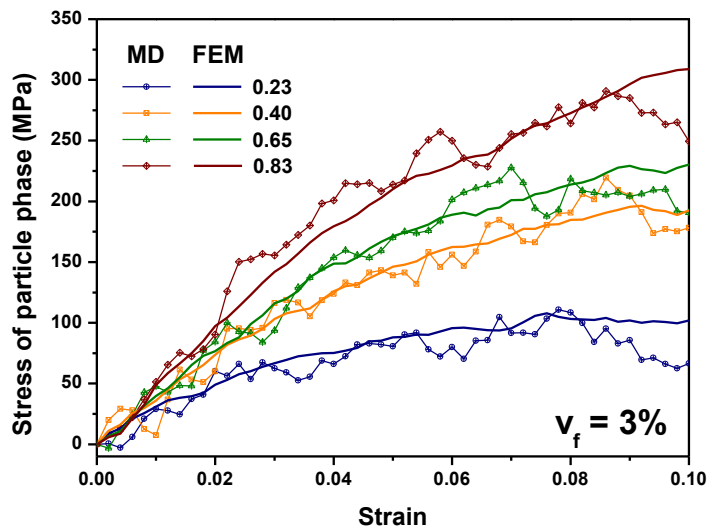
$$f_{\text{imperfect}}(E_{em}^{\text{sec}}, K_{nn}) = \left| \frac{\Sigma_{comp,xx}^{(MD)} - \Sigma_{comp,xx}^{(Homog.)}(E_{em}^{\text{sec}}, K_{nn})}{\Sigma_{comp,xx}^{(MD)}} \right| \quad (\text{B.4b})$$

where K_{nn} is the interfacial spring constant in normal direction. In this specific work, the ε_{max} is set as 0.1. The objectives of this iterative inverse algorithm are that the minimization of $L(K_{nn})$ with satisfying the inequality condition, $f_{\text{imperfect}} < 10^{-4}$.

With the weakened interface concept, the finite element model can reasonably describe the load transfer characteristics (see **Figure B.2**). The fundamental nature of internal stress transfer in nanocomposites is attributed to the formation of interphase region. This densely packed domain around the embedded particle substantially enhances the load transfer characteristics. While there are many issues over the thickness of the interphase region^{78,96}, it is fairly reasonable to assume that the molecular systems having the same filler size and crosslink conversion in matrix retain almost identical thicknesses of the interphase, especially in a dilute filler loading condition. In that sense, the effective volume fraction of the interphase zone over the entire nanocomposite system is larger in the higher filler volume fraction case. Thus, it is natural that the contribution of interphase region on the load transfer is more effective in the system with a higher filler

loading; this feature is manifested by the larger spring constant in 5% of filler volume fraction case compared to the 3%. The interfacial spring constant in the present model reflects not only the interfacial compliance with crosslinking but also the overall contribution of the interphase region on the load transfer characteristics for different filler volume fractions.

(a)



(b)

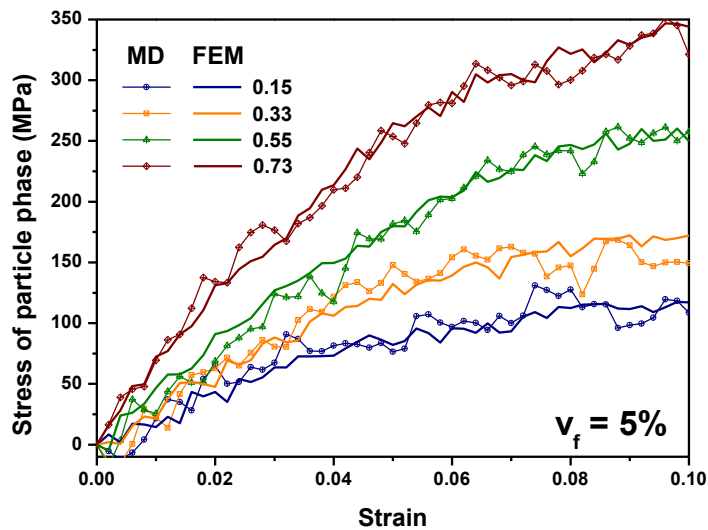


Figure B.2. Comparison of particle stress with strain between finite element model and molecular dynamics simulation: (a) 3% and (b) 5% of filler volume fraction.

B.4. Summary of appendix B

In the present multiscale model, detailed interfacial stress transfer characteristics of epoxy/SiC nanocomposites are investigated using MD simulations. From the MD simulations, the interfacial load transfer ability from the matrix to the filler in nanocomposites is enhanced with increasing crosslink conversion of epoxy matrix. Moreover, variations of interfacial characteristics with crosslink conversions are investigated as the tensile strains are applied. Due to the different nature of polymer segmental dynamics of epoxy matrix with crosslinking, abrupt structural changes are observed in highly crosslinked epoxy nanocomposites systems. To reflect the observation in the molecular level into the continuum scale, a homogenization-based FE model is proposed. Considering the interfacial imperfection, the present continuum model provides a reasonable prediction in terms of the interfacial load transfer characteristics of epoxy nanocomposites.

References

1. Heinrich, G.; Klüppel, M., Rubber friction, tread deformation and tire traction. *Wear* **2008**, *265* (7), 1052-1060.
2. Wagner, P.; Wriggers, P.; Veltmaat, L.; Clasen, H.; Prange, C.; Wies, B., Numerical multiscale modelling and experimental validation of low speed rubber friction on rough road surfaces including hysteretic and adhesive effects. *Tribology International* **2017**, *111*, 243-253.
3. Wagner, P.; Wriggers, P.; Klapproth, C.; Prange, C.; Wies, B., Multiscale FEM approach for hysteresis friction of rubber on rough surfaces. *Computer Methods in Applied Mechanics and Engineering* **2015**, *296*, 150-168.
4. Popov, V. L.; Dimaki, A.; Psakhie, S.; Popov, M., On the role of scales in contact mechanics and friction between elastomers and randomly rough self-affine surfaces. *Scientific Reports* **2015**, *5*, 11139.
5. Tuononen, A. J., Onset of frictional sliding of rubber–glass contact under dry and lubricated conditions. *Scientific Reports* **2016**, *6*, 27951.
6. Li, Q.; Dimaki, A.; Popov, M.; Psakhie, S. G.; Popov, V. L., Kinetics of the coefficient of friction of elastomers. *Scientific Reports* **2014**, *4*, 5795.
7. Goda, T. J., Effect of track roughness generated micro-hysterisis on rubber friction in case of (apparently) smooth surfaces. *Tribology International* **2016**, *93*, 142-150.

8. Popov, V. L.; Voll, L.; Li, Q.; Chai, Y. S.; Popov, M., Generalized law of friction between elastomers and differently shaped rough bodies. *Scientific Reports* **2014**, *4*, 3750.
9. Hartung, F.; Kienle, R.; Götz, T.; Winkler, T.; Ressel, W.; Eckstein, L.; Kaliske, M., Numerical determination of hysteresis friction on different length scales and comparison to experiments. *Tribology International* **2018**, *127*, 165-176.
10. Maegawa, S.; Itoigawa, F.; Nakamura, T., Effect of normal load on friction coefficient for sliding contact between rough rubber surface and rigid smooth plane. *Tribology International* **2015**, *92*, 335-343.
11. Baum, M. J.; Heepe, L.; Gorb, S. N., Friction behavior of a microstructured polymer surface inspired by snake skin. *Beilstein Journal of Nanotechnology* **2014**, *5*, 83-97.
12. Mahboob Kanafi, M.; Tuononen, A. J.; Dorogin, L.; Persson, B. N. J., Rubber friction on 3D-printed randomly rough surfaces at low and high sliding speeds. *Wear* **2017**, *376-377*, 1200-1206.
13. Persson, B. N. J.; Lorenz, B.; Shimizu, M.; Koishi, M., Multiscale Contact Mechanics with Application to Seals and Rubber Friction on Dry and Lubricated Surfaces. In *Designing of Elastomer Nanocomposites: From Theory to Applications*, Stöckelhuber, K. W.; Das, A.; Klüppel, M., Eds. Springer International Publishing: Cham, 2017; pp 103-156.
14. Farfán-Cabrera, L. I.; Gallardo-Hernández, E. A.; de la Rosa, C. S.; Vite-Torres, M., Micro-scale abrasive wear of some sealing elastomers. *Wear* **2017**, *376-377*, 1347-

1355.

15. Persson, J. S.; Tiwari, A.; Valbahs, E.; Tolpekina, T. V.; Persson, B. N. J., On the Use of Silicon Rubber Replica for Surface Topography Studies. *Tribology Letters* **2018**, *66* (4), 140.
16. Lang, A.; Klüppel, M., Influences of temperature and load on the dry friction behaviour of tire tread compounds in contact with rough granite. *Wear* **2017**, *380-381*, 15-25.
17. Persson, B. N. J., Theory of rubber friction and contact mechanics. *The Journal of chemical physics* **2001**, *115* (8), 3840-3861.
18. Wriggers, P.; Reinelt, J., Multi-scale approach for frictional contact of elastomers on rough rigid surfaces. *Computer Methods in Applied Mechanics and Engineering* **2009**, *198* (21), 1996-2008.
19. Heinrich, G., Hysteresis Friction of Sliding Rubbers on Rough and Fractal Surfaces. *Rubber Chemistry and Technology* **1997**, *70* (1), 1-14.
20. Uddin, M. S.; Ju, J., Multiscale modeling of a natural rubber: Bridging a coarse-grained molecular model to the rubber network theory. *Polymer* **2016**, *101*, 34-47.
21. Ketkaew, R.; Tantirungrotechai, Y., Dissipative Particle Dynamics Study of SWCNT Reinforced Natural Rubber Composite System: An Important Role of Self-Avoiding Model on Mechanical Properties. *Macromolecular Theory and Simulations*, 1700093-n/a.
22. Abdel-Goad, M.; Pyckhout-Hintzen, W.; Kahle, S.; Allgaier, J.; Richter, D.;

Fetters, L. J., Rheological Properties of 1,4-Polyisoprene over a Large Molecular Weight Range. *Macromolecules* **2004**, *37* (21), 8135-8144.

23. Stephen, R.; Raju, K. V. S. N.; Nair, S. V.; Varghese, S.; Oommen, Z.; Thomas, S., Mechanical and viscoelastic behavior of natural rubber and carboxylated styrene-butadiene rubber latex blends. *Journal of Applied Polymer Science* **2003**, *88* (11), 2639-2648.
24. Yagyu, H., Coarse-grained Molecular Dynamics Simulation of the Effects of Strain Rate on Tensile Stress of Cross-Linked Rubber. *Soft Materials* **2015**, *13* (4), 263-270.
25. Pavlov, A. S.; Khalatur, P. G., Fully atomistic molecular dynamics simulation of nanosilica-filled crosslinked polybutadiene. *Chemical Physics Letters* **2016**, *653*, 90-95.
26. Santangelo, P. G.; Roland, C. M., Temperature Dependence of Mechanical and Dielectric Relaxation in cis-1,4-Polyisoprene. *Macromolecules* **1998**, *31* (11), 3715-3719.
27. Arman, B.; Reddy, A. S.; Arya, G., Viscoelastic Properties and Shock Response of Coarse-Grained Models of Multiblock versus Diblock Copolymers: Insights into Dissipative Properties of Polyurea. *Macromolecules* **2012**, *45* (7), 3247-3255.
28. Hattemer, G. D.; Arya, G., Viscoelastic Properties of Polymer-Grafted Nanoparticle Composites from Molecular Dynamics Simulations. *Macromolecules* **2015**, *48* (4), 1240-1255.
29. Halverson, J. D.; Lee, W. B.; Grest, G. S.; Grosberg, A. Y.; Kremer, K., Molecular dynamics simulation study of nonconcatenated ring polymers in a melt. II.

- Dynamics. *The Journal of chemical physics* **2011**, *134* (20), 204905.
30. Sirk, T. W.; Karim, M.; Lenhart, J. L.; Andzelm, J. W.; Khare, R., Bi-modal polymer networks: Viscoelasticity and mechanics from molecular dynamics simulation. *Polymer*.
31. Eitan, A.; Fisher, F. T.; Andrews, R.; Brinson, L. C.; Schadler, L. S., Reinforcement mechanisms in MWCNT-filled polycarbonate. *Composites Science and Technology* **2006**, *66* (9), 1162-1173.
32. Deng, Y. J.; Peng, L. F.; Lai, X. M.; Fu, M. W.; Lin, Z. Q., Constitutive modeling of size effect on deformation behaviors of amorphous polymers in micro-scaled deformation. *International Journal of Plasticity*.
33. Rao, Y.-N.; Dai, H.-L., Micromechanics-based thermo-viscoelastic properties prediction of fiber reinforced polymers with graded interphases and slightly weakened interfaces. *Composite Structures* **2017**, *168*, 440-455.
34. Fisher, F. T.; Brinson, L. C., Viscoelastic interphases in polymer–matrix composites: theoretical models and finite-element analysis. *Composites Science and Technology* **2001**, *61* (5), 731-748.
35. Hanzon, D. W.; He, X.; Yang, H.; Shi, Q.; Yu, K., Creep-induced anisotropy in covalent adaptable network polymers. *Soft Matter* **2017**, *13* (39), 7061-7073.
36. Kindt, P.; Briels, W. J., A single particle model to simulate the dynamics of entangled polymer melts. *The Journal of chemical physics* **2007**, *127* (13), 134901.
37. Li, Y.; Liu, Z.; Jia, Z.; Liu, W. K.; Aldousari, S. M.; Hedia, H. S.; Asiri, S. A.,

Modular-based multiscale modeling on viscoelasticity of polymer nanocomposites.

Computational Mechanics **2017**, *59* (2), 187-201.

38. Maurel, G.; Schnell, B.; Goujon, F.; Couty, M.; Malfreyt, P., Multiscale Modeling Approach toward the Prediction of Viscoelastic Properties of Polymers.

Journal of Chemical Theory and Computation **2012**, *8* (11), 4570-4579.

39. Ramírez-Hernández, A.; Detcheverry, F. A.; Peters, B. L.; Chappa, V. C.; Schweizer, K. S.; Müller, M.; de Pablo, J. J., Dynamical Simulations of Coarse Grain Polymeric Systems: Rouse and Entangled Dynamics. *Macromolecules* **2013**, *46* (15), 6287-6299.

40. Hu, A.; Li, X.; Ajdari, A.; Jiang, B.; Burkhardt, C.; Chen, W.; Brinson, L. C., Computational analysis of particle reinforced viscoelastic polymer nanocomposites – statistical study of representative volume element. *Journal of the Mechanics and Physics of Solids*.

41. Li, Z.; Liu, J.; Zhang, Z.; Gao, Y.; Liu, L.; Zhang, L.; Yuan, B., Molecular dynamics simulation of the viscoelasticity of polymer nanocomposites under oscillatory shear: effect of interfacial chemical coupling. *RSC Advances* **2018**, *8* (15), 8141-8151.

42. Agrawal, V.; Holzworth, K.; Nantasetphong, W.; Amirkhizi, A. V.; Oswald, J.; Nemat-Nasser, S., Prediction of viscoelastic properties with coarse-grained molecular dynamics and experimental validation for a benchmark polyurea system. *Journal of Polymer Science Part B: Polymer Physics* **2016**, *54* (8), 797-810.

43. Bhattacharya, M.; Bhowmick, A. K., Correlation of Vulcanization and

Viscoelastic Properties of Nanocomposites Based on Natural Rubber and Different Nanofillers, with Molecular and Supramolecular Structure. *Rubber Chemistry and Technology* **2010**, 83 (1), 16-34.

44. Jones, B. H.; Wheeler, D. R.; Black, H. T.; Stavig, M. E.; Sawyer, P. S.; Giron, N. H.; Celina, M. C.; Lambert, T. N.; Alam, T. M., Stress Relaxation in Epoxy Thermosets via a Ferrocene-Based Amine Curing Agent. *Macromolecules* **2017**, 50 (13), 5014-5024.
45. Wang, Z.; Likhtman, A. E.; Larson, R. G., Segmental Dynamics in Entangled Linear Polymer Melts. *Macromolecules* **2012**, 45 (8), 3557-3570.
46. Chen, Y.-L.; Schweizer, K. S., Microscopic theory of gelation and elasticity in polymer-particle suspensions. *The Journal of chemical physics* **2004**, 120 (15), 7212-7222.
47. Raos, G.; Moreno, M.; Elli, S., Computational Experiments on Filled Rubber Viscoelasticity: What Is the Role of Particle-Particle Interactions? *Macromolecules* **2006**, 39 (19), 6744-6751.
48. Mousavi, A. A.; Arash, B.; Zhuang, X.; Rabczuk, T., A coarse-grained model for the elastic properties of cross linked short carbon nanotube/polymer composites. *Composites Part B: Engineering*.
49. Arash, B.; Park, H. S.; Rabczuk, T., Tensile fracture behavior of short carbon nanotube reinforced polymer composites: A coarse-grained model. *Composite Structures* **2015**, 134, 981-988.
50. Arash, B.; Park, H. S.; Rabczuk, T., Mechanical properties of carbon nanotube

reinforced polymer nanocomposites: A coarse-grained model. *Composites Part B: Engineering* **2015**, *80*, 92-100.

51. Arash, B.; Park, H. S.; Rabczuk, T., Coarse-grained model of the J-integral of carbon nanotube reinforced polymer composites. *Carbon* **2016**, *96*, 1084-1092.

52. Mousavi, A. A.; Arash, B.; Zhuang, X.; Rabczuk, T., A coarse-grained model for the elastic properties of cross linked short carbon nanotube/polymer composites. *Composites Part B: Engineering* **2016**, *95*, 404-411.

53. Msekh, M. A.; Silani, M.; Jamshidian, M.; Areias, P.; Zhuang, X.; Zi, G.; He, P.; Rabczuk, T., Predictions of J integral and tensile strength of clay/epoxy nanocomposites material using phase field model. *Composites Part B: Engineering* **2016**, *93*, 97-114.

54. Tsige, M.; Stevens, M. J., Effect of Cross-Linker Functionality on the Adhesion of Highly Cross-Linked Polymer Networks: A Molecular Dynamics Study of Epoxies. *Macromolecules* **2004**, *37* (2), 630-637.

55. Faller, R., Automatic coarse graining of polymers. *Polymer* **2004**, *45* (11), 3869-3876.

56. Ying, L.; Tang, S.; Kröger, M.; Wing Kam, L., Molecular simulation guided constitutive modeling on finite strain viscoelasticity of elastomers. *Journal of the Mechanics and Physics of Solids* **2016**, *88*, 204-226.

57. Ma, C.; Ji, T.; Robertson, C. G.; Rajeshbabu, R.; Zhu, J.; Dong, Y., Molecular insight into the Mullins effect: irreversible disentanglement of polymer chains revealed by molecular dynamics simulations. *Physical Chemistry Chemical Physics* **2017**, *19* (29),

19468-19477.

58. Ikeshima, D.; Yonezu, A.; Liu, L., Molecular origins of elastoplastic behavior of polycarbonate under tension: A coarse-grained molecular dynamics approach. *Computational Materials Science* **2018**, *145*, 306-319.
59. Hagita, K.; Morita, H.; Takano, H., Molecular dynamics simulation study of a fracture of filler-filled polymer nanocomposites. *Polymer* **2016**, *99*, 368-375.
60. Hagita, K.; Morita, H.; Doi, M.; Takano, H., Coarse-Grained Molecular Dynamics Simulation of Filled Polymer Nanocomposites under Uniaxial Elongation. *Macromolecules* **2016**, *49* (5), 1972-1983.
61. Fritz, D.; Koschke, K.; Harmandaris, V. A.; van der Vegt, N. F. A.; Kremer, K., Multiscale modeling of soft matter: scaling of dynamics. *Physical Chemistry Chemical Physics* **2011**, *13* (22), 10412-10420.
62. Scherer, C.; Andrienko, D., Comparison of systematic coarse-graining strategies for soluble conjugated polymers*. *Eur. Phys. J. Special Topics* **2016**, *225* (8-9), 1441-1461.
63. Li, Y.; Abberton, B.; Kröger, M.; Liu, W., Challenges in Multiscale Modeling of Polymer Dynamics. *Polymers* **2013**, *5* (2), 751.
64. Tschöp, W.; Kremer, K.; Batoulis, J.; Bürger, T.; Hahn, O., Simulation of polymer melts. I. Coarse-graining procedure for polycarbonates. *Acta Polymerica* **1998**, *49* (2-3), 61-74.
65. Milano, G.; Goudeau, S.; Müller-Plathe, F., Multicentered Gaussian-based

- potentials for coarse-grained polymer simulations: Linking atomistic and mesoscopic scales. *Journal of Polymer Science Part B: Polymer Physics* **2005**, *43* (8), 871-885.
66. Milano, G.; Müller-Plathe, F., Mapping Atomistic Simulations to Mesoscopic Models: A Systematic Coarse-Graining Procedure for Vinyl Polymer Chains. *The Journal of Physical Chemistry B* **2005**, *109* (39), 18609-18619.
67. Accelrys Inc., San Diego, www.Accelrys.com
68. <http://lammps.sandia.gov>
69. Greco, R., Molecular weight dependence of stress relaxation of commercial polyisobutylene. *European Polymer Journal* **1978**, *14* (3), 233-237.
70. Salerno, K. M.; Agrawal, A.; Peters, B. L.; Perahia, D.; Grest, G. S., Dynamics in entangled polyethylene melts. *The European Physical Journal Special Topics* **2016**, *225* (8), 1707-1722.
71. Wolfgang, P.; Grant, D. S., Structure and dynamics of amorphous polymers: computer simulations compared to experiment and theory. *Reports on Progress in Physics* **2004**, *67* (7), 1117.
72. Li, C.; Strachan, A., Molecular scale simulations on thermoset polymers: A review. *Journal of Polymer Science Part B: Polymer Physics* **2015**, *53* (2), 103-122.
73. Putz, K. W.; Palmeri, M. J.; Cohn, R. B.; Andrews, R.; Brinson, L. C., Effect of Cross-Link Density on Interphase Creation in Polymer Nanocomposites. *Macromolecules* **2008**, *41* (18), 6752-6756.
74. Zeng, Q. H.; Yu, A. B.; Lu, G. Q., Multiscale modeling and simulation of

polymer nanocomposites. *Progress in Polymer Science* **2008**, *33* (2), 191-269.

75. Jancar, J.; Douglas, J. F.; Starr, F. W.; Kumar, S. K.; Cassagnau, P.; Lesser, A. J.; Sternstein, S. S.; Buehler, M. J., Current issues in research on structure–property relationships in polymer nanocomposites. *Polymer* **2010**, *51* (15), 3321-3343.
76. Ghanbari, A.; Rahimi, M.; Dehghany, J., Influence of Surface Grafted Polymers on the Polymer Dynamics in a Silica–Polystyrene Nanocomposite: A Coarse-Grained Molecular Dynamics Investigation. *The Journal of Physical Chemistry C* **2013**, *117* (47), 25069-25076.
77. Gojny, F. H.; Schulte, K., Functionalisation effect on the thermo-mechanical behaviour of multi-wall carbon nanotube/epoxy-composites. *Composites Science and Technology* **2004**, *64* (15), 2303-2308.
78. Li, M.; Gu, Y.-Z.; Liu, H.; Li, Y.-X.; Wang, S.-K.; Wu, Q.; Zhang, Z.-G., Investigation the interphase formation process of carbon fiber/epoxy composites using a multiscale simulation method. *Composites Science and Technology* **2013**, *86* (0), 117-121.
79. Fidelus, J. D.; Wiesel, E.; Gojny, F. H.; Schulte, K.; Wagner, H. D., Thermo-mechanical properties of randomly oriented carbon/epoxy nanocomposites. *Composites Part A: Applied Science and Manufacturing* **2005**, *36* (11), 1555-1561.
80. Shiu, S.-C.; Tsai, J.-L., Characterizing thermal and mechanical properties of graphene/epoxy nanocomposites. *Composites Part B: Engineering* **2014**, *56*, 691-697.
81. Odegard, G. M.; Clancy, T. C.; Gates, T. S., Modeling of the mechanical properties of nanoparticle/polymer composites. *Polymer* **2005**, *46* (2), 553-562.

82. Ramanathan, T.; Liu, H.; Brinson, L. C., Functionalized SWNT/polymer nanocomposites for dramatic property improvement. *Journal of Polymer Science Part B: Polymer Physics* **2005**, *43* (17), 2269-2279.
83. Yang, S.; Cho, M., A scale-bridging method for nanoparticulate polymer nanocomposites and their nondilute concentration effect. *Applied Physics Letters* **2009**, *94* (22), 223104.
84. Yu, S.; Yang, S.; Cho, M., Multi-scale modeling of cross-linked epoxy nanocomposites. *Polymer* **2009**, *50* (3), 945-952.
85. Amnaya, P. A.; Dimitris, C. L.; Daniel, C. H., Modeling of graphene–polymer interfacial mechanical behavior using molecular dynamics. *Modelling and Simulation in Materials Science and Engineering* **2009**, *17* (1), 015002.
86. Safaei, M.; Sheidaei, A.; Baniassadi, M.; Ahzi, S.; Mosavi Mashhadi, M.; Pourboghrat, F., An interfacial debonding-induced damage model for graphite nanoplatelet polymer composites. *Computational Materials Science* **2015**, *96*, Part A, 191-199.
87. Sun, Y.; Zhang, Z.; Moon, K.-S.; Wong, C. P., Glass transition and relaxation behavior of epoxy nanocomposites. *Journal of Polymer Science Part B: Polymer Physics* **2004**, *42* (21), 3849-3858.
88. Kim, B.; Choi, J.; Yang, S.; Yu, S.; Cho, M., Influence of crosslink density on the interfacial characteristics of epoxy nanocomposites. *Polymer* **2015**, *60*, 186-197.
89. Eshelby, J. D., The determination of the elastic field of an ellipsoidal inclusion,

and related problems. *Proceedings of the Royal Society of London. Series A. Mathematical and Physical Sciences* **1957**, 241 (1226), 376-396.

90. Kim, B.; Choi, J.; Yang, S.; Yu, S.; Cho, M., Multiscale modeling of interphase in crosslinked epoxy nanocomposites. *Composites Part B: Engineering* **2017**, 120 (Supplement C), 128-142.

91. Wagner, H. D.; Vaia, R. A., Nanocomposites: issues at the interface. *Materials Today* **2004**, 7 (11), 38-42.

92. Gong, L.; Kinloch, I. A.; Young, R. J.; Riaz, I.; Jalil, R.; Novoselov, K. S., Interfacial Stress Transfer in a Graphene Monolayer Nanocomposite. *Advanced Materials* **2010**, 22 (24), 2694-2697.

93. Nie, M.; Kalyon, D. M.; Fisher, F. T., Interfacial Load Transfer in Polymer/Carbon Nanotube Nanocomposites with a Nanohybrid Shish Kebab Modification. *ACS Applied Materials & Interfaces* **2014**, 6 (17), 14886-14893.

94. Li, Y.; Seidel, G. D., Multiscale modeling of the effects of nanoscale load transfer on the effective elastic properties of unfunctionalized carbon nanotube-polyethylene nanocomposites. *Modelling and Simulation in Materials Science and Engineering* **2014**, 22 (2), 025023.

95. Song, S.; Chen, Y.; Su, Z.; Quan, C.; Tan, V. B. C., Effects of clay structural parameters and gallery strength on the damage behavior of epoxy/clay nanocomposites. *Composites Science and Technology* **2013**, 85, 50-57.

96. Guo, Q.; Zhu, P.; Li, G.; Wen, J.; Wang, T.; Lu, D.; Sun, R.; Wong, C., Study on

the effects of interfacial interaction on the rheological and thermal performance of silica nanoparticles reinforced epoxy nanocomposites. *Composites Part B: Engineering*.

국문 요약

본 논문에서는 고무의 점탄성 거동 및 이력 마찰 특성을 규명하기 위한 멀티스케일 해석 방법론을 제시한다. 기존의 분자동역학 전산모사는 고분자 재료의 물성을 예측하는데 큰 기여를 해왔지만, 시간과 공간 스케일의 한계로 이하여 메조스케일에 대한 특성을 다루는데 한계를 보여왔다. 본 연구에서는 여러 원자로 구성된 단위 구조를 가상의 입자로 치환하여 전체 시스템의 자유도를 줄임으로써 기존 분자동역학 전산모사의 시간/공간 스케일의 한계를 극복하는 축소 분자동역학 기법을 도입하였다. 이를 통해 확장된 시간/공간 스케일에서 고무의 시간에 따른 안정화 특성을 정량적으로 다를 수 있으며 고무 재료의 점탄성 거동의 규명을 가능케 하였다. 이를 바탕으로 고무의 분자량과 가황 특성 및 실리카 강화입자 삽입에 따른 점탄성 거동의 변화를 도출하였다. 특히, 분자량 증가와 가황 과정은 고무의 시간에 따른 안정화 특성을 크게 변화시킴을 확인하였다. 반면, 실리카 입자에 대한 점탄성 거동의 변화는 크지 않다. 이는 실리카 입자와 고무의 약한 상호작용력에 기인한다. 축소 분자동역학 전산모사를 통해 도출된 시간에 따른 안정화 특성은 퓨리에 변환을 통해 주파수 영역에 대한 종탄성계수 및 손실계수를 제공한다.

탄성체의 마찰 특성은 마찰 표면 특성, 재료의 동적 물성, 속도, 온도 등에 영향을 받는다. 탄성체의 경우 이력 마찰 특성이 전체 마찰 특성을 좌우하게 되는데, 이는 마찰 과정에서 표면에서 발생하는 변형에 의한 에너지 소산과 관련이 있다. 본 연구에서는 축소 전산모사를 통해 도출된 동적 물성에

기반하여, 주어진 마찰 조건에서 이력 마찰 계수를 도출하였다. 이를 통해 탄성체의 마찰 특성을 종합적으로 규명할 수 있는 멀티스케일 해석 방법론을 정립하였다.

본 연구는 탄성체의 점탄성 특성 및 마찰 특성을 종합적으로 규명할 수 있는 해석 기반 멀티스케일 방법론을 제안함으로써 다양한 산업 분야에 적용될 수 있는 가능성을 제시한다. 표면과 맞닿아 작동하는 다양한 고분자 소재의 마찰 특성을 해석적 접근을 통해 순차적으로 규명할 수 있으므로 폭넓은 활용이 기대된다.

주요어: 탄성체, 점탄성 거동, 이력 마찰, 멀티스케일 해석, 축소 분자동역학

학번: 2012-23937